Modelling of a large scale High-Temperature Thermal Energy Storage System

Aalborg University
Department of Energy Technology
4th semester Master Thesis
M.Sc. In Thermal Energy and Process Engineering
Group TEPE4-1008

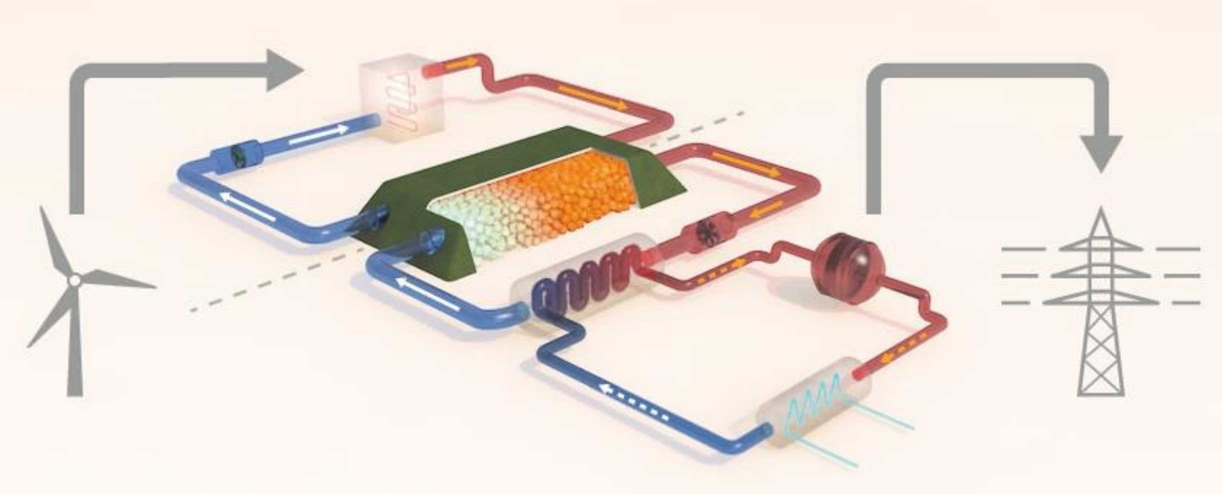

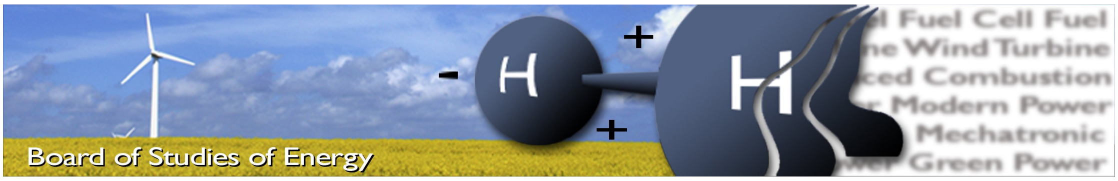

Title: Modelling of a large scale High-Temperature Thermal Energy Storage System
Semester: 4^{th} M.Sc.
Semester theme: Master's thesis
Project period: 01.02.17 to 1.06.17
ECTS: 30
Supervisors: Kim Sørensen and Thomas J. Condra
Project group: TEPE4-1008

ABSTRACT:

The share of the Danish energy demand covered by renewables has increased steadily since the 1990's. Because of this, energy storage is becoming a more viable solution for peak shaving and a key component for transitioning to renewable power generation.

Thermal Energy Storage (TES) utilises a packed bed of rocks to store high temperature thermal energy originating from fluctuating sources such as wind power. When needed, heat is extracted and converted to electricity using a steam Rankine cycle.

A TES resembling a cone section is dynamically modelled to investigate the heat transfer- and pressure loss characteristics. A parametric study is conducted to identify the governing parameters of the TES performance. Two steam Rankine cycles are modelled as a part of the auxiliary system to identify efficiencies and heat exchanger areas.

It is concluded that a TES with a volume of 175,000 m^3 effectively utilises only 40.5% of the storage volume. A rock diameter of 3 cm is selected as the optimum size. Energy and exergy efficiencies for thermal cycling of the TES are, for most cases, above 98%.

A single pressure steam Rankine cycle is able to produce 35.34 MW_{el} at a discharge rate and temperature of 221.2 kg/s and 873 K respectively, with an energy efficiency of 32.2%.

Kristian Kristensen

Søren Søndergaard Batz

Copies: 3
Pages: 111
Appendices: 8

By signing this document, each member of the group confirms that all participated in the project work, and thereby all members are collectively liable for the content of the report. Furthermore, all group members confirm that the report does not include plagiarism.

Executive summary

The purpose of this study is to dynamically model a High Temperature Thermal Energy Storage (HT-TES) in order to investigate the dynamic behaviour of the thermal energy storage. A parametric study is conducted to identify the governing parameters of the TES performance and investigate the effects of these on the performance characteristics of the TES.

As power production gradually transitions from centralised power production from thermal power plants to decentralised production from fluctuating renewable energy sources, the viability of energy storage systems has increased. In 2015, the Danish wind power production covered 42% of the total domestic electricity demand. A potential benefit of energy storage includes the possibility to become more energy independent by storing surplus wind power production instead of exporting to neighbouring countries. For future energy systems, consisting purely renewable and often fluctuating energy sources, energy storages are considered key components for peak shaving.

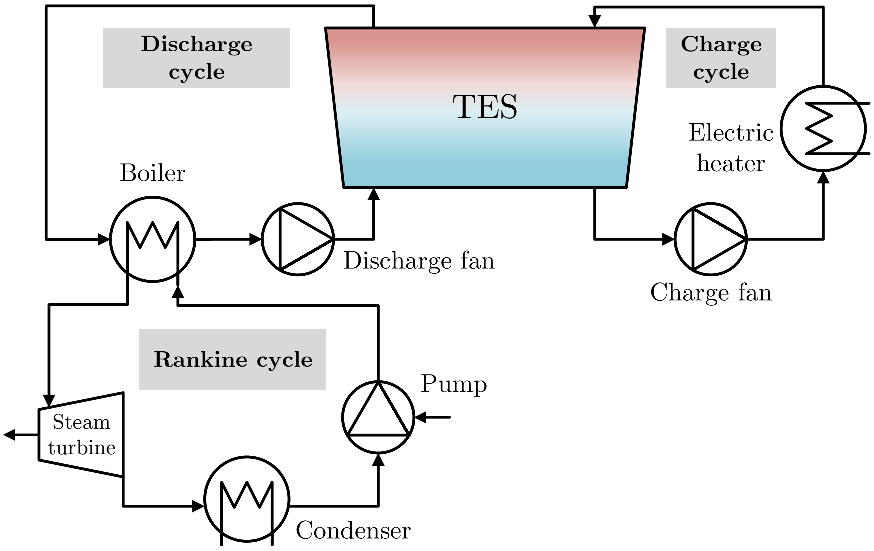

Figure 1: Schematic of the TES system.

One type of energy storage is the Thermal Energy Storage (TES), which stores electricity in the form of thermal energy. The type of TES studied in this investigation consists of a packed bed of solid storage media *i.e.* rocks. The TES is charged using a dedicated charge cycle as seen in figure 1 using air as a secondary heat transfer medium. The air, heated by an electric heater, is led through the TES by a fan during charging of the storage. Here, the thermal energy in the charge air is transferred to the rocks in the TES. When the storage is discharged, cold air is pumped through the TES utilising a dedicated discharge cycle where the air is heated by the rocks. The hot discharge air is then led through a boiler connected to a traditional steam Rankine cycle to generate electrical power.

A conical packed bed TES with a volume of 175.000 m^3, a height of 25 m and a roof and bottom radius of 49.19 m and 45.19 m respectively was used for the majority of this investigation.

A dynamic model of the TES was created based on the Schumann model for packed beds. The model covers the internal heat transfer between the secondary heat transfer medium and the solid heat storage material by convection as well as axial radiation and conduction. The pressure loss through the TES, a key factor in determining the overall system efficiency, has been modelled using a modified version of the Ergun equation. Two versions of the traditional steam Rankine cycle have modelled and optimised for selected paremters to determine amount of power produced by the TES system, another key parameter in determining the overall system performance.

Based on the results from the developed models and conducted parametric studies, the following conclusions can be drawn:

- A rock size of 3 cm in diameter was found to be the optimal compromise between a sufficiently small Biot number and an acceptable pressure loss.
- The maximum charge/discharge rate, based on the maximum allowable Biot number, was fount to be 553 kg/s.
- From parametric studies, it can be concluded that only 40.5% of the total storage volume of 175,000 m^3 could be effectively utilised to store useful thermal energy.
- It is concluded that the initial insulation thicknesses, some places up to 0.6 m thick, could be reduced by as much as 40% without affecting the TES efficiency and performance to a noticeable degree.
- Energy and exergy efficiencies remained above 98% for all but the most extreme cases investigated in the parametric study.
- A single pressure steam Rankine cycle operating for a charge rate from the TES of 221.2 kg/s was able to produce 35.34 MW_{el} at a thermal efficiency of 32%.

Preface

This master's thesis was written by group TEPE4-1008 during the 4th of the M.Sc. in *Thermal Energy and Process Engineering* semester at the Department of Energy Technology, spring 2017, Aalborg University. This thesis covers a study of a Thermal Energy Storage system and subsequent modelling of the Thermal Energy Storage and auxiliary systems. The results include a parametric study of the system behaviour with an emphasis on the thermal energy storage performance. This thesis consists of a main report and additional supplementary appendices.

The thesis consists of the following main parts:

- Introduction to thermal energy storage systems.
- State of the art analysis of thermal energy storage systems.
- Modelling of a thermal energy storage and auxiliary discharge cycle.
- Parametric studies of the thermal energy storage and auxiliary system.
- Presentation of system results and efficiencies

Applications and tools used in this thesis include:

- *EES* - for analytic modelling.
- *MATLAB* - for analytic modelling and data processing.
- *Simulink* - for dynamic modelling and simulation.
- *REFPROP* - fluid properties library for MATLAB.

Reading Instructions

A list of nomenclature can be found in the beginning of the report including descriptions and units for each variable. References are listed in the end of the appendix report[1]. In the text, references are represented using the Harvard method shown as (Author, Year). The references in the bibliography are given in the following manner:

Author, Title, Publisher, Journal, Year, URL, ISBN

All equations, figures and tables are numbered in correspondence with appendix number and in the order of appearance.

---

[1] Front page image: https://www.siemens.com/customer-magazine/en/home/energy/renewable-energy/shaping-the-future.html

Nomenclature

Symbol	**Description**	**Unit**
a_p	Area per surface volume	[m^2/m^3]
A	Area	[m^2]
C	Correction	[$-$]
c_s	Solid-phase specific heat capacity	[J/kg-K]
d	Diameter	[m]
E	Energy	[J]
Ex	Exergy	[J]
g	Gravitational acceleration	[m/s^2]
f	Fraction	[$-$]
f_f	Fanning friction factor	[$-$]
G	Core mass flow rate (flux)	[kg/m^2-s]
H	Height	[m]
h	Enthalpy	[J/kg]
h_{vol}	Volumetric heat transfer coefficient	[W/m^2-K]
h_{rv}	Void to void heat transfer coefficient	[W/m^2-K]
h_{rs}	Surface to Surface heat transfer coefficient	[W/m^2-K]
h	Enthalpy	[J/kg]
j	Colburn heat transfer factor	[$-$]
K_g	Pressure loss coefficient	[$-$]
L	Length	[m]
$\dot{m}$	Mass flow rate	[kg/s]
N	Max grid elements	[$-$]
N_r	Number of tube rows	[$-$]
Nu	Nusselt number	[$-$]
P_l	Longitudinal pitch	[m]
P_t	Transverse pitch	[m]
p	Pressure	[Pa]
Δp	Pressure loss	[Pa]
r	Radius	[m]
Pr	Prandtl number	[$-$]
Q	Absorbed heat	[J]
$\dot{q}$	Rate of heat transfer	[W]
R	Thermal resistance	[K/W]
Re	Reynolds number	[$-$]
s	Entropy	[J/kg-K]
T	Temperature	[K]

Symbol	**Description**	**Unit**
t	Time	[s]
U	Overall heat transfer coefficient	$\left[\mathrm{W/m^2\text{-}K}\right]$
u	Internal energy	[J/kg]
v	Interstitial velocity	[m/s]
V	Volume	$\left[\mathrm{m^3}\right]$
$\dot{V}$	Volume flow	$\left[\mathrm{m^3/s}\right]$
W	Work	$[W]$
x	Packed bed length	[m]

Greek Letters

Symbol	**Description**	**Unit**
β	Distance ratio for effective conduction coefficient	$[-]$
ϵ	emissivity	$[-]$
ε	Void fraction	$[-]$
μ	Dynamic viscosity	[Pa s]
ρ	Density	$\left[\mathrm{kg/m^3}\right]$
ψ	Exergy efficiency	$[-]$
Ψ	Particle sphericity	$[-]$
ϕ	Ratio of eff. thickness of fluid film	$[-]$
λ	Conduction coefficient	[W/m-K]
γ	Ratio of effective particle lengths	$[-]$
η	Energy efficiency	$[-]$

Subscripts

Subscript	**Description**
∞	Ambient
cond	Condenser
conv	Convection
eff	Effective
ext	External
f	Fluid phase
in	Inlet
m	Mean
n	Current grid point
o	Outer
out	Outlet
p	Particle
r	Reversible
rad	Radiation
s	Solid phase
th	Thermal
tot	Total
turb	Turbine
v	Void
vol	Volumetric

Abbreviations

Abbrevation	**Description**
CSP	Concentrated Solar Power
DP	Dual Pressure
HP	High Pressure
HT	High Temperature
GCI	Grid Convergence Index
LMTD	Log Mean Temperature Difference
LDC	Low Density Concrete
LP	Low Pressure
PCM	Phase Change Material
SP	Single Pressure
SRC	Steam Rankine Cycle
TES	Thermal Energy Storage
UHPC	Ultra High Performance Concrete

Contents

1. Introduction

Initiatives by the Danish government and a 2025 energy plan to reduce greenhouse gas emissions and increase energy security has resulted in a decentralisation of power production and is making conventional fossil fuelled central power plants, coal fired plants in particular, appear obsolete.

2015 experienced a historically low electricity production from centralised thermal power plants with a drop of 29% compared to 2014, and an increase in the production of electricity from wind turbines by 8%. The increase in wind power production was primarily due to favourable wind conditions. In total, 42% of the Danish electricity demand in 2015 was covered by wind turbine production and is expected to cover 60% of the electricity production in 2025 (Friberg, 2016).

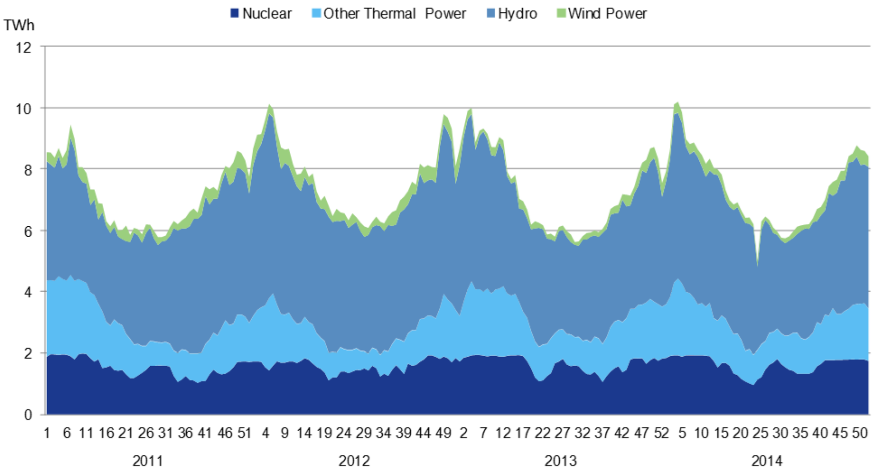

Figure 1.1: Electricity production in the Nord Pool Market from 2011 to 2014 was largely characterised by hydro-, thermal- and nuclear power (Nord Pool AS).

A general tendency, since the 1990's, is a decentralisation of power production, an increase in de-centralised renewable energy production and the retirement of fossil fuel power plants or conversion to biomass. An important aspect of this development is the integration of wind power with the thermal power plants, which currently still provide a base load of power and heat.

Denmark is a part of the free Nordic energy market *Nord Pool Spot* where the price of electricity is regulated by supply and demand. The Nord Pool Spot market has expanded since the 1990's and the market now includes the Nordic and Baltic countries, Germany and the UK.

Power plants with the highest bidding price set the overall electricity price whilst power produced from the cheapest production units is offered at prices closest to zero. This means that wind power will always push the highest priced power plants off the market and thus regulate the price accordingly (Lykkedal, 2016). The Nordic electricity production and the price of electricity are largely characterised by the increased capacity of renewable energies, hydro power production and storage capacity in Norway and Sweden and the seasonal impact on these sources. This is illustrated in figure 1.1.

When wind power is plentiful during dry years and during the winter, surplus power is available which is exported to Norway and Sweden at relatively low prices and sometimes at a negative prices to be stored as hydro power. In wet years and in the summer, the wind power production in Denmark and Germany is generally lower. In these situations, cheap hydro power is often imported from the northern countries. The price of electricity is mostly governed by the other countries of the Nordic energy market and is only governed nationally in Denmark about 10% of the time (Danmarks Vindmølleforening, 2015).

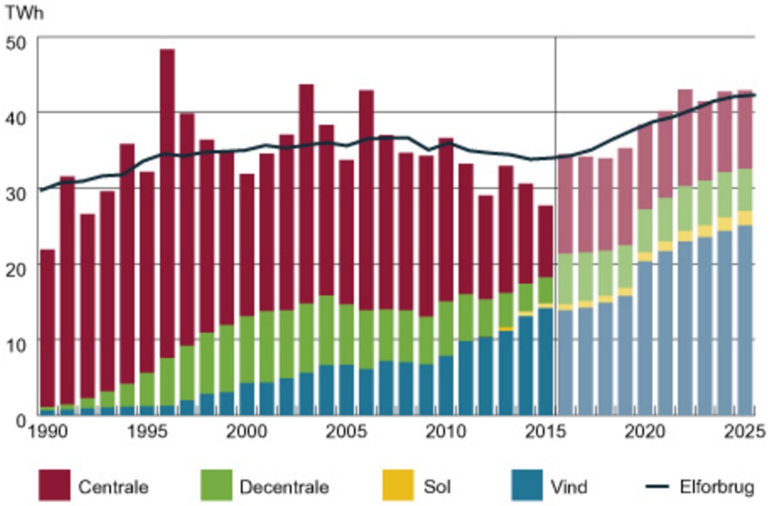

Figure 1.2: The Danish electricity production up to 2015 can be characterised by an increase in production from renewables and a decrease in production from central power plants (Friberg, 2016).

One way of addressing the issues stated above is to introduce *Thermal Energy Storage* (TES) to take advantage of surplus wind power production to make the Danish energy sector more self sufficient and flexible thus increasing energy security. They have the prospect of being relatively cheap compared to other storage technologies, can improve the energy flexibility by utilising cheap domestically produced wind power and enable the utilisation of existing brown-field power plant installations which are otherwise scheduled for retirement.

1.1 Thermal energy storage

Thermal energy storages can be divided into three main categories: Sensible Heat, Latent Heat and Thermochemical energy storages. The different technologies are illustrated in figure 1.3. Depending on factors such as the storage scale and the application, an appropriate storage can be selected.

In **Thermochemical** thermal energy storages, heat is stored by means of chemical reactions, where synthesis such as steam reforming of methane, adsorption and dissociation reactions are common mechanisms.

Latent heat storage media undergo phase change and have the advantage of comparatively high heat transfer, stable temperature levels and comparatively small storage units (Tahat et al., 1993). Types of storage media include organic substances such as alcohols, glycols and inorganic substances such as salts and metal alloys. The substances may be encapsuled in tubes, spheres or panels for more convenient containment.

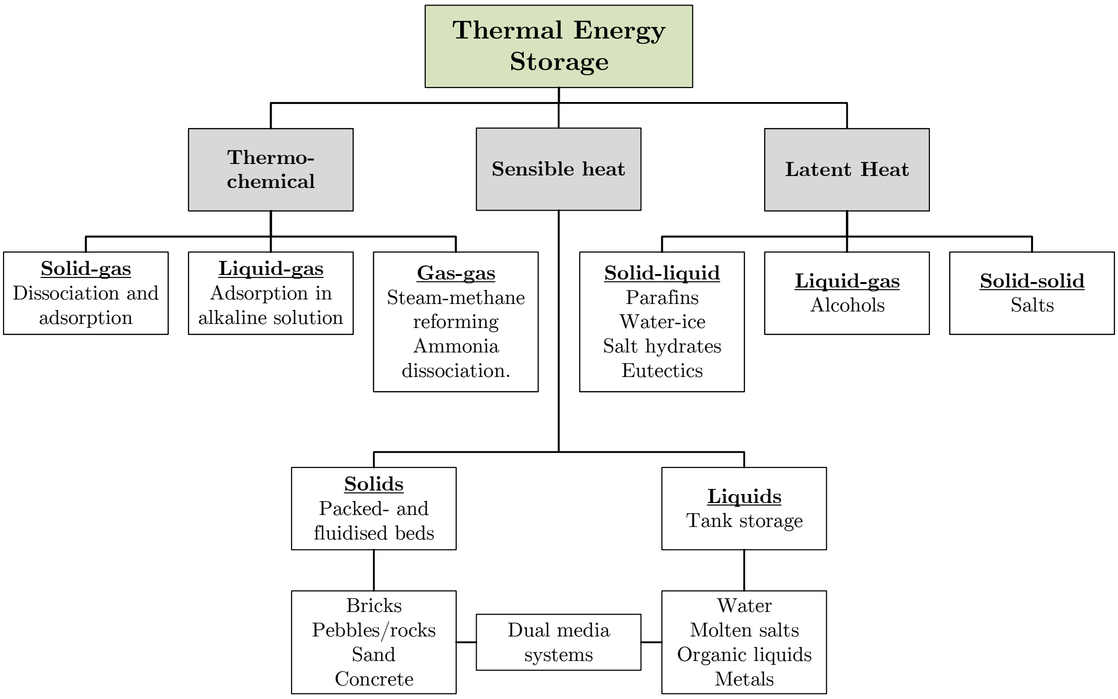

Figure 1.3: Main types of thermal storage types. Adapted from Alva et al. (2017); Tahat et al. (1993); Singh et al. (2010).

Sensible heat storages utilise storage media that do not undergo phase change when the storage is charged. The amount of heat that can be stored is governed by the specific heat capacity c_p of the storage media and charging and discharging of the storage raises or lowers the temperature of the storage media. Common types of sensible heat storage media include rocks, concrete, ceramics, liquid water and molten salts (Alva et al., 2017).

Solid storage media like rocks are arranged in packed beds and have the advantage of being relatively cheap, mechanically stable, are easy to contain and are readily available (Singh et al., 2010). These advantages, though, come at the expense of large required mass flows of the heat transfer media, low energy density compared to the other technologies, inherent self discharge due to higher temperature ranges and relatively high pressure losses through the storage (Kalaiselvam and Parameshwaran, 2014).

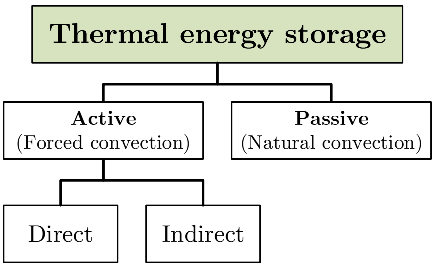

Figure 1.4: System operational modes.

Sensible heat storage is a widely researched and mature technology and is currently the most common in use due to its relative simple implementation, reliability and an abundance of cheap storage media (Kalaiselvam and Parameshwaran, 2014; Zanganeh, 2014).

There are generally two methods of charging and discharging of the thermal energy storage. The heat transfer can be either *direct*, circulating the heat storage medium itself, or *indirect* using a stationary heat storage medium and a secondary heat transfer medium for charging and discharging of the storage. This is illustrated in figure 1.4.

The heat transfer in an *active* system can be either direct or indirect depending on the storage medium. Here, the storage medium or a secondary heat transfer medium is circulated with a mechanically driven pump or fan and thus, heat transfer is governed by forced convection. In contrast, *passive* systems utilise natural convection to circulate the heat storage medium for a direct heat transfer or a secondary heat transfer medium for indirect heat transfer.

The thermal energy storage system considered in this report consists of the ***Thermal Energy Storage*** itself, ***charge and discharge cycles*** including fans and heat exchangers and a ***thermal power cycle*** for power generation as seen in figure 1.5.

The system works by charging the thermal energy storage using a separate charging cycle, either with heat generated from electricity, heat generated from the existing power plant boiler or a combination of the two, using air as heat transfer media. The storage can then be discharged, also using air, in a separate discharging cycle. Here, the air is led through a boiler to generate steam for the power cycle. The cooled air is returned to the storage and the cycle is repeated.

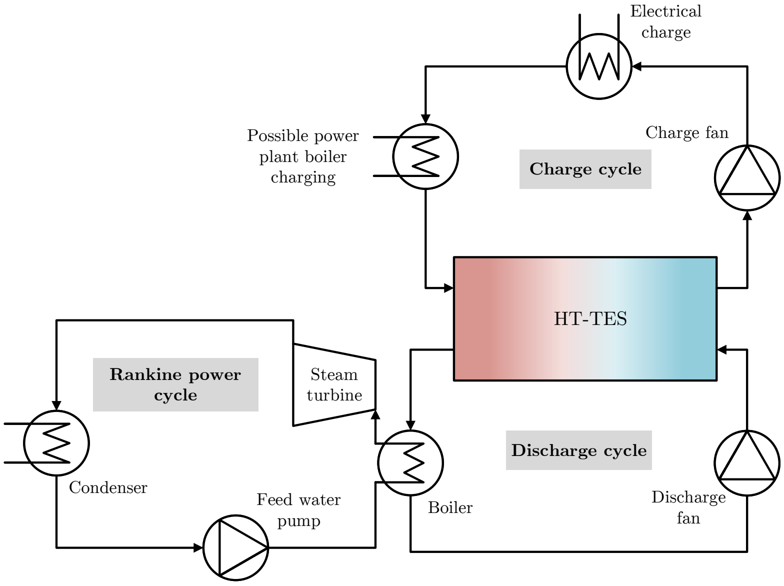

Figure 1.5: A proposed TES system consisting of a thermal storage, a charge- and discharge system and a power cycle.

1.2 State of the art

The majority of research on high-temperature thermal energy storages concern applications for solar power plants and solar power generation utilising solar energy to drive a thermodynamic power cycle. Thus, studies for dedicated thermal energy storages or retrofits for existing power plants are not numerous. The most common type of heat storage currently applied is sensible heat storages with mediums such as hot water and rocks or pebbles for hot or cold storage. Low temperature sensible heat storages often find their use in building applications for air heating or cooling, whereas medium to high temperature thermal energy storages are currently used mostly for concentrated solar power applications. The majority of studies focus on small, pilot-scale storages.

Packed bed thermal energy storage

An extensive study carried out by (Zanganeh, 2014) covered a numerical two-phase study of a high temperature 6.5 MWh pilot scale thermal energy storage. The storage was shaped as a cone segment utilising rocks as sensible heat storage medium with air as the charging medium. This was experimentally validated utilising a 42.2 $\mathrm{kWh_{th}}$ lab scale test storage. The physical properties of the numerical model was investigated in the temperature range of 50-650°C. Results from a scaled model to a 100 $\mathrm{MWh_{th}}$ storage for a 3 $\mathrm{MW_{th}}$ Concentrated Solar Power plant showed that, for a charging temperature of 640°C, the discharge temperature remained above 550°C and the overall efficiency reached 89%. The author defines this as the a first law efficiency accounting for loss to surroundings and pump work. A similar scale up to a 7.2 $\mathrm{GWh_{th}}$ storage for a 26 $\mathrm{MW_{el}}$ CSP plant yielded 92% overall efficiency with discharge temperatures above 590°C for a charging temperature of 650°C. The overall efficiency was defined as the charging efficiency multiplied by the discharging efficiency. Further parametric studies of the storage dimensions, insulation thickness and storage medium particle sizes were carried out, utilising relations for the storage heat transfer from authors such as Schumann (1929), pressure loss through the storage from authors such as Ergun and Orning (1949) and correlations for storage medium convective heat transfer compared for several authors including Coutier and Farber (1982). Additionally, the stabilising effect of the addition of encapsulted phase change materials to the sensible heat storage was investigated. It was found that the storage discharge temperature could be held constant at the PCM melting temperature with 4.4% of the stored energy originating from the PCM.

A similar model and experimental study by Geissbühler et al. (2016) investigated a combined packed bed and latent heat storage utilising capsuled aluminium alloy to stabilise the drop in the discharge temperature for a conventional sensible heat storage. They constructed a one-dimensional transient heat transfer model which was validated using exact solutions and experimental data for a 42 $\mathrm{kWh_{th}}$ pilot scale combined storage. The authors conclude that exergy efficiencies can be increased and that the material costs can be reduced when compared to a sensible heat storage for a given discharge temperature. The PCM postpones the drop in temperature compared to a pure sensible heat storage and thus, cost is reduced as less sensible heat material is required. The total cost of the storage was dominated by structural concrete and insulation. They found that exergy losses were dominated by thermal losses to the surrounding as well as pumping losses. The simulations showed exergy efficiencies above 95% as well as costs below 15 dollar per $\mathrm{kWh_{th}}$.

(Allen, 2010) conducted an extensive study on the application of packed bed thermal energy storage for solar power applications using air as the charge medium and slag or rock as the heat storage medium. The author conducted experimental testing on a packed bed for different rock types thermally cycled between 30°C to 510°C to validate existing equations for pressure loss and heat transfer mechanisms in the storage during cycling. Additionally, the influence of the average size of the rocks, density and specific heat capacity was also investigated. Based on the experimental investigation, it is concluded that the pressure loss estimation based on Ergun and Orning (1949) under-predicts the pressure loss for particle Reynolds numbers less than 3500 by as much as 40%. The pressure loss was found to proportional the air flow velocity to the power of 1.8 for particle Reynolds numbers above 500. The effectiveness NTU method combined with correlations for heat transfer was able to predict the temperature profiles within 15% of the measured temperatures from conducted experiments.

Hänchen et al. (2011) considers a HT-TES packed rock bed for a CSP application using air as the charge medium. They constructed a one-dimensional two phase model with energy equations formulated for combined convection and conduction heat transfer. The model was used to simulate both charge and discharge cycles. The results obtained from this model were validated by data obtained from a pilot-scale experimental setup comprised of a packed bed of crushed magnesium silicate rock at temperatures of 800 K. They performed a parametric study of the fluid flow rate, the type of storage material, the particle diameters and the bed dimensions to investigate the characteristics of the charge- and discharge cycles, the overall thermal system efficiency and the cycle capacity ratio defined as the ratio of the amount of energy currently stored to the theoretical maximum governed by the temperature of the charge air. They found that, for continuous and under optimal conditions, the overall efficiency exceeded 90%. The pumping work constituted for less than 1% of the stored energy except when operating with very small storage media particles. The volumetric heat capacity was found to be the most relevant property of the storage material while thermal conductivity only had a minor effect. Lastly, the authors conclude that the highest efficiency was achieved with the smallest particle size investigated of 2 mm with an increased pumping work of almost 2% of the stored energy.

(Mertens et al., 2014) investigated a packed rock bed consisting of quartzite using air as the secondary heat transfer medium for charging and discharging by creating a mathematical model. The model was then scaled to a semi-industrial 1.5 $\mathrm{MW_{el}}$ solar power plant and optimised to achieve the highest electrical efficiency during charging and discharging. The storage capacity corresponded to four hours of full load operation. They conducted a grid dependency study of the numerical solution of the discretised heat storage and found that, on this scale, a change in grid size from 200 control volumes to 400 volumes yielded a change in the calculated results of less than one percent. It was concluded that, when selecting the storage geometry, the compressor work should be considered to minimise the drop in the overall efficiency as a result of increased pumping work. Lowering the charge and discharge air velocity in the storage reduces the pressure loss. Integrating the TES into the investigated CSP pilot plant, an efficiency reduction of 1.4% points could be attributed to the compressor. Some general requirements for optimum heat storage implementation include (Medrano et al., 2010; Hauer, 2013; Stiesdal, 2016a):

- **Efficiency** of the system accounting for losses such as pumping work to overcome the internal pressure losses, losses in auxiliary components and loss to surroundings from the thermal energy storage.
- **Capacity** must be appropriate for the expected loads to utilise as mush of the storage as possible while saving on material costs.
- **Storage period** must be considered in relation to the expected cycling period as well as thermal losses from the storage and inherent self discharge as a function of time.
- **Power** relating to charging and discharging which governs how fast the storage can be either charged or discharged.
- **Cost** accounting for capital, operating and maintenance costs.
- **Life time** including stability of the storage materials and resistance to thermal degradation due to thermal cycling.

Properties of storage materials

Several studies investigating the thermo-physical properties of common natural rock types exist. Natural rocks are divided into three main categories (Geology.com, 2017):

Igneous or magmatic rock originating from cooled magma.

Sedimentary or secondary rock originating from sediments of igneous rock, minerals or organic materials.

Metamorphic rock formed from other rock types subjected to high pressure and temperature leading to a change in structure.

Potential candidates for sensible, high temperature packed bed thermal energy storage are listed in table 1.1.

Type	C_p [J/kg K]	ρ [kg/m^3]	λ [W/m K]
Gabbro$^{1)}$	$643 \pm 24(20°C)$	2911 ± 2.69	$2.05 \pm 0.04(173°C)$
Granite$^{2)}$	892(20°C)	2750	2.9
Basalt$^{4,6)}$	920(500°C)	3000	–
Quartzite$^{1)}$	$623 \pm 12(20°C)$	2618 ± 1.68	$3.37 \pm 0.11(173°C)$
Limestone$^{1)}$	$683 \pm 15(20°C)$	2697 ± 1.66	$2.05 \pm 0.03(173°C)$
EAF slag$^{3)}$	933(500°C)	3430	1.34
HT Concrete$^{5)}$	916(350°C)	2750	1.0(350°C)
Castable ceramics$^{5)}$	866(350°C)	3500	1.35(350°C)

Table 1.1: High temperature thermal energy storages from recent studies. $^{1)}$(Zanganeh et al., 2012), $^{2)}$ (Hahne, 1999-2014), $^{3)}$(nigo Ortega-Fernández et al., 2015), $^{4)}$ (Martin et al., 2014), $^{5)}$ (Laing et al., 2006)

Tiskatine et al. (2016) conducted a study on the suitability of different rock types for high temperature thermal energy storages utilising air as the charge medium. The authors studied the characteristics of rock types such as igneous or magmatic rock and sedimentary rock such as sandstone. The rocks are cycled between 20°C and 650°C. The chemical and thermophysical parameters influencing the rock life time are investigated as well as the effect of thermo-mechanical stress during cycling. They conclude that, among the investigated rock types, quartzitic sandstone, calcite, quartzite and rhyolite in particular were most suitable for use in a thermal energy storage. On the contrary, marble, granite and limestone degraded as a function of thermal cycling.

Based on 125 thermal cycles, Allen (2010) concludes that igneous rock types such as granite and dolerite are most suitable suitable rock types for high-temperature thermal storages. Metamorphic rock types such as quartzite was found to fail after only 40 cycles between 510°C and room temperature while sedimentary rock types such as sandstone and shale failed at temperatures of 70 and 200°C respectively.

Zanganeh (2014) conducted experiments for temperatures up to 600°C to investigate thermophysical properties such as the thermal conductivity as a function of temperature, density and the heat capacity, of different rock types. Additionally, a study on the mean diameter, particle size distribution and spherity of rocks was conducted.

General requirements and considerations for selection of heat storage medium in the thermal energy storage include (Alva et al., 2017):

Figure 1.6: A common igneous rock type, basalt (Geology.com, 2017).

Figure 1.7: A very common igneous rock type in Scandinavia, granite (Geology.com, 2017).

- Specific heat capacity
- Density and volume change as a function of temperature
- Thermal conductivity
- Availability and cost of storage material
- Thermal, chemical and mechanical stability
- Corrosivity, toxicity and flammability.
- Melting point

1.3 Large scale, high-temperature packed bed storages

Heat storage capacities for thermal energy storages are calculated based on assumptions for constant c_p values and a set temperature gradient. They are often specified in terms of thermal energy or the potential electrical energy including the efficiency of a power cycle. A general consensus does not currently exist, since the specific capacity of each storage depends on the operating temperature range, exergy considerations and depth of discharge and must thus be specifies for the individual storage application. Zanganeh (2014) defined the storage heat capacity for a gradient from ambient conditions of 20°C to the charge temperature while other authors define the capacity from the gradient between the charge and discharge temperature of the relevant cycle.

Location	Geometry	r_{lid} [m]	r_{bottom} [m]	H [m]	Rated capacity [MWh_{th}]
Ait Baha, Morocco	Cone section	6	5	4	100
Biasca, Switzerland	Cone section	2	1.25	4	6.5
Scale up (concept)	Cone section	20	16	25	7.2

Table 1.2: High temperature thermal energy storages from recent studies.

(Zanganeh, 2014) presented storage geometries of pilot plants built in Ait Baha, Morocco, and a test facility built by Airlight Energy SA in Biasca, Switzerland. These geometries resemble a cone shaped, underground packed bed as seen in figures 1.8 and 1.9.

Examples of physical high-temperature thermal energy storages currently in use as well as a scaled concept can be seen in table 1.2.

These geometries are charged from the top and discharged from the bottom to maintain a high temperature heat front. When comparing the storage to the requirements stated in section 1.2, the advantage of this type of storage is lower pressure loss and mechanical stability of the construction and packed bed material due to the cone shaped walls allowing for thermal expansion of the storage material. The disadvantage of this type is limitation in the scalability due to structural limitations. This can, though, potentially be overcome by arranging several storage units in parallel or series, depending on the desired storage characteristics for the relevant application. Additionally, the inherent shape of the storage changes the flow velocity of the charge media.

Figure 1.8: The 6.5 MWh pilot plant at Biasca Research Facility, Switzerland (Zanganeh, 2014).

Figure 1.9: The 100 MWh CSP pilot plant in Ait Baha, Morocco (Zanganeh, 2014).

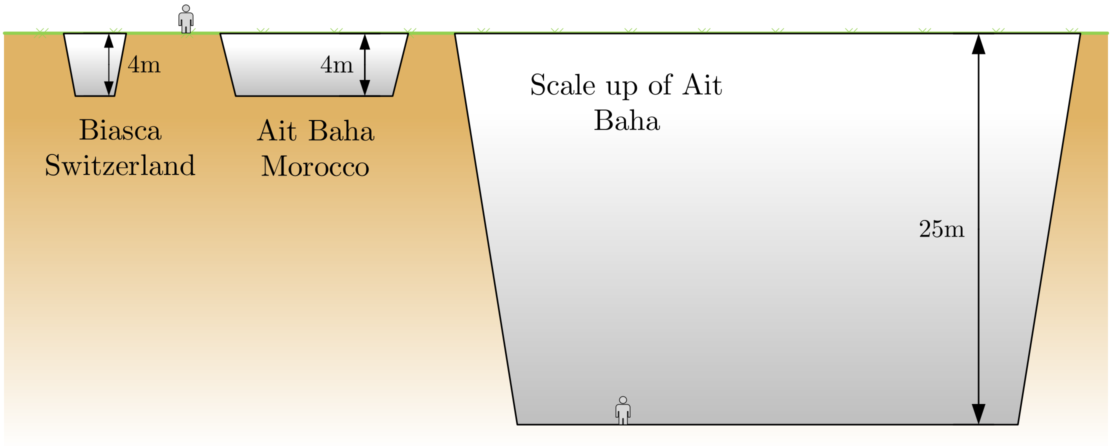

Figure 1.10: Perspective of scaled cone section storages. Adapted from Zanganeh (2014).

Stiesdal (2016a) presented a proposal for an elongated above-ground storage as seen in figure 1.11. This type of storage can be arranged in a u-shape to allow for the auxiliary equipment to be located at one central location. Baffles are placed vertically inside the storage to avoid thermal leakage due to convection in the axial direction and will also secure the storage material if the bed at some point needed to be up-scaled. The advantage of this type of packed bed configuration would be good scalability, where additional length can be added to the packed bed for a higher capacity, and a good thermal front in the storage. A disadvantage of this type is the additional pressure loss, depending of the flow velocity and thus charge rate, as a function of the storage axial length which will require higher pumping work and potentially lower the overall system efficiency.

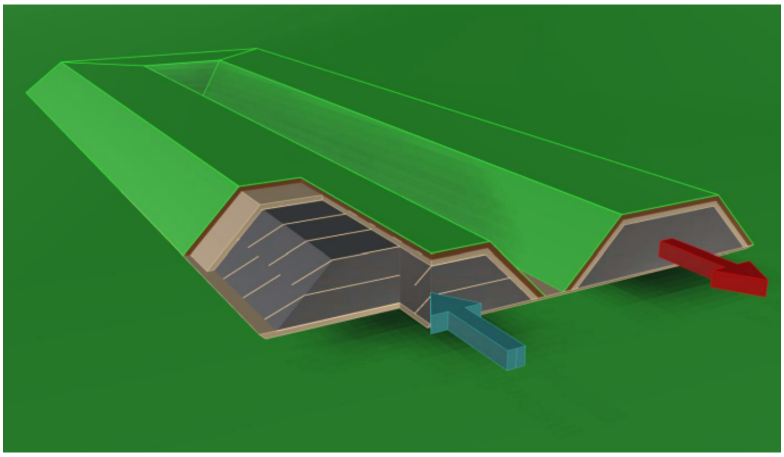

Figure 1.11: Concept for a large scale high-temperature thermal energy storage as proposed by Stiesdal (2016b).

The scale of the proposed storage solution is 250 m in total length, a height of 10 m and a width of 45 m with a total bed volume of $175 \cdot 10^3$ m^3 with a thermal capacity of 17.5 GWh_{th} for discharge from 600°C to 200°C.

From this selection of physical plants currently in use and concepts in development, it becomes clear that high-temperature packed bed thermal energy storage on a large scale is still in the development phase and currently only exist conceptually. In perspective, the thermal capacity of the TES in Ait Baha, which is currently the highest capacity high temperature packed bed storage in use, and the concept of Stiesdal (2016a) differ by a factor of 175.

1.4 Objectives

Based on the previous literature survey and the current state of high-temperature packed bed thermal energy storage technology, this report aims to investigate the future prospects of large scale thermal energy storage. The investigation covers modelling of the thermal energy storage and it's dynamics, the overall system efficiencies as well as considerations of parameters affecting the characteristics and properties of the thermal energy storage and the associated auxiliary system.

"What are the important parameters for efficiency optimisation of a Thermal Energy Storage system?"

The overall goals can be divided into several objectives covering the following aspects:

- *Identify significant geometric-, hydraulic- and thermophysical parameters for the Thermal Energy Storage system.*
- *Determination of the Thermal Energy Storage system important parameters and their optimum values.*
- *Investigate the dynamic behaviour of the Thermal Energy Storage system.*
- *Determination of system first- and second law efficiencies.*
- *Determination of the Thermal Energy Storage system energy capacity.*

Project limitations:

- This investigation is limited to sensible heat Thermal Energy Storage utilising solid storage material.
- The economics and life time aspect of the Thermal Energy Storage system will not be considered.
- The project will only be based on results from the models developed as the physical size of the Thermal Energy Storage system.
- The storage period of the Thermal Energy Storage will not be considered.

2. Thermal Energy Storage (TES)

In this chapter the Thermal Energy Storage will be introduced. The packed bed TES investigated in this study utilises rocks as the storage medium and air as the charging medium. This technology has been widely investigated for Concentrated Solar Power (CSP) plant applications. CSP plants utilise the solar irradiation to heat up a fluid to be used for power generation. A TES can thus be implemented to help distribute the power generation from the peak sun hours to other times of the day. A schematic of a conically shaped TES pilot plant constructed in Ait Baha, Morocco Zanganeh (2014) can be seen in figure 2.1. This storage has a lid diameter of 12 m and is 4 m deep.

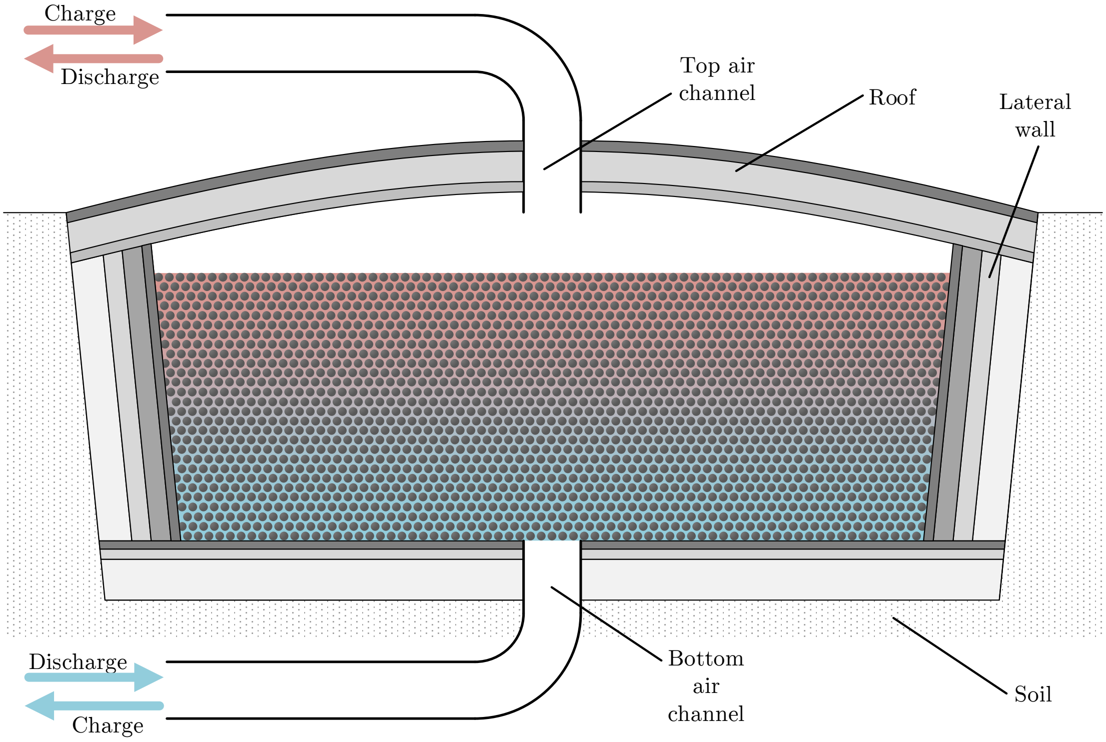

Figure 2.1: A schematic of the 100 MWh_{th} HT-TES geometry for the Ait Baha CSP plant in Morocco. Adapted from Zanganeh (2014).

The packed bed TES utilises rocks of a specific size to provide the required heat capacity for heat storage while maintaining as low a pressure loss for the charge medium as possible. For this study two main properties examined are: The heat distribution in the TES and the pressure loss across the TES. Figure 2.2 shows an illustration of a packed bed consisting of rocks or pebbles with air as the charge medium.

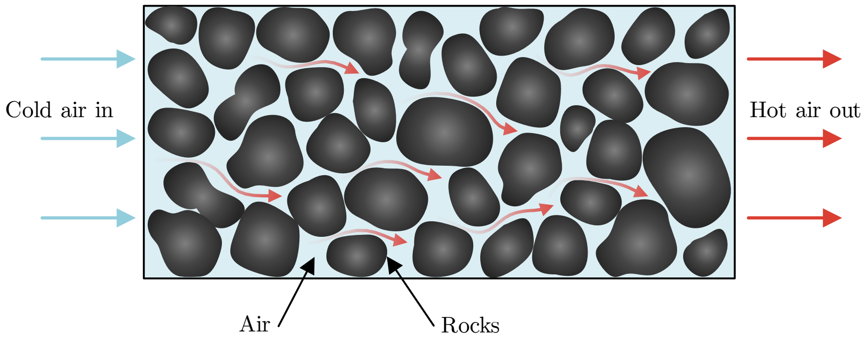

Figure 2.2: Packed bed with air and rock in discharge mode.

The main advantage of this kind of TES is the ability to have a continuous air outlet temperature for prolonged periods of time. To achieve this, the packed bed is charged and discharged from opposite ends of the storage to take advantage of the temperature gradients in the storage.

As cold discharge air flows through the rocks in a fully charged bed, heat is transferred from the rocks to the charge air and the temperature of the air approaches that of the rocks. The rocks near the discharge inlet of the bed are thus cooled while the rocks at the outlet remain at a constant temperature as long as air can be heated to the fully charged rock temperature before it reaches the outlet.

Figure 2.3 shows how a temperature front or profile moves through the bed as a function of the length of the bed and the ratio of the temperature of the rocks T_s to the discharge temperature T_0. During discharge the air inlet is located at $L = 0$ and the front moves towards L = 1. When charging the bed with hot air the flow direction is reversed and the front moves towards $L = 0$ again. This means that the TES does not need to be fully charged before it can be discharged at the same temperature again.

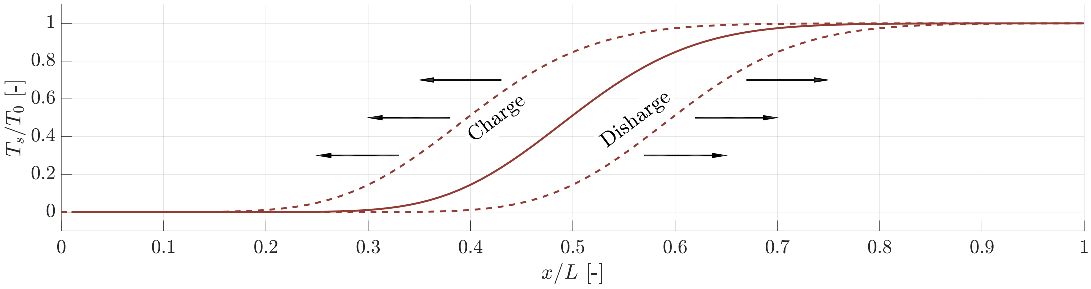

Figure 2.3: Heat front during charging and discharging of the TES.

Similarly to figure 2.3, figure 2.3 shows the effect of varying rock sizes on the temperature gradients in the storage. It can be seen that the smaller rocks yield a steeper temperature gradient allowing for a uniform discharge temperature to be maintained for a longer period compared to larger rocks. Smaller rock sizes do, however, increase the pressure loss across the bed and thus affect the pumping power required and the total system efficiency.

Increasing the length of the bed will have the same effect as decreasing the rock size: The heat front will be shorter compared to the bed length but the pressure loss would also increase.

The pressure loss and heat transfer within the storage are thus interconnected and are both key parameters affecting the overall system efficiency. The storage efficiency will be treated later in section 2.2.

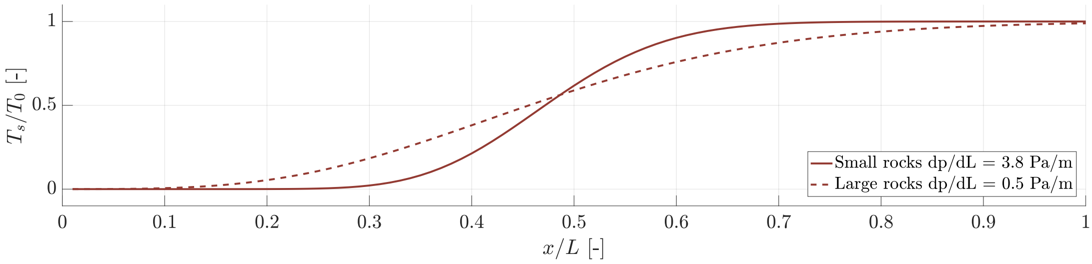

Figure 2.4: Rock size affect the length of the heat front (Sanderson and Cunningham, 1995).

The following section will describe how the TES is modelled and what thermal transport phenomena affects the TES.

2.1 HT-TES model

The developed TES model is a transient, one dimensional and two-phase model that is based on the general Schumann Model (Schumann, 1929). The Schumann model consists of two coupled Partial Differential Equations (PDEs) describing the energy balance of the fluid- and solid phases of a packed bed in relation to time and the axial distance. The original Schumann model is further explained in appendix A. The basic Schumann model is based on the following assumptions:

1. Constant thermal-fluid and solid properties independent of temperature.
2. Steady incompressible flow.
3. No axial heat conduction or radiation.
4. Infinite radial heat conduction and radiation.
5. No temperature gradient in the solid particles *i.e.* low Biot number.

Several of the assumptions listed have been accounted for by implementing extra physical models and properties into the main model:

- Assumption 1 has been accounted for by incorporating thermal properties for air from the NIST REFPROP libraries and fits of the rock heat capacity and thermal conductivity.
- Assumption 2 is accounted for by considering changes in the air density as a function of temperature and pressure utilising the REFPROP implementations from assumption 1.
- Assumption 3 is accounted for by introducing an extra term into the model that takes axial conduction and radiation into account for the solid phase.
- Assumption 4 is not considered in the model as the flow is assumed to evenly distributed over the cross-sectional area of the TES resulting in uniform temperature in the radial coordinate. In reality the loses through the walls will cause some temperature gradient that the model does not account for.
- Assumption 5 is assumed to be true and thus not taken into account in the model. The magnitude of the Biot number will, however, be examined under varying conditions.

The model is mainly based on work done by Zanganeh (2014). The fluid and solid equations are based on an energy balance where the change in energy of either phase is based on the energy flow from or to that phase.

The equation for the fluid phase can be written as:

$$\underbrace{\varepsilon V \rho_f \frac{dh_f}{dt}}_{\text{Fluid enthalpy change}} + \underbrace{\varepsilon V \rho_f v_f \frac{dh_f}{dx}}_{\text{Convection by flow}} = \underbrace{h_{vol} V \left(T_s - T_f\right)}_{\text{fluid-solid phase convection}} - \underbrace{\frac{T_f - T_\infty}{R_{wall}}}_{\text{loss to surroundings}} \tag{2.1}$$

The equation for the solid phase is written as:

$$\underbrace{\left(1-\varepsilon\right)\rho_s V \frac{du_s}{dt}}_{\text{Solid phase capasity}} = - \underbrace{h_{vol} V \left(T_s - T_f\right)}_{\text{fluid-solid phase convection}} + \underbrace{\left[\left(\lambda_{eff} A \frac{dT_s}{dx}\right)_n - \left(\lambda_{eff} A \frac{dT_s}{dx}\right)_{n-1}\right]}_{\text{axial conduction and radiation}} \tag{2.2}$$

where
ε = Packed bed void fraction [−]
V = Packed bed volume [m^2]
Δx = Packed bed length [m]
ρ = Density [kg/m^3]
h = Enthalpy [J/kg]
u = Internal Energy [J/kg]
c_p = Specific heat capacity [J/kg-K]
v_f = Interstitial fluid velocity (between rocks) [m/s]
T = Temperature [K]
h_{vol} = Volumetric convective heat transfer coefficient [W/m^3-K]
R_{wall} = Wall thermal resistance [K/W]
λ_{eff} = Effective conduction coefficient [W/m-K]
with subscripts
f = Fluid phase
s = Solid phase
∞ = Ambient

The convection by flow describes the amount of energy added to or removed from the solid phase by the flow of air through the TES. The fluid-solid phase convection accounts for the energy exchange between the fluid and solid phases while the axial conduction and radiation term accounts for the energy flow caused by the axial temperature difference in the TES. The loss to the surroundings accounts for the loss of energy through the surface of the TES walls.

The void fraction in the equations above is defined as the ratio of volume not occupied by the solid particles to the total volume of the packed bed:

$$\varepsilon = \frac{V_{void}}{V_{total}} \tag{2.3}$$

The interstitial fluid velocity v_f is the average velocity of the fluid in the space between the solid particles defined as:

$$v_f = \frac{\dot{m}}{\varepsilon \rho_f A} \tag{2.4}$$

The two-phase equations are solved by utilising the method of lines (MOL). The MOL requires replacement of the spatial derivatives in equations 2.1 and 2.2 with algebraic equations that approximate the derivatives (Hamdi et al., 2009). This results in the following expression wherein dh_f/dx is approximated by a first order backwards difference scheme:

$$\frac{dh_f}{dx} \approx \frac{h_{f,n} - h_{f,n-1}}{\Delta x} + O\left(\Delta x\right), \;\; 1 \leq n \leq N \tag{2.5}$$

where n is the index of the discretised domain and N is the total number of grid points in the domain. The procedure changes the two PDEs into a set of ODEs that must be solved for the discretised domain of the TES. The discretisation of the axial distance can be seen in figure 2.5 where the storage height is divided into a number of axial grid points. The TES can be modelled as a conical tank as well as a cylindrical tank by defining the top and bottom radii in the model and calculating the geometrical properties of the individual grid points accordingly. These geometrical calculations are further explained in section B.1.

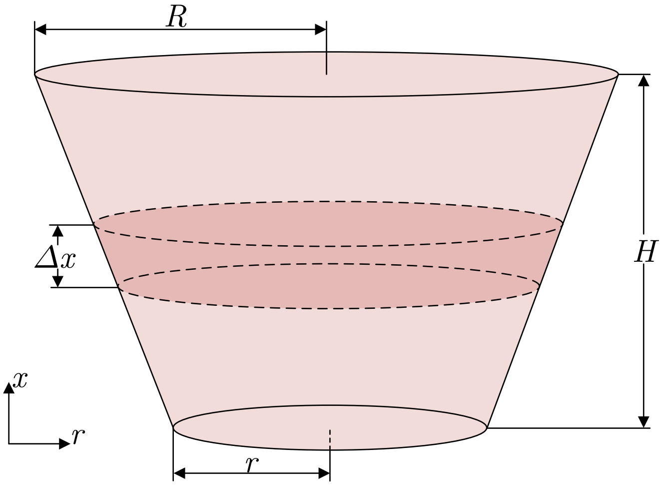

Figure 2.5: Discretisation of the computational domain.

The fully discretised equation for the fluid phase thus becomes:

$$\begin{aligned}\underbrace{\varepsilon V_n \rho_{f,n} \frac{dh_{f,n}}{dt}}_{\text{Fluid enthalpy change}} &= \underbrace{\Big[(\varepsilon A \rho_f v_f h_f)_n - (\varepsilon A \rho_f v_f h_f)_{n-1}\Big]}_{\text{Convection by flow}} + \\ &\underbrace{h_{vol} V_n \left(T_{s,n} - T_{f,n}\right)}_{\text{fluid-solid phase convection}} + \underbrace{\frac{(T_{f,n} - T_\infty)}{R_{wall}}}_{\text{loss to surroundings}}\end{aligned} \tag{2.6}$$

Likewise, the discretisation of the solid phase equation becomes:

$$\begin{aligned}\underbrace{(1-\varepsilon)\,\rho_{s,n} V_n \frac{du_{s,n}}{dt}}_{\text{Solid phase capasity}} = &- \underbrace{h_{vol} V_n \left(T_{s,n} - T_{f,n}\right)}_{\text{Convection by flow}} + \\ &\underbrace{\frac{A_n \lambda_{eff,n}\left(T_{s,n+1} - T_{s,n}\right) - A_{n-1}\lambda_{eff,n-1}\left(T_{s,n} - T_{s,n-1}\right)}{\Delta x}}_{\text{axial conduction and radiation}}\end{aligned} \tag{2.7}$$

where n denotes the grid point. Note that the conduction and radiation term is approximated by a second order central difference scheme as opposed the first order backwards difference scheme used for the convection by flow therm.

In order to solve the two equations the boundary- and initial conditions must be defined. The air inlet temperature $T_{f,n-1}$ at the first grid layer is thus $T_{f,0}$ and defines the temperature of the charge or discharge air as it enters the TES depending on the the direction of the flow. The temperature of the air is related the enthalpy through the REFPROP thermodynamic tables. The boundary condition of the air thus becomes:

$$h_{f,0} = \begin{cases} h_{f,charge} & \text{For the charge phase} \\ h_{f,discharge} & \text{For the discharge phase} \end{cases}$$

The boundary conditions for the temperature gradient of the axial conduction and radiation term in equation 2.7 is set to zero. This implies that, for the first grid layer, the gradient becomes:

$$\frac{(T_{s,1} - T_{s,0})}{\Delta x} = 0$$

Similarly, at the final grid layer, the gradient becomes:

$$\frac{(T_{s,N+1} - T_{s,N})}{\Delta x} = 0$$

The initial condition of the fluid and solid phase is based on an initial temperature that is set for each individual grid point. This means that the initial condition for either phase is a vector of N components containing the individual grid layer temperature. This temperature is then converted into either the respective fluid enthalpy through the NIST REFPROP libraries or into the corresponding internal energy for the solid phase through the relations described in section 2.1.2. With the equations modified to be used with the MOL and the boundaries defined the model can be solved using the MOL.

One of the benefits of using the MOL is that it allows the use of the integrated ODE solvers in MATLAB and Simulink to solve the ODEs. The model is solved in Simulink where each grid point has been represented by a block that incorporates equations 2.6 and 2.7 for the respective grid point. The ode15s solver is used as it have proven to solve the equations more faster and more stable than other of the build in Simulink solvers. The ode15s solver have, however, been limited to time steps of 1000 s to keep the solutions stable as some instabilities have been observed if the solver is allowed to take huge time steps.

The structure in Simulink is established as shown in figure 2.6. Each block receives the necessary property values from the adjacent blocks to solve the fluid and solid phase equations and outputs the values needed for evaluation of the solution.

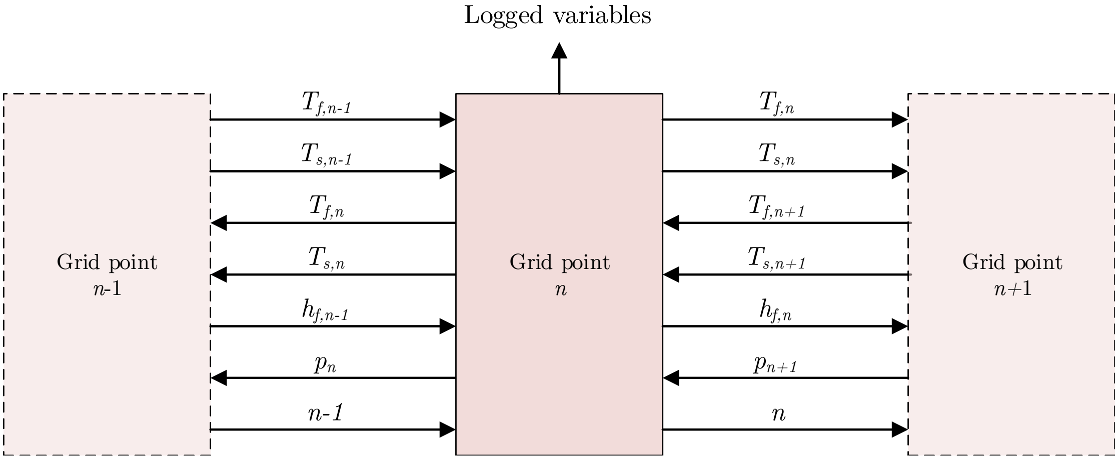

Figure 2.6: Overall Simulink model structure with each grid point represented by a model block with inputs and outputs to its neighbouring grid points.

The internal structure of each grid point is explained in further detail in appendix B.2.

2.1.1 Charge and discharge modelling

The flow of air through the TES is modelled in Simulink in a way that only allows for air flow to move in one direction. In order to model both the charge and discharge cycle, the model discretisation is required to change orientation between simulations. This is illustrated in figure 2.7 where the first grid point during a charge simulation is the roof and subsequently the floor during discharge simulation.

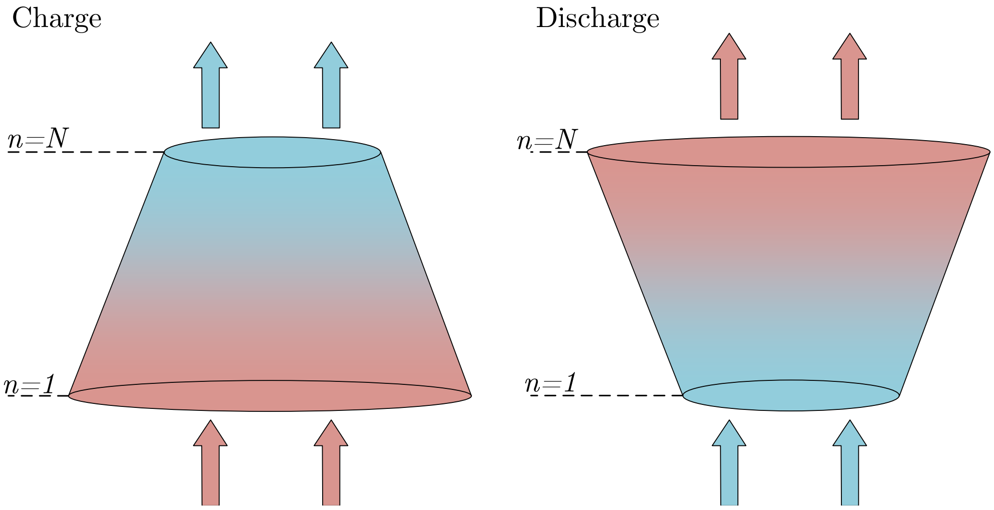

Figure 2.7: Illustration of the geometrical layout of the Simulink model in charge and discharge mode.

As a consequence of this, modelling of continuous charge-discharge cycles require the model to be initialised for an initial temperature that represents the initial TES charge state as well as setting the air inlet boundary condition to the charge temperature. When the charge phase is complete, the end of the charge phase temperature profile through the TES is saved and used as the initial condition for the discharge phase. This, however, requires that the vector containing the temperature for the individual grid points is reversed in order to fit the gradient to allow for the roof grid point of the charge cycle to become the roof grid point of the discharge cycle. This can also be seen from 2.7 where the temperature gradient maintains its orientation in relation to the TES while the flow changes direction.

In the following section the implementation of the temperature dependent properties for the fluid and solid phase is explained. This is followed by the modelling of the major heat transfer mechanisms, **convection**, **conduction** and **radiation**. It covers the modelling of the heat transfer coefficient for the fluid-solid phase convection, the effective conduction coefficient and the overall heat transfer coefficient accounting for the loss to the surroundings.

2.1.2 Temperature dependent properties

The thermal properties for both the fluid phase and solid phase have been implemented to change as a function of temperature. For the fluid phase, all properties are determined for air by implementing lookup tables generated in Matlab by calls to the NIST REFPROP libraries. The air density is determined as a function of temperature and pressure while enthalpy, heat capacity, dynamic viscosity, thermal conductivity and the Prandtl number are determined as a function of temperature only. The only downside to the implementation of variable properties is that each lookup is time consuming and that the resolution of the individual lookup tables have a significant impact on the simulation times. Because of this, the resolution of the tables are as low as possible without it having an effect on the results.

For the solid phase, the heat capacity and conductivity have been implemented as a function of temperature. Both properties have been experimentally determined at lower temperatures and extrapolated using general methods by Zanganeh (2014). The conductivity of the rocks can be determined by the Tikhomirov correlation based on the rock conductivity at 20°C λ_{20} as shown in the following equation (Somerton, 1992):

$$\lambda(T) = \lambda_{20} - A(T-B)(\lambda_{20}-C) \quad for \;\; \lambda_{20} < 2 \;\; W/m-K \tag{2.8}$$

where A, B and C are constants with the values $A = 0.001$, $B = 293$ and $C = 1.38$. This relation fits the tendency of most kinds of rock where the conductivity of the rock decreases with higher temperature. λ_{20} varies for different kinds of rock where an average of 4 W/m-K is used in this investigation. Figure 2.8 shows the Tikhomirov correlation for the thermal conductivity for different starting conductivities, λ_{20}. As there is only a small difference in the conductivities in the relevant operating area, a value of 4 W/m-K for the conductivity *i.e.* the middle of the range, is thus considered reasonable.

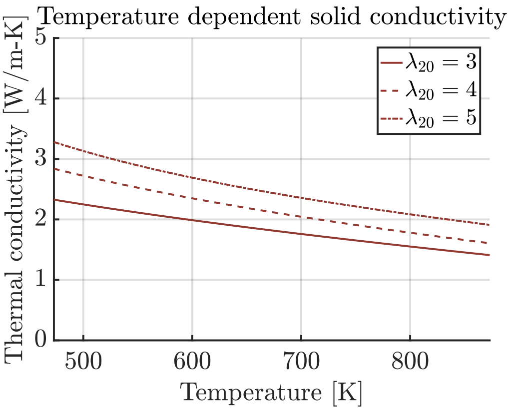

Figure 2.8: The Tikhomirov correlation of the rock thermal conductivity implemented in the model.

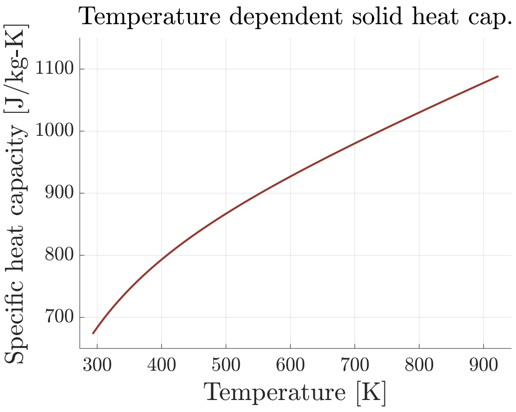

Figure 2.9: The Kelly correlation of the rock heat capacity implemented in the model.

The heat capacity of the rocks is based on the Kelly correlation (Kelly, 1960) and is based on the average of 5 different rock types investigated by Zanganeh (2014). The Kelly correlation is given by:

$$c_s(T) = A\left(B + CT + \frac{D}{T^2}\right) \tag{2.9}$$

where A, B, C and D are constants with the values $A = 705$, $B = 1$, $C = 6.14 \cdot 10^{-4}$ and $D = 1.93 \cdot 10^{4}$ determined by Zanganeh (2014). The rock heat capacity has been plotted in figure 2.9.

In the Simulink model the Kelly correlation for the specific heat capacity of the rocks is implemented as described in appendix C. This implementation is assumed to be the cause of a minor error in the model where the energy balance of the TES based on in- and outflows does not exactly match the energy stored in the TES after simulation is complete. The error is in the range of 1.8% to 4% meaning that up to 4% extra energy is present at the end of a simulation than where added or removed during simulation. As the error is less than 4% it is accepted and later validation of the model will be used to determine the accuracy of the model.

The model has been run with constant thermal properties determined at average temperatures and compared to the variable property model with the implemented lookup tables and fits shown above. The TES in this simulation is a cylindrical TES with a radius of 16 meters and the air mass flow rate is 50 kg/s. The TES is discharged from full capacity at 873 K down to 473 K. The results of the implementation of temperature dependent properties can be seen in figure 2.10.

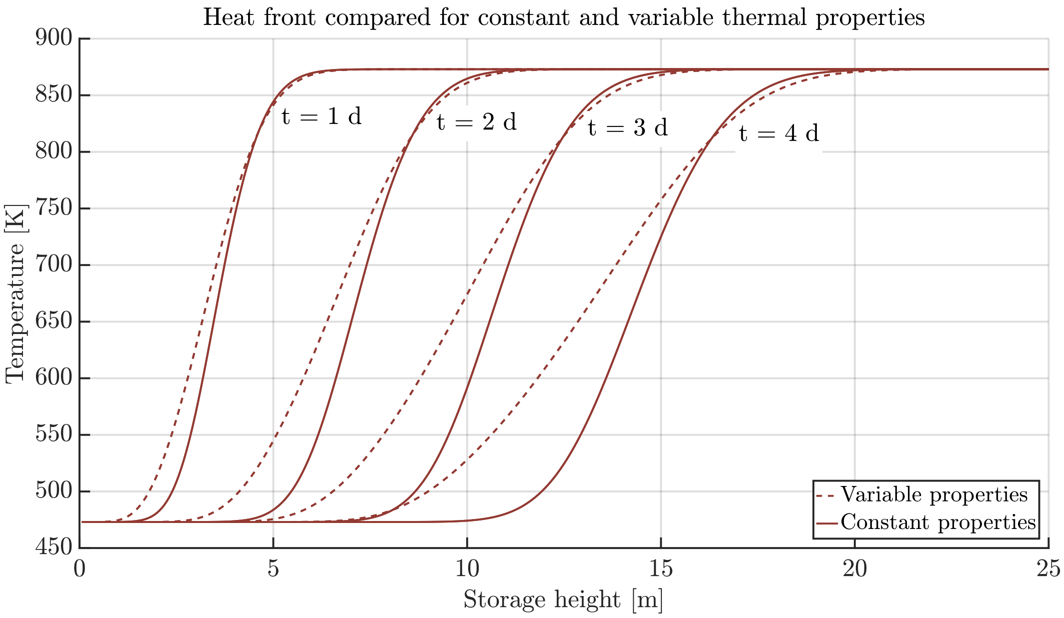

Figure 2.10: The heat front throughout the storage at 1, 2, 3 and 4 days for constant and variable properties.

As can be seen from the figure the heat front becomes much longer when the temperature dependent properties are implemented. The main reason for this change is that the heat capacity of the storage material is greater at higher temperatures with variable properties. This means that more energy has to be removed with variable thermal properties implemented compared to the constant properties. Another effect of the varying thermal properties is that the air velocity is now affected by the temperature which causes a lower flow velocity in the colder regions and a higher velocity in the hotter regions. This affects the fluid-solid phase heat transfer and the pressure loss as these are dependent on the velocity as described in the next section.

2.1.3 Fluid-solid phase convection

The fluid-solid phase convection term accounts for the convective heat transfer between the fluid and the solid phase. The main factor is the convective heat transfer coefficient which, in this study, is expressed by the volumetric heat transfer coefficient h_{vol} which is given by (Coutier and Farber, 1982):

$$h_{\text{vol}} = 700 \left(\frac{G}{d_p} \right)^{0.76} \tag{2.10}$$

where G is the mass flow rate per cross-sectional area $\left[\text{kg/m}^2\text{-s}\right]$ *i.e.* a mass flux, also called the *Core mass velocity*, and d_p is the average solid particle diameter [m]. This relation is valid in the range of $100 < \text{Re}_p < 350$, for temperatures above 373 K and for Biot numbers $\text{Bi} \sim 0.1$. Furthermore, the relation is only valid for particle diameters of $1.8\,\text{cm} < d_p < 3\,\text{cm}$. In this study, the particle Reynolds number Re_p will be less than 100 due to the large cross-sectional area of the TES to the mass flow ratio. Likewise, the particle diameter will be simulated at diameters larger than 3 cm. Zanganeh (2014) compared other relations for the convective heat transfer coefficient by Pfeffer (1964) and Alanis et al. (1977) concluding that the impact on the final model results were negligible.

The Biot number Bi is defined as (Barbour et al., 2015):

$$\text{Bi} = \frac{h_{\text{vol}} d_p}{2 \lambda_p a_p} \tag{2.11}$$

where λ_p is the thermal conductivity of the solid and a_p is the surface areal per volume of the solid $\left[\text{m}^2/\text{m}^3\right]$. The particle Reynolds number is defined as:

$$\text{Re}_p = \frac{G d_p}{\mu} \tag{2.12}$$

where μ is the fluid dynamic viscosity [Pa s].

The Biot number relates the convective heat transfer of the fluid-solid phase to the conductive heat transfer inside the solid. If the Biot number is sufficiently small ($\text{Bi} \ll 1$), the temperature gradient of the solid phase can be neglected in the model. If the Biot number is not sufficiently small the solid phase will not able to either absorb or transfer energy to- or from the fluid at the same rate as the convective heat transfer which is not desirable. TES design parameters affecting the Biot number should, thus, be investigated to keep the Biot number sufficiently small.

2.1.4 Axial conduction and radiation

The axial conduction and radiation describes the energy transfer along the axial direction based on the temperature gradient in the TES. In this study both, the conduction of the solid phase along with the radiation will be taken in to account for the axial displacement of energy.

The radiation for porous media has been investigated by Smith and Kunii (1960) who conclude that the temperature limit at which thermal radiation becomes a significant heat transfer mechanism is mainly for temperatures of 755 K and above. Figure 2.11 shows how rocks at temperatures above 600°C radiates visible light and electromagnetic radiation (Zanganeh, 2014).

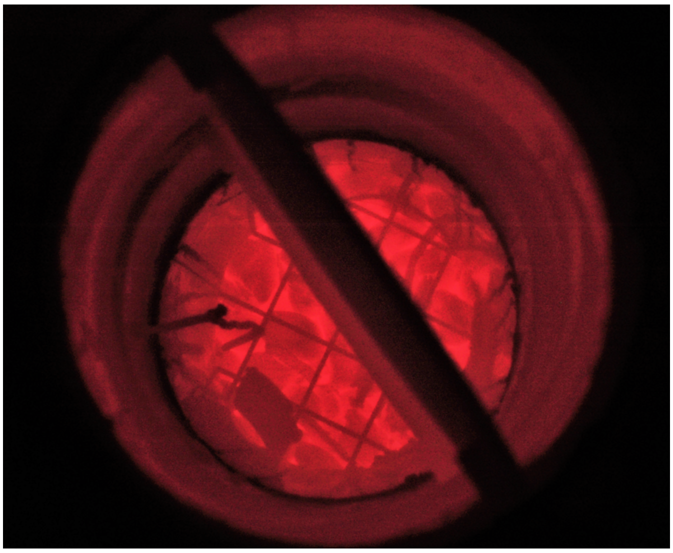

Figure 2.11: Picture taken of rocks at high temperature in the experimental set-up by Zanganeh (2014).

The effective conduction coefficient λ_{eff} used in this study is based on work conducted by Yagi and Kunii (1957) and Smith and Kunii (1960). The effective conduction coefficient takes both the axial conduction of the solid particles and the void fraction into account along with the axial radiation. The effective conductivity is given by:

$$\frac{\lambda_{eff}}{\lambda_f} = \varepsilon\left(1 + \beta\frac{h_{rv}d_p}{\lambda_f}\right) + \frac{\beta\left(1-\varepsilon\right)}{\dfrac{1}{\dfrac{1}{\phi} + \dfrac{h_{rs}d_p}{\lambda_f}} + \dfrac{\lambda_f}{\lambda_s}} \tag{2.13}$$

where β is the ratio of the average distance between two neighbouring solid particles and the diameter of the particles. The minimum and maximum values of this ratio is $\beta = 0.82$ for loosely packed beds and $\beta = 1.0$ for a tightly packed bed. Here, an average value of 0.9 is used as the packing is assumed to be between the two extremes. d_p is the solid particle diameter and γ is the ratio of effective length of the solid relating to thermal conduction to solid particle diameter $\gamma = 2/3$. ϵ is the solid emissivity assumed to be 0.85. ϕ is the ratio of the effective thickness of the fluid film, related to the heat transfer through the fluid film adjacent to the solid particles represented by 5 in figure 2.12. h_{rv} is the void to void radiative heat transfer coefficient represented by 3 in figure

2.12. h_{rs} is the solid surface to solid surface radiative heat transfer coefficient represented by 3 in figure 2.12 (Yagi and Kunii, 1957). The calculation of ϕ, h_{rv} and h_{rs} is shown is shown appendix D.1.

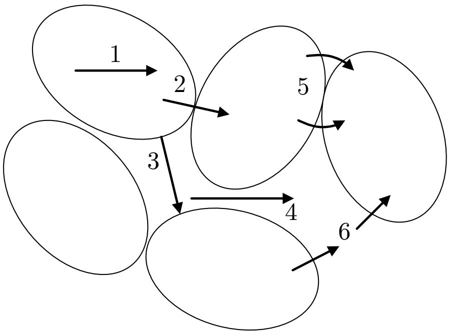

Figure 2.12: Mechanisms of heat transfer in a packed bed. 1, conduction through the solid particles. 2, conduction through the solid particle interfaces. 3, radiation between solid particles. 4, radiation from void to void. 5, heat transfer through the fluid film adjacent to the solid particles. 6, fluid-solid phase convection. (Adapted fromSmith and Kunii (1960)).

Conduction and radiation effects

The effect of implementing the axial conduction into the model can be seen in figure 2.13. Here, the model has been run for a TES height of 25 m and a radius of 16 m. The TES is discharged from 873 K with air at 473 K and a mass flow rate of 50 kg/s. As it can be seen the implementation of axial conduction and radiation has a small effect on the results. The inclusion of axial conduction and radiation affects the length of the heat front. As heat is transferred form hotter parts of the TES to the colder parts the heat front becomes longer and the gradient less steep.

The effect of the axial conduction is, however, also related to the air mass flow rate and the cross sectional area of the storage. A storage with a large heat capacity and a low charge or discharge rate will be affected to a higher degree as the energy transferred by the flow becomes smaller compared to the energy transferred axially by conduction and radiation.

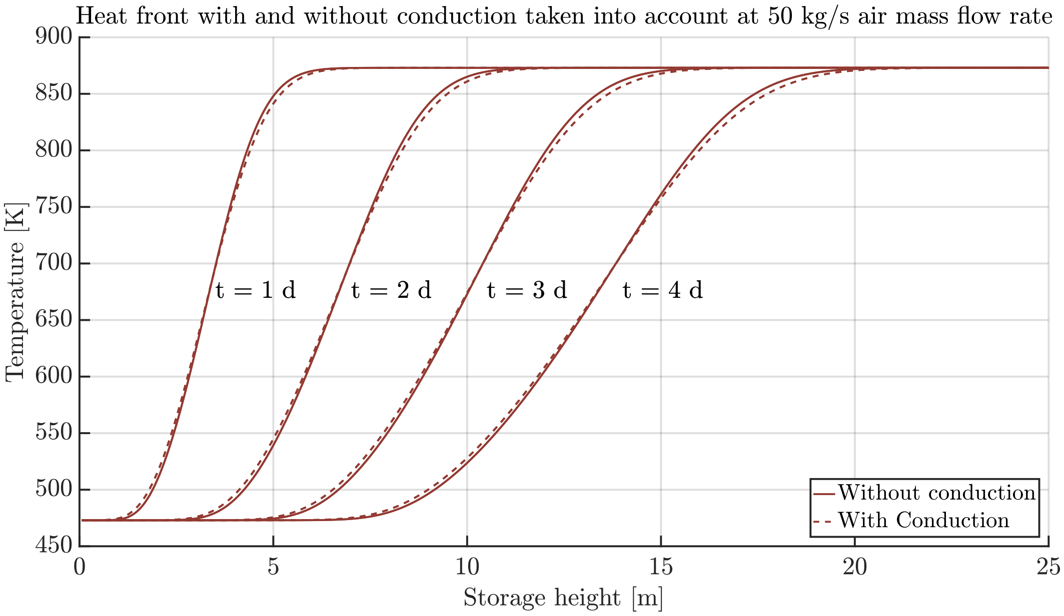

Figure 2.13: The heat front throughout the storage at 1, 2, 3 and 4 days with and without axial conduction.

2.1.5 Thermal losses

The thermal losses to the surroundings are accounted for by introducing a loss term into equation 2.1. The thermal losses are split into the loss through the lateral walls of the TES, the roof and the floor of the TES. These losses are treated in different ways but are all based on the amount of insulation in the respective section. The amount and type of insulation used in the model is based on an existing TES pilot plant and a scaled up version proposed by Zanganeh (2014). The model utilises several different types of insulation materials with different properties. The insulation materials are chosen based on materials used for the Ait Baha pilot plant and include Ultra High Performance Concrete (UHPC), Low density Concrete (LDC) and two types of commercially available insulation, namely Microtherm® and Foamglas®. Furthermore, a layer of soil of 20 cm is also used in some simulations as part of the the insulation for the walls and floor. The base insulation thickness for the different types of insulation and for the relevant sections of the TES can be seen in table 2.1.

	Layer thickness [m]				
	UHPC	LDC	Microtherm®	Foamglas®	Soil
Roof	0.02	0.7	0.6	0.5	0.0
Wall	0.02	1	0.3	0.5	0.2
Floor	0.02	0.48	0	0.4	0.2

Table 2.1: Insulation layers and thickness used to determine the thermal losses in the TES (Zanganeh, 2014).

The thermal conductivity of the five different materials used throughout this study is shown in table 2.2.

	Thermal conductivity [W/m-K]
UHPC	2
LDC	0.375
Microtherm®	0.025
Foamglas®	0.05
Soil	0.5

Table 2.2: Thermal conductivities for the different materials used in the TES model (Zanganeh, 2014).

From table 2.2 it can be observed that Microtherm® and Foamglas® provide the insulation of the TES while the two concrete types are not used strictly for insulation purposes but are part of the structural integrity of the TES.

Model implementation of thermal losses

The losses through the wall, roof and floor of the TES are implemented differently into the model. The wall loss applies to all grid layers of the model while the floor and roof loss is only present at grid point 0 and grid point N. The first grid point, grid point 0, represents the floor when the model is in discharge mode and the roof when the model is in charge mode as illustrated in figure 2.7. The opposite is true for the Nth grid point.

The wall loss is implemented for all grid points as in equation equation 2.1. The wall thermal resistance R_{wall} is further explained in appendix D.2.1

The loss through the roof $\dot{q}_{roof}$ is only considered for the roof grid layer. The loss is implemented in this cell as an extra term in the fluid phase equation resulting in the following discretised equations for the roof fluid phase grid point:

$$\begin{aligned}\underbrace{\varepsilon V_n \rho_{f,n} \frac{dh_{f,n}}{dt}}_{\text{Fluid enthalpy change}} &= \underbrace{\Big[(\varepsilon A \rho_f v_f h_f)_n - (\varepsilon A \rho_f v_f h_f)_{n-1}\Big]}_{\text{Convection by flow}} + \\ &\qquad \underbrace{h_{vol} V_n \left(T_{s,n} - T_{f,n}\right)}_{\text{fluid-solid phase convection}} - \underbrace{\frac{(T_{f,n} - T_\infty)}{R_{wall}}}_{\text{loss to surroundings}} - \underbrace{\dot{q}_{roof}}_{\text{roof loss}} \qquad (2.14)\end{aligned}$$

where $n = 1$ for a charge simulation and $n = N$ for a discharge simulation. The detailed calculation of $\dot{q}_{roof}$ is described in appendix D.2.2. The loss for the floor is similarly shown in the discretised equation of the fluid-phase floor grid point.

$$\underbrace{\varepsilon V_n \rho_{f,n} \frac{dh_{f,n}}{dt}}_{\text{Fluid enthalpy change}} = \underbrace{\left[(\varepsilon A \rho_f v_f h_f)_n - (\varepsilon A \rho_f v_f h_f)_{n-1}\right]}_{\text{Convection by flow}} + \underbrace{h_{vol} V_n \left(T_{s,n} - T_{f,n}\right)}_{\text{fluid-solid phase convection}} - \underbrace{\frac{(T_{f,n} - T_\infty)}{R_{wall}}}_{\text{loss to surroundings}} - \underbrace{\frac{(T_{f,n} - T_\infty)}{R_{floor}}}_{\text{floor loss}} \tag{2.15}$$

where $n = N$ for in a charge simulation and $n = 1$ for a discharge simulation according to figure 2.7 R_{floor} is explained in further detail in appendix D.2.3.

2.1.6 Pressure loss

The pressure loss through the TES is of key importance when considering the losses associated with pumping of air through the rock bed. The pressure loss is calculated at each grid point in the model utilising the empirical Ergun equation developed for determining pressure losses through packed beds (Ergun and Orning, 1949):

$$\Delta p = \frac{\Delta x G_{f,n}^2}{\rho_{f,n} d_p} \left(A \underbrace{\frac{(1-\varepsilon)^2}{\varepsilon^3 \Psi} \frac{\mu_{f,n}}{G_{f,n} d_p}}_{\text{viscous}} + B \underbrace{\frac{1-\varepsilon}{\varepsilon^3 \Psi}}_{\text{kinetic}} \right) + \underbrace{\rho_f g \Delta x \frac{\Delta T}{T_{f,n}}}_{\text{buoyancy}} \tag{2.16}$$

where Ψ is the sphericity of the rocks in the TES, assumed to be 0.6. ΔT is the temperature difference across the grid layer and g is the gravitational constant. The equation is composed of two terms that accounts for the viscous and inertial losses of the flow. The Ergun equation is modified with a buoyancy term to account for the pressure loss caused by the temperature difference in the TES as proposed by Andersen (2003). Furthermore, the Ergun equation is modified with constants $A = 217$ and $B = 1.83$ which improves the accuracy of the pressure loss for randomly shaped particles (Macdonald et al., 1979).

2.2 TES efficiency

In this section, the energy- (first law) and exergy (second law) efficiencies will be used to evaluate the performance of a given TES along with the fraction of energy lost to the surroundings and the fraction of energy used to power the fan that pumps the air through the TES. These are defined in order to calculate the efficiencies and loss fractions for a charge-discharge cycle *i.e.* a simulated charge period followed by a simulated discharge period.

Exergy is defined as the quality of energy or the energy available to do useful work. This follows from the second law of thermodynamics stating that the quality of some amount of energy used to drive a process is reduced when work is performed. Thus, the entropy increases while the exergy decreases. This is linked to the inherent irreversibilities of all real processes.

Traditional ways of evaluating efficiencies are based on energy efficiency. Being highly temperature dependent, the Thermal Energy Storage depends not only on the quantity of energy but also the quality of the energy transferred to and from the storage. Evaluating the TES efficiency based solely on the energy efficiency can be misleading because the first law energy efficiency considers all transferred thermal energy equally. The exergy efficiency takes into account the quality and thus the temperature of the thermal energy when evaluating the TES efficiency. Because generation of useful steam for power generation generally requires higher temperatures, the exergy- or second law efficiency is a convenient method for efficiency evaluation and TES comparison when linked with a traditional energy- or first law analysis (Dincer and Rosen, 2010).

Krane (1987) discusses the importance of exergy considerations in relation to Thermal Energy Storage and concludes that the purpose of a TES is not store energy alone but exergy *i.e.* thermodynamic availability. The author also underlines the importance of the consideration of not only the storage itself but any associated auxiliary equipment such as charge and discharge cycles.

The energy or *First Law* efficiency for a steady state system is often defined as (Dincer and Rosen, 2010):

$$\eta = \frac{\text{Energy in product outputs}}{\text{Energy in inputs}} \tag{2.17}$$

The energy efficiency describes the total amount of energy extracted by the TES system in the form of electricity and/or heat.

The exergy or *Second Law* efficiency is defined as (Dincer and Rosen, 2010):

$$\psi = \frac{\text{Exergy in product outputs}}{\text{Exergy in inputs}} \tag{2.18}$$

The exergy efficiency ψ thus describes the usefulness of the energy extracted from the TES system in the form of electricity and/or heat.

First law efficiency

The overall charge-discharge cycle first law or energy efficiency of the TES can be expressed by re-writing equation 2.17 as (Rezaie et al., 2012)

$$\eta_{cycle} = \frac{E_{recovered} - E_{fan,discharge}}{E_{input} + E_{fan,charge}} \tag{2.19}$$

where $E_{recovered}$ is the amount of energy recovered during the discharge period, given in equation E.1, and E_{input} is the energy added to the TES during a charge period. $E_{fan,charge}$ is the fan power required over the charge period to power the fan based on the fan power $E_{pump} = \dot{V}\Delta p$. This is done assuming that the flow is incompressible and taking assuming an electric efficiency of the fan to be 95%. $E_{fan,discharge}$ is the amount of thermal energy the TES has to provide for the Rankine-cycle in order for the fan to run of the electricity generated by the Rankine-cycle. This means that the thermal efficiency of the Rankine-cycle has to be taken into account. From section 3.1.2, an average of 35% is used.

Due to this definition, the required fan power during the discharge period will originate from the Rankine power cycle and thus lower the discharge efficiency compared to the charge period because the electricity required for pumping during the charge period will be provided by the electrical grid. The equations for $E_{recovered}$, $E_{fan,discharge}$, E_{input} and $E_{fan,charge}$ are found in appendix E

Second law efficiency

The second law or exergy efficiency is expressed using enthalpies while the overall exergy efficiency is expressed in the same manner as the energy efficiency(Rezaie et al., 2012)

$$\psi_{cycle} = \frac{Ex_{recovered} - Ex_{fan,discharge}}{Ex_{input} + Ex_{fan,charge}} \tag{2.20}$$

where Ex_{input} is the exergy input during a charge period and $Ex_{recovered}$ is the exergy recovered during a discharge period. $Ex_{fan,discharge}$ and $Ex_{fan,charge}$ is the exergy required during discharge and charge respectively and is subject to the same assumptions made for equation 2.19. The equations for Ex_{input}, $Ex_{recovered}$, $Ex_{fan,discharge}$ and $Ex_{fan,charge}$ can be found in appendix E.

Loss fractions

The energy lost to the surroundings and the energy used to drive the fan during the charge and discharge periods is measured relative to the amount of energy added to the system over a charge-discharge cycle. The fraction of energy used to drive the fan f_{fan} is calculated as (Zanganeh, 2014):

$$f_{fan} = \frac{E_{fan,charge} + E_{fan,discharge}}{E_{recovered}} \tag{2.21}$$

The loss fraction of the thermal loss through the TES surfaces is calculated as (Zanganeh, 2014):

$$f_{thermal} = \frac{E_{Floor\,loss,cycle} + E_{wall\,loss,cycle} + E_{roof\,loss,cycle}}{E_{recovered}} \tag{2.22}$$

where $E_{Floor\,loss,cycle}$, $E_{wall\,loss,cycle}$ and $E_{roof\,loss,cycle}$ are the thermal losses through the floor, wall and roof of the TES respectively.

2.3 Model validation

In this section the model will be validated in two different ways: Firstly, a grid independence study is carried out in order to ensure that the resolution of the discretised

TES domain is high enough to prevent the grid resolution to have an effect on the model results. Secondly, the model will be compared to simulations performed by Zanganeh (2014) to determine if the model performs similarly to the theory on which it is based.

2.3.1 Grid independence study

In order to determine number of grid points necessary for a grid independent solution, the model has been run at 100, 200, 400 and 800 grid points for a cylindrical TES with a height of 26 meters and a radius of 16 meters based on the up-scaled 7.2 GWh conical TES as presented by Zanganeh (2014). The simulation is carried out for a fully charged TES at 873 K that is discharged using air at an inlet temperature of 473 K and a mass flow rate of 133 kg/s. The simulation is run for 2 days at which point the air temperature at the outlet begins to decrease under these conditions. The loss to the surroundings has been omitted in this simulation as the convection of the flow is the major property that affects the amount of grid points needed. Figure 2.14 shows the results of the four different numbers of grid points at 0.5, 1, 1.5 and 2 days of discharge.

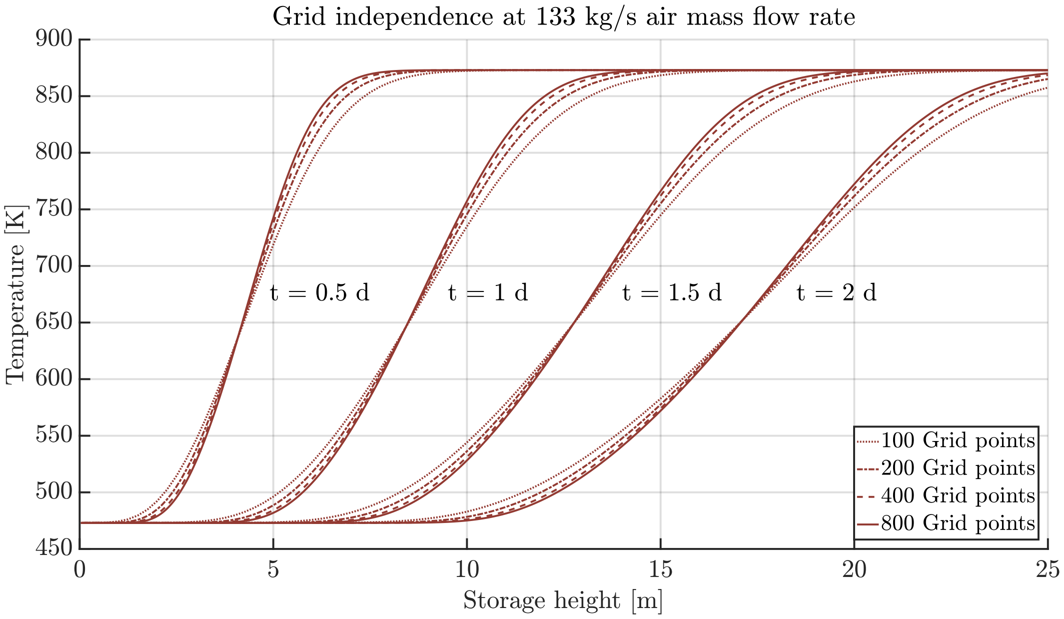

Figure 2.14: The heat front throughout the storage at 0.5, 1, 1.5 and 2 days for 100, 200, 400 and 800 grid points.

As can be seen from figure 2.14, the overall difference in number of grid points is not significant. The difference between 800 and 400 grid points is almost negligible and 400 grid points provides sufficient accuracy for further studies. Furthermore, computation times are significantly lower at 400 grid points compared to 800 grid points. In the following section, results generated by the developed model will be compared to model results obtained by Zanganeh (2014) from a model similarly based on 400 grid points.

2.3.2 Validation

In order to validate the developed model, the results are compared to results obtained by Zanganeh (2014). In order to do this, one of the studies conducted by Zanganeh (2014) is replicated. As the model is originally created for a CSP plant, the TES is used to store energy every day during the sunny hours and discharged during the night. For this, Zanganeh (2014) conducted a study where in the model is cycled through 30 days with 8 hours of charging followed by 16 hours of discharging. This means that the model will have to simulate 30 continuous days in alternating charge and discharge mode. Because even small differences in the modelling results will accumulate over longer simulation times, the chosen case is ideal for model validation.

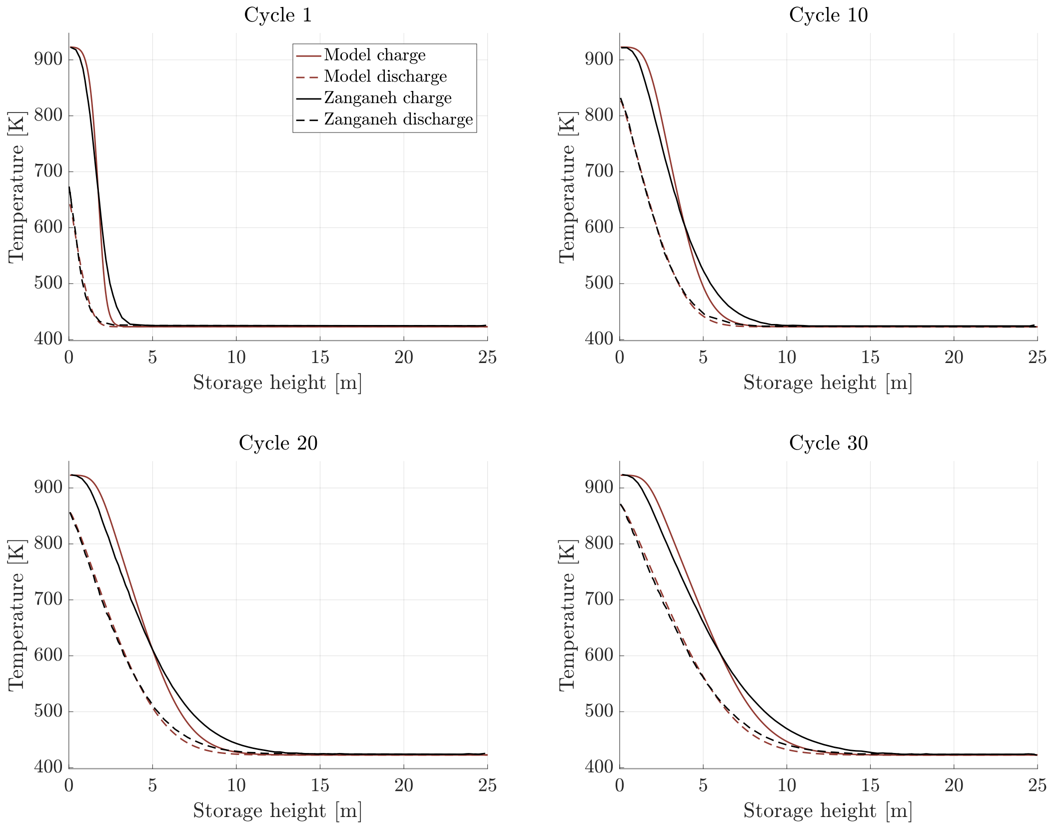

Figure 2.15: Result of the cyclic model over 30 days from the simulation conducted with the model build for this study and data from Zanganeh (2014).

The model is run with parameters similar to those of the up-scaled, conical 7.2 GWh TES investigated by Zanganeh (2014) with a height of 25 meters, a bottom radius of 16 meters and a top radius of 20 meters. The TES is charged from 423 K to 923 K with an air flow rate of 133 kg/s and discharged with air at 423 K with an air flow rate of 66 kg/s. The insulation materials used in the simulation are identical to the TES investigated by Zanganeh (2014). The insulation is composed of four different materials and the walls the roof and the floor insulation thicknesses are modelled as as listed in 2.1.

Figure 2.15 shows the results at charge-discharge cycles 1, 10, 20 and 30 as results from identical points are provided by Zanganeh (2014).

The comparison reveals that the charge behaviour of the two models deviate slightly. The discharge behaviours do, however, fit well when plotted side by side. One explanation of the deviations could be partly explained by errors in the capturing of data from Zanganeh (2014), which has been performed manually from plots using data capturing software to obtain data points for validation and might, therefore, be prone to some uncertainties.

From the model result comparisons, it was observed that the heat front gradient of the modelled TES after each charge cycle is steeper compared to the original model developed by Zanganeh (2014). The following discharge cycle, though, seems to capture the same heat distribution as the original model. A reason for the difference in the models could be explained by an error in the implementation of the specific heat capacity of the rocks. Despite this, 30 consecutive runs of the model does not seem to result in any accumulative error. Overall, the differences between the models are reasonably small and as the final outlet temperatures are identical within a small margin as described above, the model is considered validated for further studies of the TES behaviour.

2.4 TES model conclusion

This concludes the description of the TES model. The model is based on the original packed bed Schumann model and modified to address several assumptions of the original Schumann model. The implementation of temperature dependent properties causes the largest difference compared to constant thermal properties for the fluid and solid phases while the implementation of axial conduction and radiation have a minor effect on the heat front. Both the temperature dependent thermal properties and the conduction and radiation do, however, contribute to creating a longer heat front with a smaller gradient that will have a negative effect on the overall TES performance. The model has been validated using data obtained from a similar model developed by Zanganeh (2014) for 30 thermal cycles. The model is considered validated despite small deviations in the charge cycle temperature profiles of the compared models.

3. Auxiliary system

The auxiliary system in this investigation covers the discharge cycle of the TES as well as the steam Rankine cycle that produces power from heat delivered by the discharge cycle. The auxiliary system is highlighted in figure 3.1. The connection between the charge cycle and the steam Rankine cycle is the charge air boiler used for steam generation. The pressure loss trough this boiler is a key factor in determining the overall efficiency of the combined TES system efficiency.

The total heat exchanger area must be known in order to determine the pressure loss. This, in turn, along with the Rankine cycle power output, is then used to determine the overall TES system efficiency. Two steam Rankine cycle (SRC) configurations are modelled in this investigation: a single- and a dual pressure configuration. A brief parametric study of the single pressure cycle is conducted to investigate the general tendencies of parameters such as the thermal efficiency and shaft work of the cycle. The general Rankine cycle model inputs and constraints are presented for later cycle optimisation.

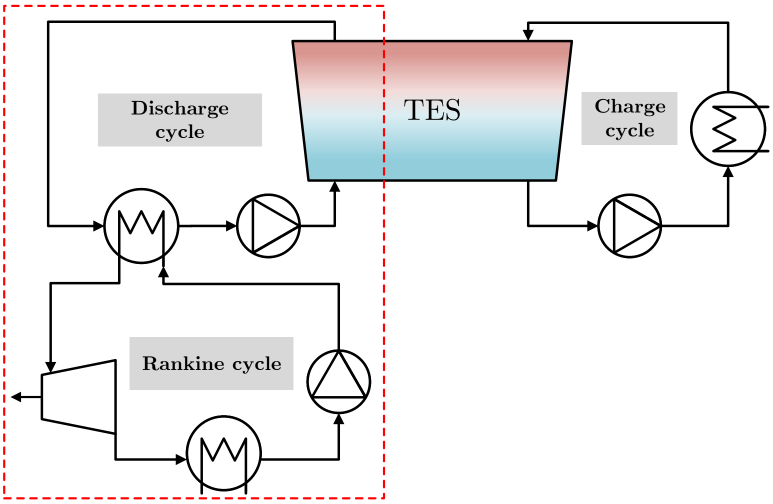

Figure 3.1: The TES system with the relevant parts of the auxiliary system highlighted in red.

The modelling of the discharge cycle is presented next, which covers the calculation of the pressure loss across the boiler. The pressure loss is investigated as a function of the number of boiler tubes, for various tube configurations *i.e.* pitch ratios as well as for varying dimensions of the boiler casing. For evaluation of the investigated boiler configurations, the *efficiency index* is utilised to account for the ratio of heat transfer to pressure loss through the boiler, the two most prominent properties of heat exchanger performance. The treatment of charge and discharge air fans will be limited to practical considerations in the end of this report and, thus, modelling of these is not considered beyond calculation of the necessary pumping power.

Note that the charge cycle is not treated in detail in this investigation. Instead, the charge efficiency of the electrical heater is set to 100% assuming that all the electrical energy is converted to useful heat. The fan efficiencies for both the charge and discharge air cycles are set to 95%.

3.1 Steam Rankine cycle

The Steam Rankine cycle (SRC) is currently one of the most common power cycles for electricity generation. It works on the principle of condensation and evaporation of water. Depending the operating pressure the cycle can work in the sub-critical-, supercritical- and ultra super-critical range with cycle pressures ranging from approximately 50 bar to above 300 bar(Burmeister & Wain, 2016). The system consists of four general components: a feed water pump, a boiler, a steam turbine and a condenser. In a real system, several other components such as valves and steam drums will also be present.

In the following, modelling, parametric studies and optimisation of a simple Single Pressure (SP) and a Dual Pressure (DP) Rankine cycle is presented.

From figure 3.4 and 3.2, the operation of the general single pressure Rankine cycle can be described by from the following points:

- Point 1 to point 2 describes an adiabatic compression by the feed water pump to the operational pressure. The points are located relatively close because the isobaric lines are closely spaced due to the incompressibility of a sub-cooled liquid.
- Point 2 to 3 describes an, ideally, isobaric heating of the water to the saturation temperature at the specific pressure.
- Point 3 to 4 describes isothermal and, ideally, isobaric evaporation of the water until a saturated state is reached in point 4.
- From point 4 to 5, the steam undergoes super heating under isobaric conditions.
- From point 5 to 6, the steam undergoes adiabatic expansion down to the condenser pressure, in most practical cases reaching a point below the saturation curve. In the process, the energy is extracted and converted to mechanical energy in the steam turbine.
- From point 6 to 1, the saturated vapour is condensed under essentially isobaric and isothermal conditions and the cycle repeats.

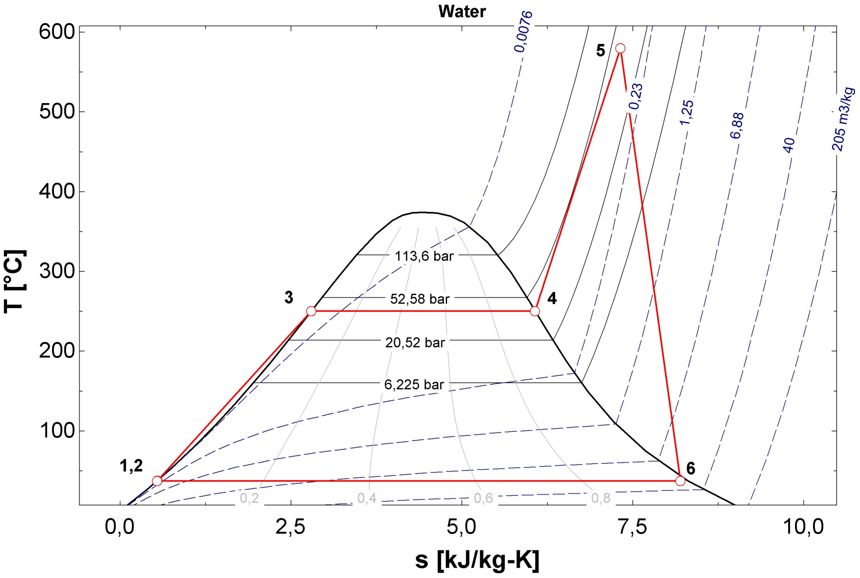

Figure 3.2: A T-s diagram for a simple single pressure steam rankine cycle.

3.1.1 Rankine cycle modelling

The Rankine cycles are modelled using Engineering Equation Solver based on general equations for energy- and mass balances. The heat exchanger areas are treated as free parameters and can be treated as the inputs to the boiler pressure loss model developed in section 3.2.

Energy balances for each component are found from a combination of thermophysical properties such as temperature, pressure and enthalpies. The general heat balances for the Rankine cycle components are defined according to:

$$\dot{Q} = \dot{m} \cdot \Delta h \tag{3.1}$$

where $\dot{m}$ is the mass flow rate of the relevant stream and Δh is the difference in enthalpies for the in- and output of the relevant component. The EES model calculates the heat exchanger areas based on the amount of heat extracted as well as the set logarithmic temperature differences:

$$\dot{Q} = UA\Delta T_{\text{LMTD}} \tag{3.2}$$

where U is the overall heat transfer coefficients chosen based on typical values the respective heat exchangers, A is the heat transfer areas. T_{LMTD} is the logarithmic mean temperature difference which, for a counter-current heat exchanger, is defined as:

$$T_{\text{LMTD}} = \frac{(T_{\text{hot,in}} - T_{\text{cold,out}}) - (T_{\text{hot,out}} - T_{\text{cold,in}})}{ln\left(\frac{(T_{\text{hot,in}} - T_{\text{cold,out}})}{(T_{\text{hot,out}} - T_{\text{cold,in}})}\right)} \tag{3.3}$$

The heat that can be extracted from the discharge air is governed by the charge air mass flow and temperature, pinch temperatures in the heat exchangers and the desired steam pressure and temperature. The desired steam temperature must not exceed the saturation pressure for the desired steam pressure. The mass flow of steam generated is governed by the desired steam pressure for the turbine with lower pressures yielding more steam at a lower quality.

The pump work is calculated as:

$$W_{\text{pump}} = \Delta p \cdot \dot{V} \cdot \eta_{\text{pump}} \tag{3.4}$$

where Δp is the total pressure difference across the pump, $\dot{V}$ is the volumetric flow rate and η_{pump} is the pump efficiency which is assumed to be 0.8.

The isentropic steam turbine efficiency is described by the following equation:

$$\eta_s = \frac{h_1 - h_{2a}}{h_1 - h_{2s}} \tag{3.5}$$

where the enthalpies correspond to figure 3.3 and η_s is the turbine efficiency assumed to be 0.8. The equation is used to determine the entropy at the turbine exit in order to determine the actual turbine work.

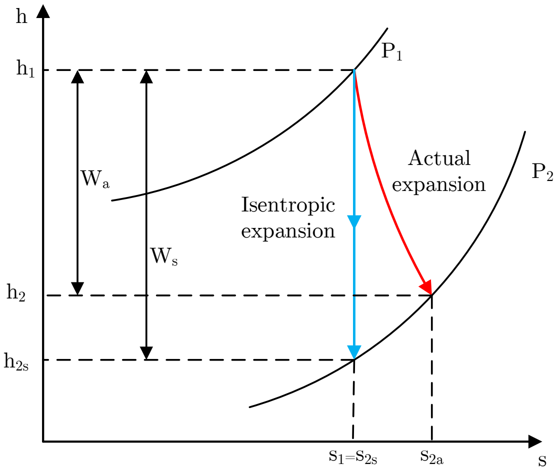

Figure 3.3: The ideal, isentropic expansion in a steam turbine and the real actual, irreversible expansion process.

The thermal energy efficiency or first law efficiency of the steam Rankine cycle is defined as the ratio of work extracted by the steam turbine to the heat absorbed by the heat exchangers:

$$\eta_{th} = \frac{W_{net}}{Q_{in}} = \frac{W_{turb} - W_{pump}}{Q_{in}} \tag{3.6}$$

The exergy- or second law efficiency of the steam Rankine cycle is defined as the ratio of the reversible (Carnot) efficiency of the cycle to the thermal efficiency as follows (Cengel and Boles, 2015):

$$\psi = \frac{\eta_{rev}}{\eta_{th}} \tag{3.7}$$

The general reversible or Carnot efficiency is defined as:

$$\eta_{rev} = \frac{T_{cond,in}}{T_{charge,in}} \tag{3.8}$$

where $T_{cond,in}$ is the cooling water temperature in the condenser, the heat sink, and $T_{charge,in}$ is the charge air temperature *i.e.* the inlet temperature to the boiler, the heat source. The exergy efficiency thus describes the ratio of thermodynamic potential which is utilised by the power cycle.

The steam turbine is dependent on a constant condenser pressure as well as inlet parameters such as the desired inlet steam pressure and temperature as well as the turbine efficiencies. In the current models, pressure loss on both the tube and shell side of the heat exchangers are neglected for simplicity.

There are several adjustable parameters to increase the turbine work. Some of these include:

- Desired steam temperature and pressure, T_{steam} and P_{steam}.
- Condenser temperature and pressure, T_{cond} and P_{cond}. These parameters are governed by the available cooling options at the installation site of the plant.
- Charge air temperature and mass flow rate, T_{charge} and $\dot{m}_{\text{charge}}$.
- The pinch temperatures between the charge air stream and steam, T_{pinch}.

Two basic configurations of the steam Rankine cycle are modelled in this investigation: a Single Pressure- and a Dual Pressure steam Rankine cycle as presented in the following.

3.1.2 Single pressure steam Rankine cycle

The single pressure Rankine cycle is the simplest steam power cycle and is modelled in order to investigate the tendencies and effects of adjusting parameters such as the cycle pressure. In practice, a real steam Rankine cycle for electricity production produces steam at several pressure levels fed to individual turbine stages. The cycle pressure governs the saturation temperature of the cycle and thus has a critical role in controlling the average heat transfer to the cycle.

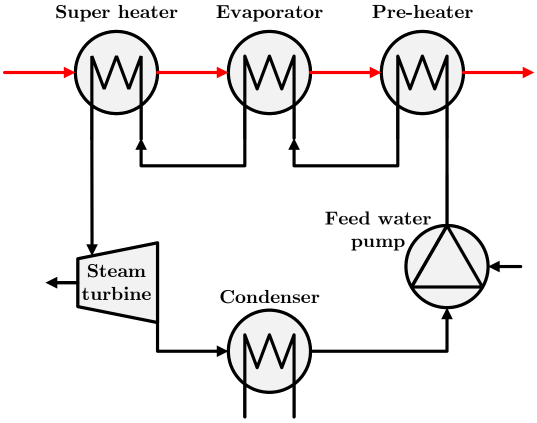

Figure 3.4: A Single Pressure steam rankine cycle.

To investigate the general behaviour of the Singe Pressure cycle including the behaviour of the turbine shaft work W_{shaft}, the heat exchanger areas A_{tot} and the thermal efficiency η_{th}, these are plotted as a function of the cycle pressure.

The shaft work as a function of the cycle pressure can be seen in figure 3.5. It can be observed that the shaft work increases rapidly up to a cycle pressure of approximately 50 bar where after the increase in turbine shaft work diminishes for pressures up to approximately 150 bar. Past this cycle pressure, the shaft work increases rapidly again as the cycle pressure approaches critical conditions of 220 bar. The increase in shaft work, though, comes at the cost of a large increase in the heat exchanger areas. This is illustrated in figure 3.7 which shows the shaft work to heat exchanger area ratio as a function of the cycle pressure. Although pressure losses are neglected in the SRC modelling, the pressure loss will increase as a function of the heat exchanger areas at the air and steam sides. As a consequence, the pressure loss in a real system on the steam side of the heat exchangers will require more pumping work to reach the desired steam pressures leading to a decrease in the overall Rankine system efficiency. The pressure loss on the air side of the heat exchangers will, similarly, have a direct effect on the required pumping work of the charge air fans for the thermal energy storage lowering the overall TES efficiency even further.

The Rankine cycle thermal efficiency can be seen in figure 3.6. It can be observed that the thermal Rankine cycle efficiency increases as a function of the cycle pressure. Past approximately 100 bar, the gains in thermal efficiency diminishes with increasing cycle pressures.

In figure 3.7, the turbine shaft work to the total heat exchanger area can be seen as a function of the cycle pressure. Since the overall TES system efficiency depends on the pumping work to overcome the pressure loss through the steam Rankine cycle boiler on the air side as well as the produced work by the Rankine cycle, this relationship is a convenient way to express the coupled storage and Rankine cycle performance. It becomes clear that an optimum for this relationship exists near a cycle pressure of approximately 40 bar. This will be covered in greater detail in section 5.

The total absorbed heat Q to the total heat exchanger area A can be seen in figure

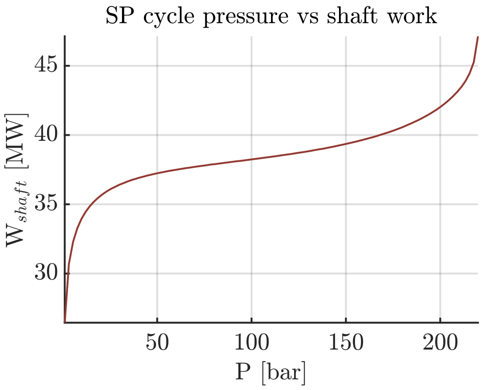

Figure 3.5: The turbine shaft work as a function of the cycle pressure.

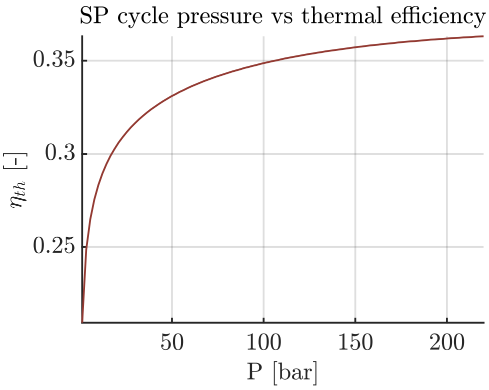

Figure 3.6: The thermal efficiency as a function of the cycle pressure.

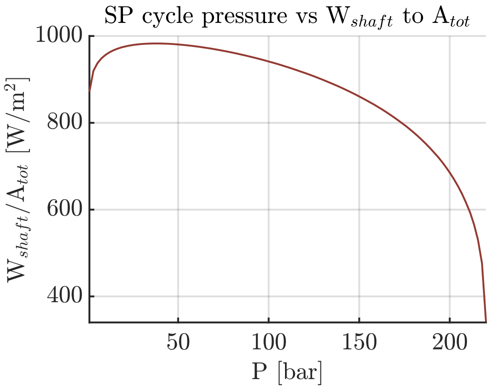

Figure 3.7: The ratio of shaft work to the total heat exchanger area as a function of the cycle pressure.

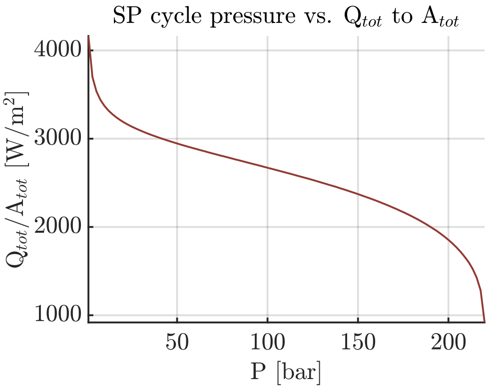

Figure 3.8: The ratio of total absorbed heat to the total heat exchanger area as a function of the cycle pressure.

3.8. When approaching the critical value of the cycle pressure, a sharp decrease in the absorbed heat-to-area ratio can be observed as the heat exchanger area increases.

3.1.3 Dual pressure steam Rankine cycle

The dual pressure steam Rankine cycle is divided into a low pressure (LP) and a high pressure (HP) cycle with a dual stage steam turbine, one for each cycle. The dual pressure steam Rankine cycle is illustrated in figure 3.9.

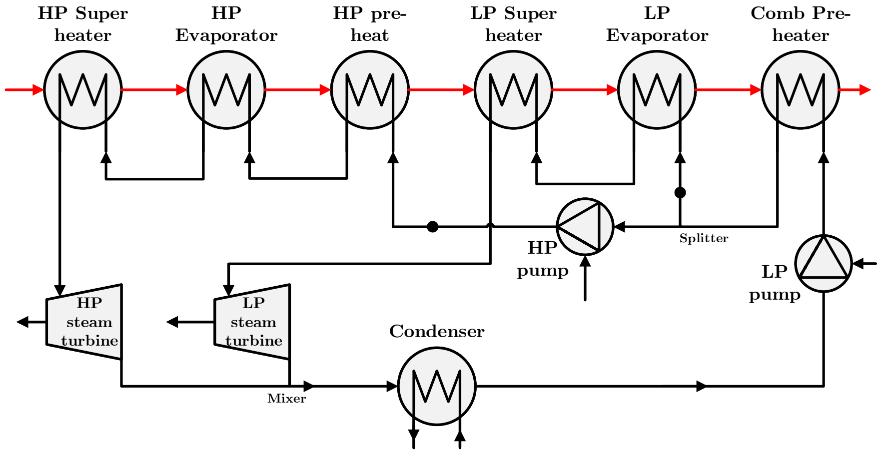

Figure 3.9: Dual pressure Rankine cycle.

The general tendencies are similar to those observed for the single pressure cycle and, thus, plots are not shown for this cycle.

The dual pressure SRC has the potential of a higher power output and higher exergic efficiency than the single pressure cycle due to its ability to utilise heat of a lower temperature and thus lower quality.

The potential advantage of the dual pressure cycle lies in the increase in the average temperature at which heat is being transferred from the air stream compared to the single pressure system by utilising the lower quality heat in the low pressure cycle.

3.1.4 Steam Rankine cycle optimisation

The general goal of a Rankine cycle optimisation is to maximise temperature at which heat is absorbed in the cycle and minimising the temperature at which is rejected from the cycle in the condenser. In this way, the the amount of heat available for useful work will be maximised.

Utilising the in-built optimisation function *min/max* in EES, the optimum cycle pressure in relation to selected parameters can be found. This in-built function uses utilises the Golden section method for one free variable and the Conjugate gradient method for two or more free variables.

The single pressure cycle is optimised using one free parameter, the cycle pressure, while the dual pressure cycle is optimised for two free parameters, the HP and LP cycle pressures.

The parameters for which the cycles are optimised include:

- The thermal efficiency of the Rankine cycle η_{th}.
- The total shaft work W_{tot}.
- The heat exchanger area in relation to shaft work W_{shaft}/A_{tot}.

The General input parameters to the models as well as optimisation constraints are shown below in table 3.1. The discharge air properties are based on values obtained from modelling of the TES in section 4.1 for a discharge rate of 100 MW and 200 MW respectively, which will be covered in separate optimisation cases.

Discharge air properties	Value
Temperature, in	873 K
Temperature, out	373 K and 473 K
Mass flow rate	221.2 kg/s and 442.4 kg/s
General cycle properties	
Condenser water inlet temperature [K]	381
Condenser water outlet temperature[K]	388
Condenser pressure [bar]	0.03
Evaporator and pre-heater pinch temperatures [K]	10
Turbine and pump efficiencies [-]	0.8
General cycle constraints	
Maximum super heating temperature* [K]	813
Maximum steam pressure* [bar]	140
Turbine exit moisture content [-] (Haywood, 1975)	0.85
Additional DP cycle constraints	
LP superheat temperature	2 K above $T_{sat,LP}$
Minimum LP cycle pressure	P_{sat} at T_{out} + 40K (≈ 3.6 bar at $T_{out} = 373$ K) (≈ 33 bar at $T_{out} = 473$ K)
Overall heat transfer coefficients	
Super heater [W/m^2-K]	72
Evaporator [W/m^2-K]	80
Economiser [W/m^2-K]	34
Condenser [W/m^2-K]	3000

Table 3.1: Resulting parameters from the Dual Pressure Rankine cycle optimisation. *Based on Siemens 65 MW ST-400 steam turbine (Siemens AG, 2014).

The results and conclusions obtained from the optimisation can be found in section 5.

3.2 Heat exchanger dimensions

In order to determine the pressure loss across the heat exchanger, the overall dimensions and tube arrangement must be determined. This is done by calculating the amount of tube rows and number of tubes per row based on the heat exchanger casing width.

The boiler tubes used for in this investigation are helically welded serrated fin tubes from

ESCOA (1979) as traditionally used in heat recovery boilers, air heaters etc that can be seen 3.10.

The dimensions of the finned tubes and other variables and constants associated with the finned tubes can be found in appendix F and the tubes are arranged as shown in figure 3.11. By assuming a square casing/channel with a certain width to height ratio and varying transverse pitches, the number of tubes per row are determined. The number of rows in the longitudinal direction needed to reach the desired surface area, determined by the Rankine-cycle model, is then calculated based on dimensions of the channel and the pitches of the boiler tubes.

Figure 3.10: The serrated fin tube used for the heat exchanger.

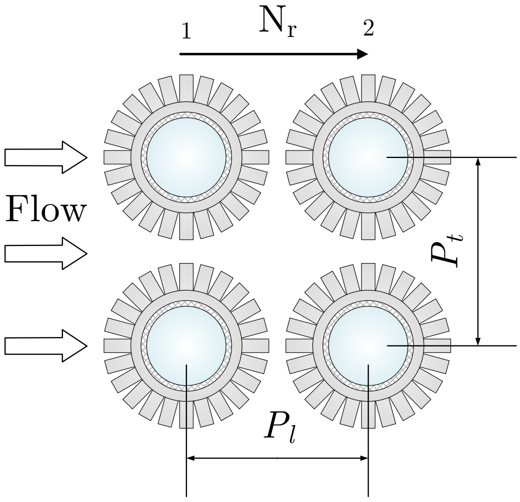

Figure 3.11: Arrangement of the tubes in the heat exchanger (Adapted from ESCOA (1979)).

3.2.1 Efficiency index

In order to choose a optimal heat exchanger layout that accounts for both the pressure loss and the heat transfer, the efficiency index is calculated for a range of channel widths and transverse tube pitches. The efficiency index is a measure of the heat transfer efficiency and the static pressure recovery and is calculated as the ratio of the average Nusselt number to the pressure loss coefficient by (Lu et al., 2013):

$$\textit{Efficiency Index} = \frac{Nu}{K_g} \tag{3.9}$$

where K_g is the pressure loss coefficient and Nu is the average Nusselt number. The average Nusselt number Nu is given by:

$$Nu_{he} = \frac{h_{eff} d_o}{\lambda_{air}} \tag{3.10}$$

where h_{eff} is the effective heat transfer coefficient for the heat exchanger [W/m^2-K] which is based on empirical relations described in appendix F.1.1 (ESCOA, 1979). d_o is the tube outer diameter [m] and λ_{air} is the thermal conductivity on the air side of the tubes [W/m-K]. The pressure loss coefficient K_g is given by:

$$K_g = \frac{\Delta p}{1/2 \rho_{air} v_{air}^2} \tag{3.11}$$

where the numerator Δp describes the static pressure difference across the heat exchanger, which based on empirical relations as described in F.1.2. The denominator describes the dynamic pressure based on ρ_{air}, the air density outside the tubes and v_{air}, the air mean velocity in the flow channel.

The results of the heat exchanger parametric study are presented in section 5.1.

4. TES Parametric study

In this chapter, the behaviour of the TES will be examined by conducting a parametric study. The developed TES model will be subjected to different operating conditions by varying selected parameters. By doing this, the governing parameters for the overall TES efficiency can be identified based on characteristics such as pressure- and thermal losses of the TES. In this parametric study, only the TES parameters are treated. This means that the auxiliary system is not taken into account other than the pump power needed to charge and discharge the TES. A parametric study of the auxiliary system is presented in a later section. The overall pressure loss of the TES does not include the Rankine cycle heat exchanger pressure loss, as this will be examined in a later section.

The TES parametric study will include an investigation on the following parameters:

- **Storage shape:** Existing thermal energy storages like the pilot plant in Ait Baha are conically shaped. The model is used to compare the conical shape of the already existing TES to a simpler cylindrical shape to investigate the difference in the TES characteristics.
- **Rock diameter:** The diameter of the rocks affects the shape of the heat front and the pressure loss though the TES.
- **Charge-discharge rate:** The air flow rate through the TES determines how fast the TES can be charged or discharged but also affects the pressure loss through the TES.
- **Insulation thickness:** A larger thickness of the insulation material reduces the thermal losses but increases the cost of a thermal energy storage. Large scale storages will benefit from a high volume to surface ratio which might diminish the benefits of large amounts of insulation.
- **TES dimensions:** Stiesdal (2016b) suggests a long, horizontal TES that will increase the available capacity of the TES compared to shorter, vertical storages with the same volume. This will, however, have a negative effect on the TES pressure loss and, thus, the overall efficiency.

The dimensions of the 175,000 m^3 TES used in the parametric study can be seen in figure 4.1 and it illustrates the 25 m high TES with a diameter of almors 100 m.

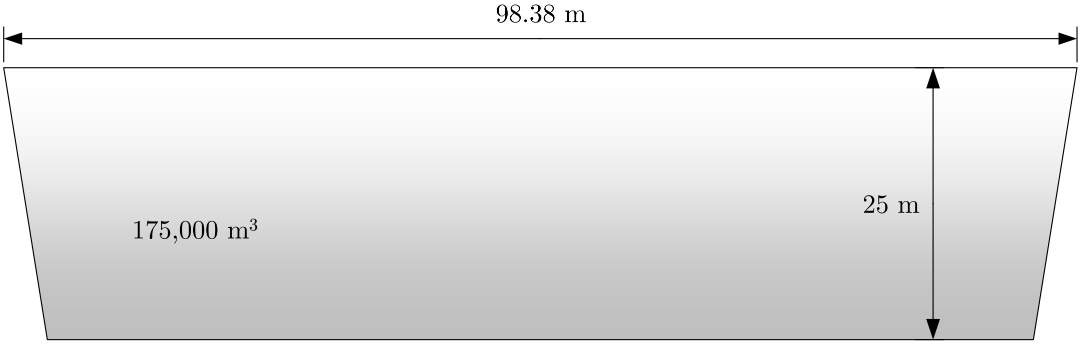

Figure 4.1: Illustration of the dimensions of a TES with a volume of 175,000 m^3.

4.1 Conical and cylindrical TES

The existing TES in Ait Baha, Morocco, and Biasca, Switzerland, are both conical in shape due to the benefit of higher structural support allowing for thermal expansion of the storage material. Besides this benefit, the conical shape have a positive effect on many other of the TES parameters. As the heat is stored in the upper part of the TES, the conical TES will have a larger volume to surface ratio in the hotter regions of the TES which reduces the the thermal losses to the surroundings.

Another benefit of the conical structure is the inherent compensation for the higher air velocities in the hot upper region of the TES with the larger cross sectional area in this region. This effectively reduces the pressure loss in this part of the TES. In the lower part of the conical TES the cross-sectional area is smaller compared to a cylindrical TES while the temperature is correspondingly lower in this region. This results in a lower air velocity than in the upper parts of the TES. The effects of the conical shape versus a simple cylindrical shape on the heat distribution, pressure loss and heat loss are examined in this section.

The detailed parameters used in the model for the study of the conical and cylindrical TES are shown in table 4.1.

Geometric parameters		
Volume [m^3]	175,000	
Shape	Cone	Cylinder
Top radius [m]	49.19	47.2
Bottom radius [m]	45.19	47.2
Height [m]	25	
Charge parameters		
$\dot{m}_{air}$ [kg/s]	221.2	
Charge temperature [K]	873	
Thermal charge rate [MW_{th}]	100	
Charge time [days]	7.48	
Discharge parameters		
$\dot{m}_{air}$ [kg/s]	221.2	
Discharge temperature [K]	473	
Thermal discharge rate [MW_{th}]	100	
Discharge time [days]	7.48	

Table 4.1: Parameters for the four different TES configurations used to compare a conical TES to a cylindrical TES.

The model is simulated from an initial state with the TES discharged to 25% capacity. This state is shown in figure 4.2 for both the conical and the cylindrical TES. From the figure it can be seen that the heat front in the conical TES is steeper than the heat front in the cylindrical TES. This small difference occurs because more energy is stored in the upper part of the conical TES volume compared to the cylindrical TES wherein the energy is distributed further down in the TES.

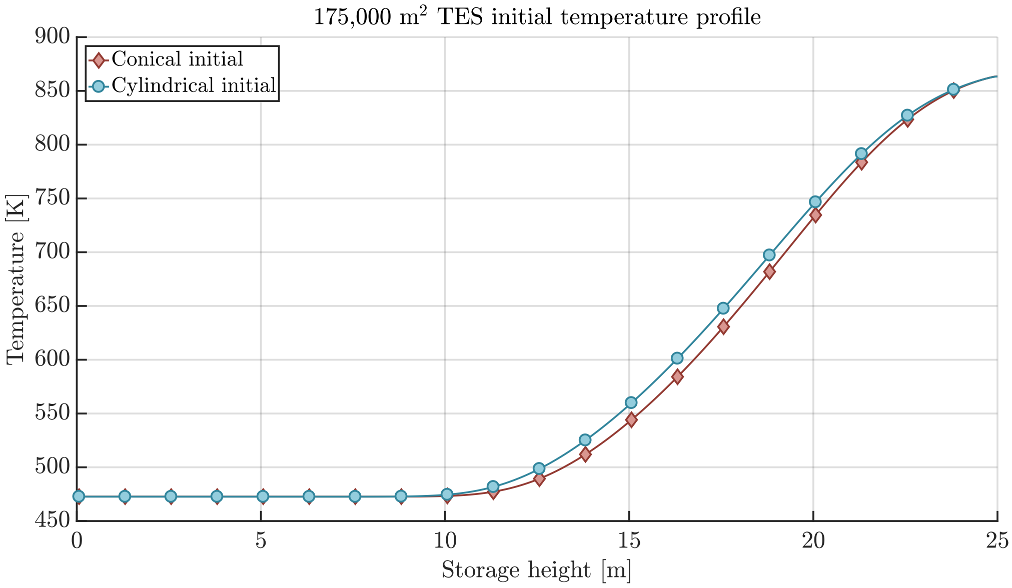

Figure 4.2: Initial capacity of 25% for the conical TES (red line) and the cylindrical TES (blue line) that is used as basis for all simulations in the parametric study.

Form the initial state the charge phase will be simulated followed by the discharge phase. The charge and discharge parameters in table 4.1 correspond to 50% of the TES capacity being added through charge or removed through discharge *i.e.* the TES will be charged from 25% capacity to 75% capacity and discharged back to 25% capacity during a full charge/discharge cycle. When the cycle is complete, the cycle efficiencies and loss fractions can then be determined. Before this can be performed, though, the temperature profiles and losses during simulation will be examined in greater detail.

Conical and cylindrical TES temperature- and energy distribution

Figure 4.3 shows both the temperature profile after the charge phase and after the discharge phase. The difference between the conical and the cylindrical TES is not significant. The heat fronts after the charge phase are almost identical although the cylindrical heat front reaches deeper into the TES as the cylindrical shape cannot store the same amount of energy in the upper part of the TES.

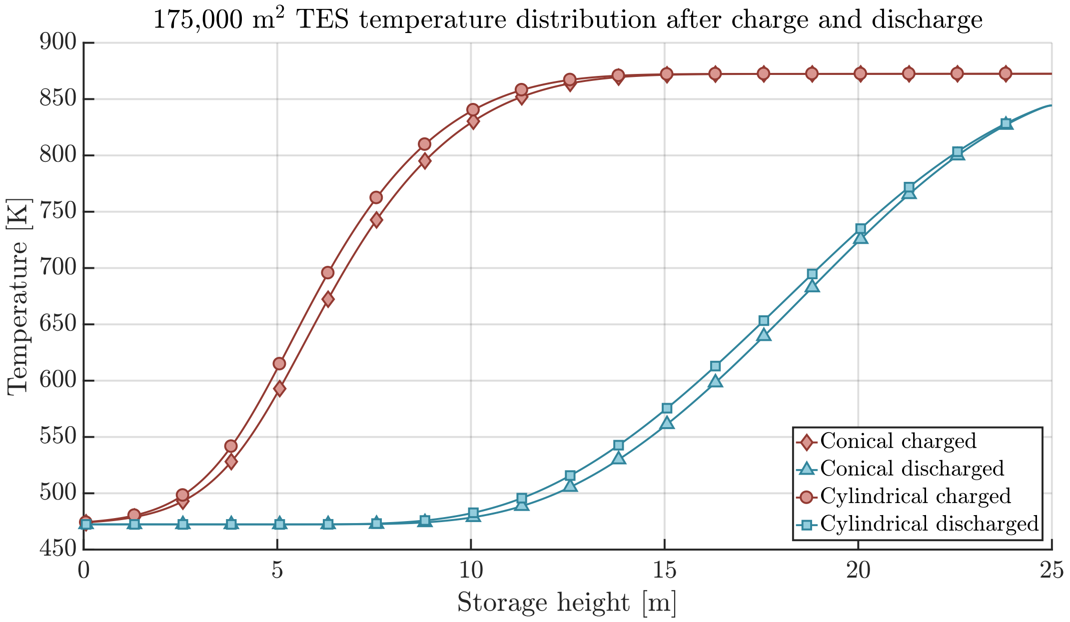

Figure 4.3: Heat front of the conical and cylindrical TES after the charge and discharge periods.

The heat fronts after the discharge phases are similar to the heat fronts of the initial state although the temperature of both are now lower at the top than at the initial state as shown in figure 4.2. This happens as conduction and radiation transports the thermal energy downwards (axially) during the charge/discharge cycle, effectively lowering the temperature in the hotter parts of the TES.

Figure 4.4 shows how the energy in the TES is distributed per meter down through the TES. From this is can be observed how the conical TES stores more energy in the upper parts compared to the cylindrical TES.

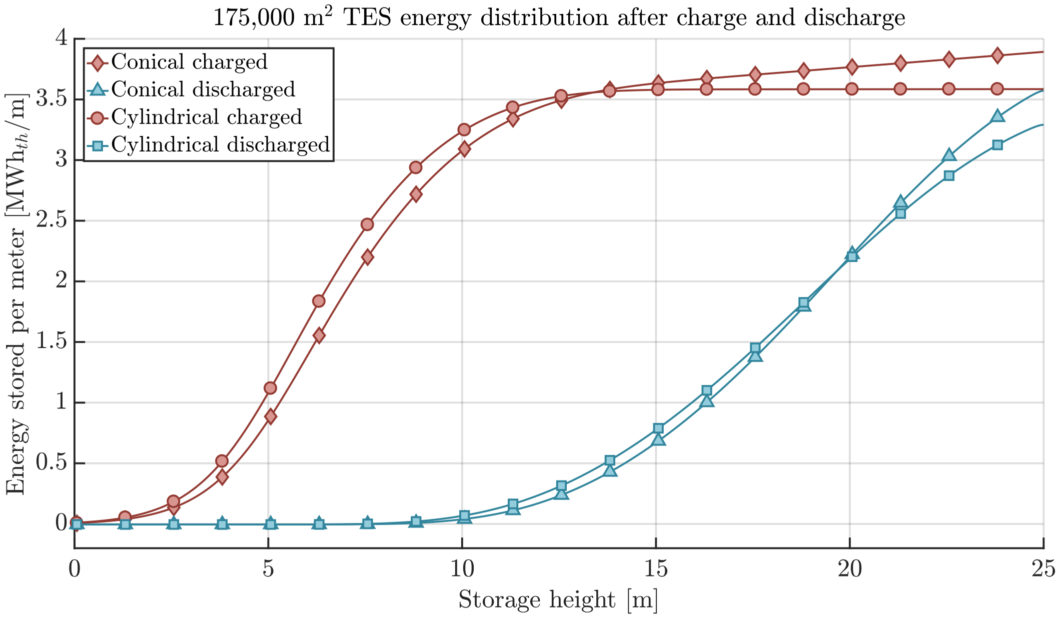

Figure 4.4: Distribution of thermal energy in the conical and cylindrical TES after the charge and discharge periods.

This difference in the energy distribution between the two shapes is the main reason that the thermal losses are lower for the conical TES compared to the cylindrical TES.

Thermal losses

The rate of heat loss through the floor, walls and roof of the conical and cylindrical TES are shown in figure 4.5 for the complete charge-discharge cycle. The loss increases as the overall temperature of the storage increases during the charge period and decreases again during the discharge period causing the spike in the curves in figure 4.5. As the temperature at the floor and roof remains almost constant during the charge-discharge cycle, the change in the loss across the cycle is due to the wall loss.

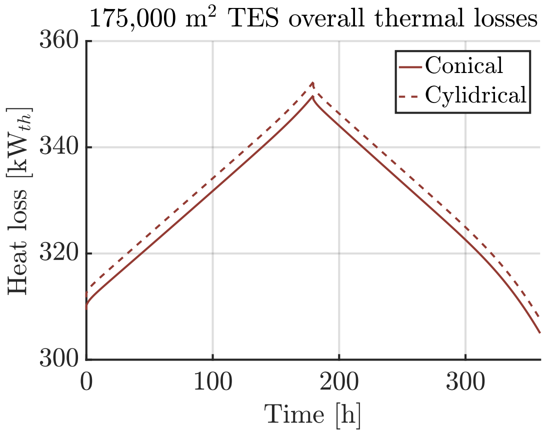

Figure 4.5: Thermal loss rate over the entire charge-discharge cycle.

The thermal losses through the floor, walls and the roof for the conical TES can be seen in figure 4.6. The floor and roof can be seen to have similar thermal losses, caused by the floor being less insulated but kept at a lower temperature with the roof being better insulated but having a higher temperature. The drop in the roof thermal losses are attributed to the drop in the roof temperature at the end of the discharge cycle as described above. The small increase in the thermal floor losses is due to a small temperature increase at floor in the end of the charge phase as the capacity increases towards 75%.

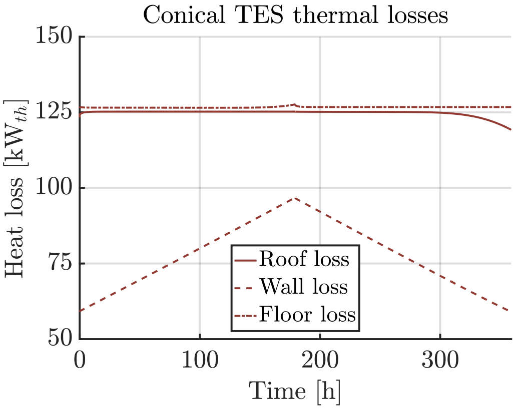

Figure 4.6: Thermal losses through floor, roof and wall of the conical TES.

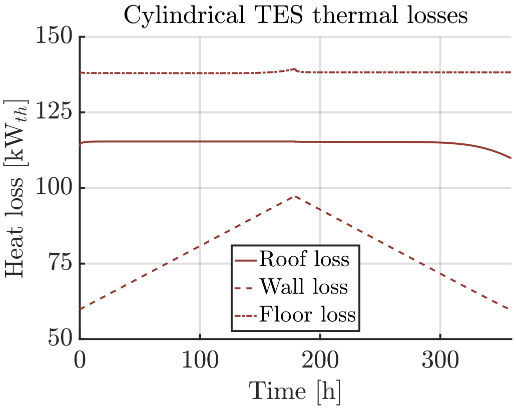

Figure 4.7: Thermal losses through floor, roof and wall of the cylindrical TES.

The floor losses of the cylindrical TES are greater compared to the roof losses because the surface of the roof and the floor are identical in the cylindrical TES, and even though the temperature at the floor is much lower than at the roof, the smaller amount of insulation of the floor results in a higher overall heat loss.

Pressure losses

The total pressure loss through the TES is also affected by the shape as the velocity decreases due to the greater cross-sectional area in the top region of the conical TES. Here, a high temperature means that the velocity of the air flow increases due to low air density. Likewise, the velocity in the lower part of the conical TES increases compared to the cylindrical TES due to a smaller cross sectional area. However, the air flow velocity in this region is also lower due to a lower temperature and higher air density. The pressure loss for the conical and cylindrical TES are compared in figure 4.8. The conical TES can be seen to have a lower pressure loss compared to the cylindrical TES.

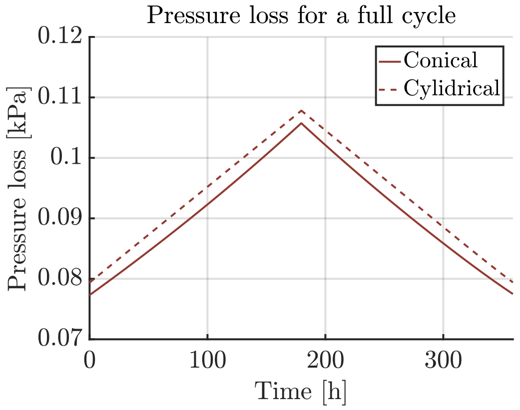

Figure 4.8: Pressure loss through the conical and cylindrical TES over the entire charge-discharge cycle.

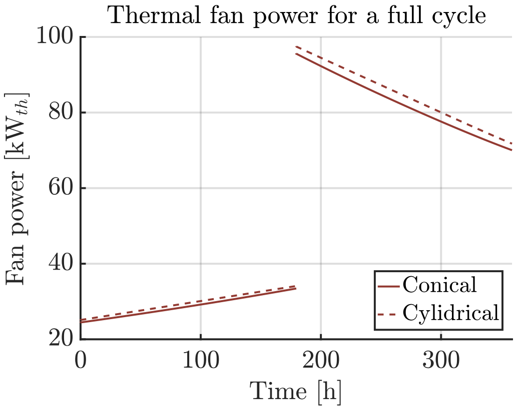

Figure 4.9: Required thermal power needed to drive the fan across the entire charge-discharge cycle.

Figure 4.9 shows the power used by the fan during the charge-discharge cycle. During charge, the fan is powered by electricity from the grid and is accounted for in the same manner as the heat input to the TES during the charge period. This means that the electricity is converted to heat at 100% efficiency. The cost of running the fan during charging is, however, subject to a fan efficiency of 95%.

During discharge, the fan is driven by the on-site Rankine-cycle assumed to have an efficiency of 35%. This means that the amount of stored heat needed to drive the fan is not only subject to the assumed 95% fan efficiency but also the assumed 35% Rankine cycle efficiency *i.e.* the thermal power needed to drive the fan during discharge is much higher than for the charge cycle. Compared to the thermal losses, the fan loss for the charge cycle is therefore much smaller, at around 20-30 kW, compared to the thermal losses in the range of approximately 310 to 350 kW. For the discharge phase, the fan losses are, however, in the range of approximately 70 to 95 kW; a substantial increase and about one third of the thermal losses.

Conclusion

Overall, the differences between a conical and a cylindrical TES of this scale are rather small. The conical TES does perform slightly better, as expected, having lower overall thermal losses and a lower pressure loss, which subsequently requires less fan power. The differences are, however, small: as it can be seen from table 4.2, the differences in the loss fractions are negligible. Furthermore, the loss fractions are very low meaning that the losses compared to the amount of energy recovered from the TES are below 1% for both the conical and the cylindrical TES. This can also be seen from the efficiencies, where the differences are also considered negligible.

	Cone	Cylinder
Loss fraction		
$f_{thermal}$ [%]	0.70	0.71
f_{fan} [%]	0.12	0.12
Efficiencies		
η_{cycle} [%]	98.52	98.54
ψ_{cycle} [%]	98.30	97.34

Table 4.2: Overall loss fractions and efficiencies for the conical and cylindrical TES

From this analysis it can be concluded that the TES will not benefit noticeably from the cylindrical shape compared to a conical shape as the losses are simply to small to affect the final performance and efficiencies. From a structural standpoint, the TES should still be constructed as a conical TES. All further analysis of the TES in this report will still utilise the conical TES.

4.2 Rock diameter

In this section, the effect of using rocks with different diameters as storage material in the TES will be investigated. The rock diameter has an effect on the volumetric heat transfer coefficient which causes the heat transfer to become less effective for larger rock diameters. This, in turn, means that the air must travel further through the TES before it is cooled or heated to the rock temperature, thus, lengthening the heat front. Additionally, the rock size also has an effect on the pressure loss through the TES, with smaller diameter rock yielding higher heat transfer performance but also higher pressure loss.

For this study, the conical 175,000 m^2 TES performance will be evaluated for rock diameters from 1 to 9 cm in five intervals. Again, a full charge-discharge cycle will be used, this time at 100 MW_{th} rate for both the charge- and discharge cycle. The duration of the charge- and discharge cycle is maintained so that, in total, 50% of the total TES capacity is charged and discharged as described in section 4.1. As in the earlier studies, the initial condition for the TES is a 25% starting capacity with the temperature profile shown in figure 4.2. The detailed model parameters can be seen in table 4.3:

Variable parameter			
Rock diameter [cm]		[1 3 5 7 9]	
Charge parameters		**Discharge parameters**	
$\dot{m}_{air}$ [kg/s]	221.2	$\dot{m}_{air}$ [kg/s]	221.2
Charge temperature [K]	873	Discharge temperature [K]	473
Charge rate [MW_{th}]	100	Discharge rate [MW_{th}]	100
Charge time [days]	7.48	Discharge time [days]	7.48

Table 4.3: Rock diameters and cycle parameters used in the study of the rock diameter and its effect on TES performance.

Temperature distribution

Figure 4.10 shows the heat front of the TES after a single charge period. The graph shows that the smaller rock diameter of 1 cm causes the length of the heat front to decrease by some degree compared to the larger diameters. The effect of this is, however, not very significant although it could possibly provide a longer discharge period before the outlet temperature of the TES is affected.

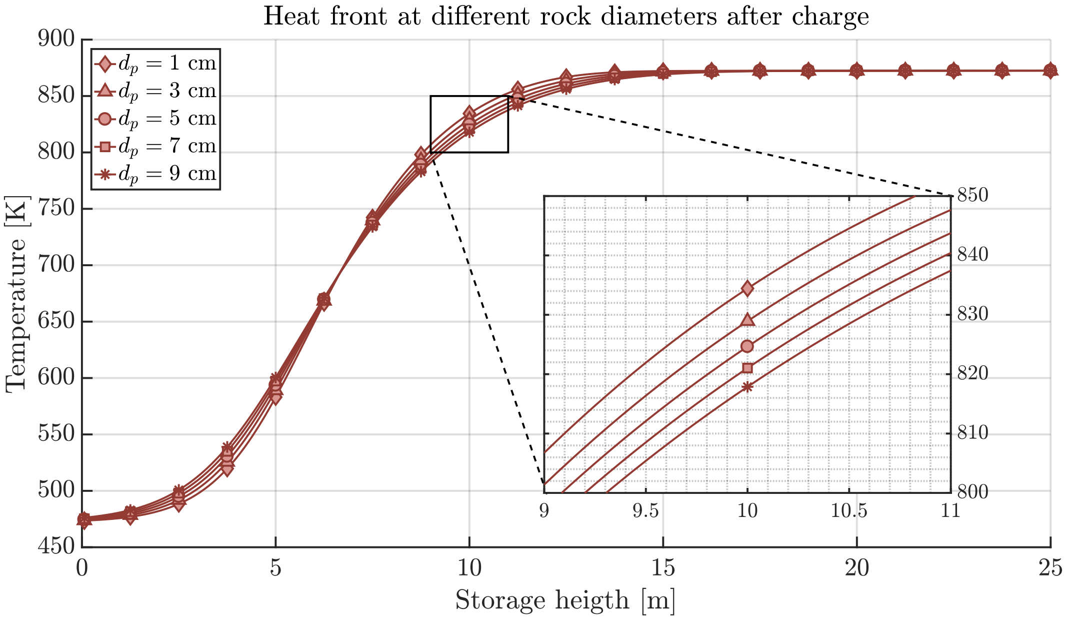

Figure 4.10: Heat front after the charge period for different rock diameters.

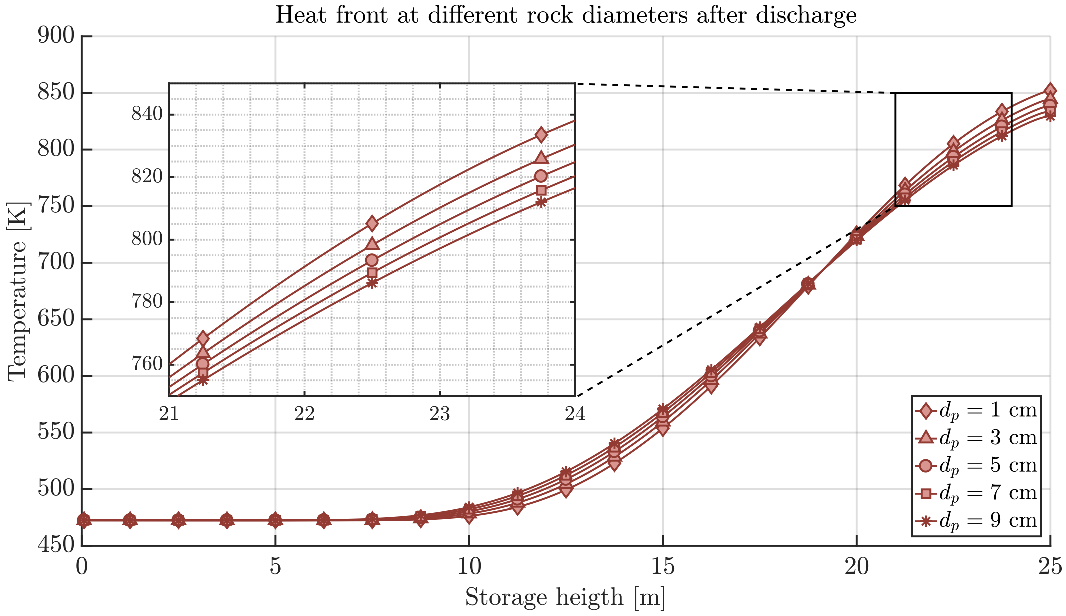

Figure 4.11: Heat front after the discharge phase for different rock diameters.

The heat front at the end of the discharge period is shown in figure 4.11. The outlet temperature of the TES can be seen to vary depending on the rock diameter. It can be observed that the temperature drops off earlier for larger rock diameters. This will affect the length of the period in which the TES can be operated without experiencing a drop in the discharge temperature *i.e.* for low storage capacities.

Figure 4.12 shows the outlet temperature at the roof at the end of the discharge period for the different rock diameters. From this is can be seen that a rock diameter of 9 cm causes the TES discharge temperature to drop below 870 K after approximately 100 hours of discharge while rocks with a diameter of 1 cm reaches 870 K after 140 hours, 40 hours later. The smaller rocks do, however, introduce a higher pressure loss across the TES. This means that the size of the rocks cannot be reduced very much without it having a significant negative effect on the fan power required to pump air through the TES.

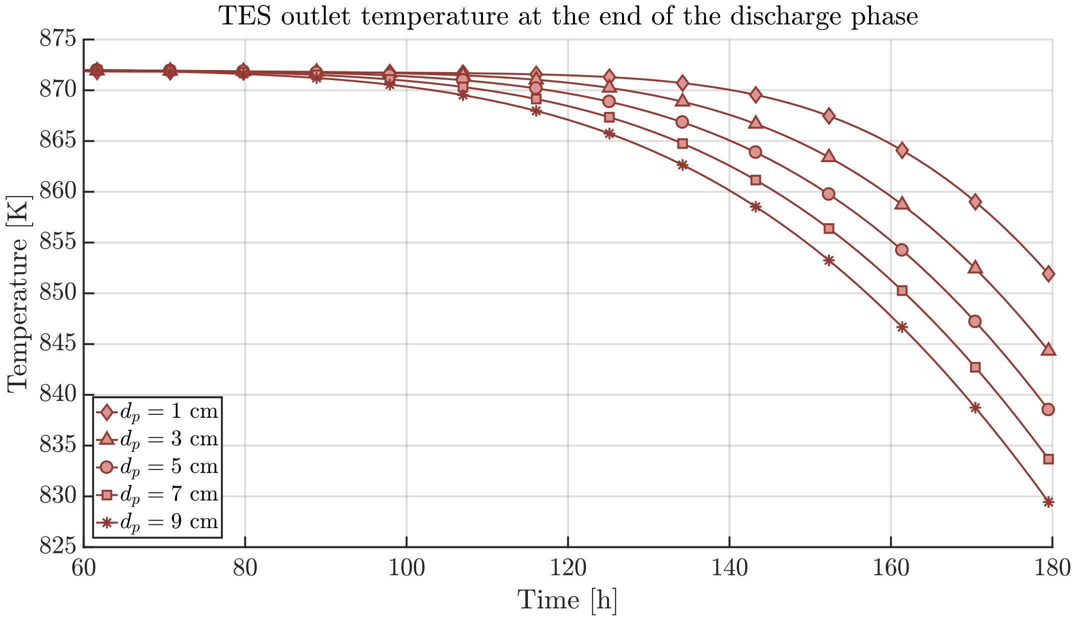

Figure 4.12: Outlet temperature at the roof of the TES at the end of the full charge-discharge cycle.

Figure 4.13 shows the fan power required to pump air at different rock diameters along with the pressure drop as a function of the rock diameter over a charge-discharge cycle. As the figure shows, the pressure loss does not increase linearly: at a rock diameter of 1 cm, the required fan power is almost 4 times higher than for a rock diameter of 3 cm. The difference between a rock diameter of 3 and 5 cm is not as significant. Nonetheless, twice as much power is required to circulate the air through the TES when moving from a rock diameter of 5 cm to 3 cm. At larger rock diameters, the difference in pressure loss becomes even smaller.

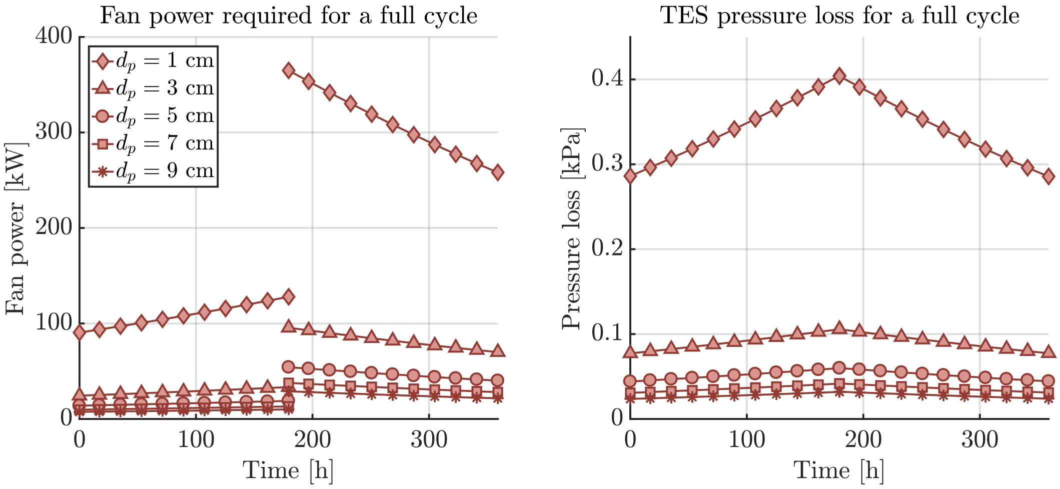

Figure 4.13: Fan power and pressure loss over the entire charge-discharge cycle for different rock diameters.

The increase in rock diameter also increases the Biot number as the distance from the surface to the center of the rocks increases while the conductivity remains constant. This affects the ability of the rocks to absorb and deliver heat from and to the air during the charge and discharge phase respectively. The model does not take this delay into account. An excessively high Biot number would, though, make the heat front even longer which is undesirable. Therefore, Biot numbers much higher than 0.1 will cause the accuracy of model results to decrease and compromise the model validity.

Figure 4.14 shows the maximum Biot number observed during simulation as a function of rock diameter. It can be seen that rock diameters above 5 cm should be avoided at the present charge-discharge rate of 100 MW. Lowering the charge-discharge rates lowers the air velocity and would not only decrease the Biot number but also the pressure loss and thus enabling the use of a smaller rock diameter.

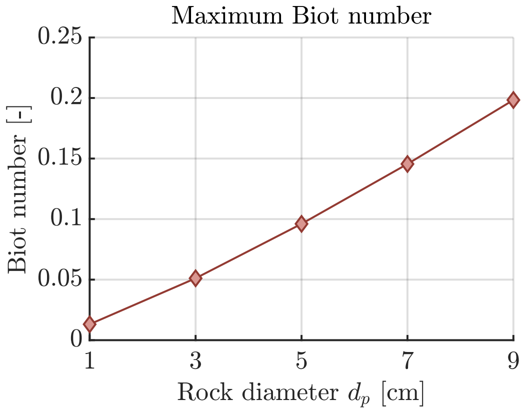

Figure 4.14: Maximum Biot number observed during the full charge-discharge cycle at the different rock diameters.

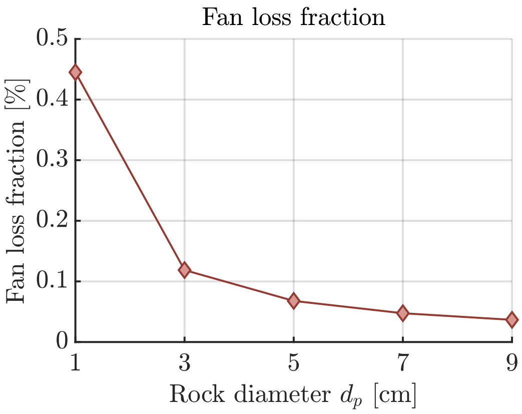

Figure 4.15: Fan loss fraction during the full charge-discharge cycle at the different rock diameters.

Rock diameter conclusion

Overall, based on the Biot number, it can be concluded that the maximum rock diameter at a 100 MW charge-discharge rate should not exceed 5 cm. A rock diameter of 1 cm would allow the TES to be discharged at a lower capacity without lowering the outlet temperature but would also cause a significantly higher pressure loss compared to a rock diameter of 3 cm. Based on this, a rock diameter of 3 cm is chosen as this would also allow for greater charge-discharge rate without increasing the Biot number. Furthermore, the efficiencies achieved for the different simulations at the 5 rock diameters can be seen in table 4.4: From this it can be seen that the efficiency is only affected to a small degree the change in the rock diameter. The main cause for the change in efficiencies is the outlet temperature that effectively reduces the amount of energy recovered at the end of the discharge-period. The exergy efficiency suffers the largest penalty as a function of the drop in temperature as the energy quality of the recovered air is reduced by the lower temperature. This however only occurs during the later parts of the discharge period and the effect on the exergy efficiency is still minimal.

Rock diameter [cm]	1	3	5	7	9
η_{cycle} [%]	98.54	98.52	98.25	97.97	97.69
ψ_{cycle} [%]	98.20	98.27	97.96	97.62	97.29

Table 4.4: Energy and exergy efficiencies for the TES for 5 different rock diameters.

4.3 Charge-Discharge rate

In this section the charge-discharge rate is investigated in order to determine the increase in pressure loss as the air flow rate is increased. The TES will be charged from an initial capacity of 25% up to 75% and again discharged to 25% as the previous study. This means that, at faster charge rates, the pressure loss may be higher although the duration of the charge-discharge cycle will also be shorter thus decreasing the thermal losses. The charge-discharge rate is varied from 100 MW$_{th}$ to 500 MW$_{th}$ which corresponds to air mass flow rates of 221.2 kg/s to 1106 kg/s and core mass flow rates of 0.034 kg/s-m^2 to 0.17 kg/s-m^2 which corresponds to the limit specified in the grid independence study.

The charge-discharge parameters can be seen in table 4.5. These are scaled so that the amount of energy added through charge period and removed during the discharge period is maintained at 50% of the TES capacity. For this study the rock diameter is kept at 3 cm as determined in the previous study while the charge- and discharge inlet temperatures remain at 873 K and 473 respectively.

Charge-discharge rate [MW$_{\mathbf{th}}$]	100	200	300	400	500
$\dot{m}_{air}$ [kg/s]	221.2	442.4	663.5	884.7	1106
Charge time [days]	7.48	5.61	3.74	2.81	1.50

Table 4.5: Parameters used in the study of the charge-discharge rate.

The fan loss fraction as a function of varying charge-discharge rates can be seen in figure 4.16. It can be observed that the fan loss fraction steadily increases as the air flow rate is increased up to a total loss fraction of 3% at 500 MW$_{th}$. Figure 4.17 shows that the combined thermal loss through the TES surfaces during the charge-discharge cycle is dictated by the time it takes to charge and discharge the TES, but is not otherwise affected by the charge-discharge rate.

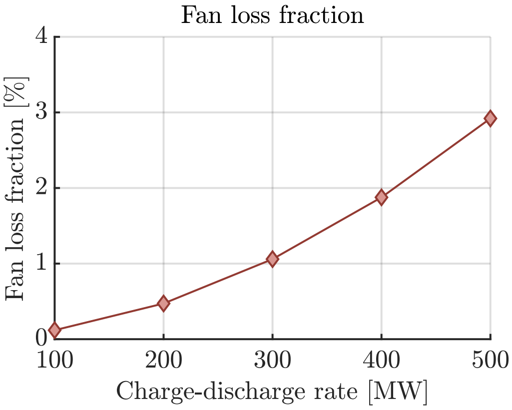

Figure 4.16: Fan loss fraction at increasing charge-discharge rates.

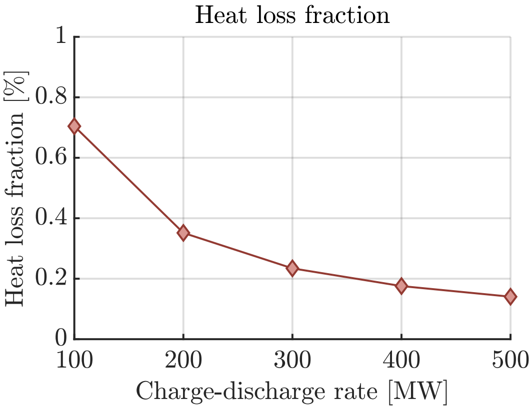

Figure 4.17: Thermal loss fraction at increasing charge-discharge rates.

Figure 4.18 shows how the Biot number is affected by the increasing charge-discharge rate. From this is can be seen that about 250 MW$_{th}$ would be the maximum allowable rate as higher flows would imply that the rocks could not transfer the heat as fast as the fluid-solid convection would be able to remove it.

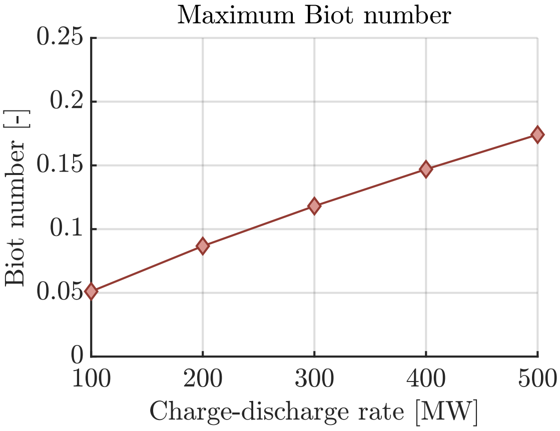

Figure 4.18: Maximum Biot number observed during the full cycle as a function of the charge-discharge rates.

Based on the observations above, it is concluded that the charge-discharge rate should be kept below 250 MW$_{th}$ for a TES of this size. The efficiencies for this analysis are shown in table 4.6:

Charge-discharge rate [MW$_{\mathbf{th}}$]	100	200	300	400	500
η_{cycle} [%]	98.52	98.54	98.07	97.31	96.31
ψ_{cycle} [%]	98.27	98.14	97.36	96.16	94.62

Table 4.6: Efficiencies of the TES at different charge-discharge rates.

4.4 Insulation thickness

In this study, the amount of insulation material is varied in order to determine how the amount of insulation in the TES roof, wall and floor affects the overall heat loss during a complete charge-discharge cycle. The cycle is defined similarly to the previous studies for 100 MW$_{th}$ charge-discharge rate. The insulation thickness is varied using the initial thickness of insulation of the two main insulation materials as the maximum value as shown in table 4.7. The insulation thickness is then decreased during simulation by multiplying the thickness by a factor less with a value less than one. The simulation is repeated 5 times for factors of f_{ins} = [0.1 0.25 0.4 0.6 0.8]. The simulation results are compared to each other and to the default insulations thickness.

	Insulation thickness [m]	
	Microtherm®	Foamglass®
Roof	0.6	0.5
Wall	0.6	0.5
Floor	0.0	0.4

Table 4.7: Initial insulation thickness for the TES roof, walls and floor.

Figure 4.19 shows the combined thermal losses through the floor, wall and roof of the TES. It can be observed that the effect of reducing the insulation thickness increases the thermal losses. As the thickness approaches the initial value, however, diminishing returns are shown at $f_{ins} = 0.6$ to $f_{ins} = 0.8$ compared to the effect of an increase from $f_{ins} = 0.4$ to $f_{ins} = 0.6$.

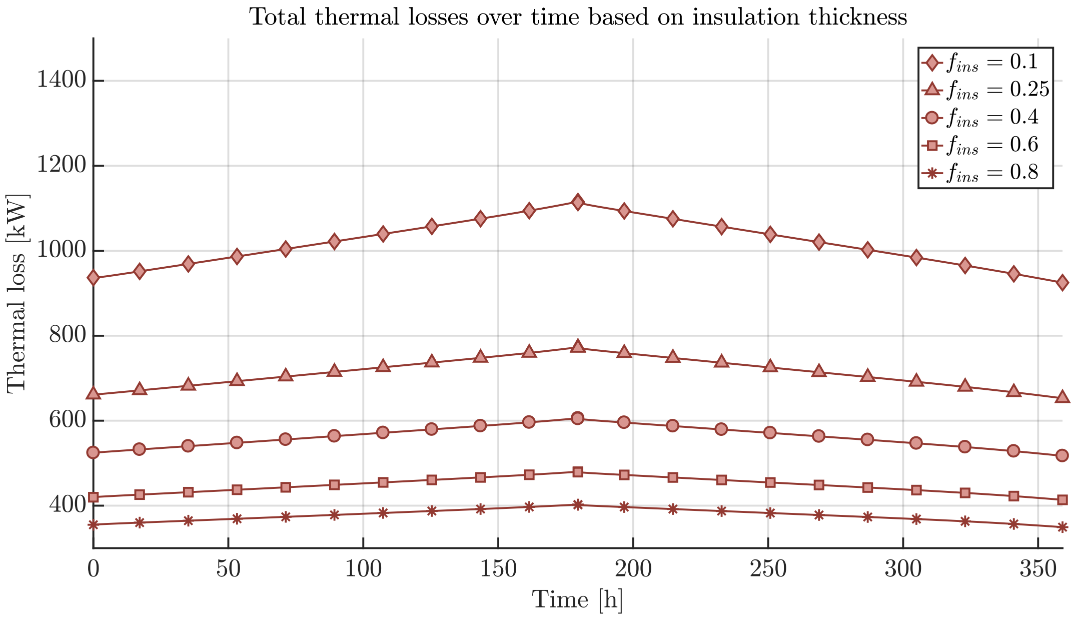

Figure 4.19: Magnitude of thermal losses at the varied insulation thickness.

Figure 4.20 shows the outlet temperature at the end of the discharge phase. It can be observed that the outlet temperature is not affected significantly by the decrease from 80% of the initial insulation thickness to 60%. It can be concluded that increasing the insulation thickness above 60% of the original thickness does not significantly increase the discharge temperature.

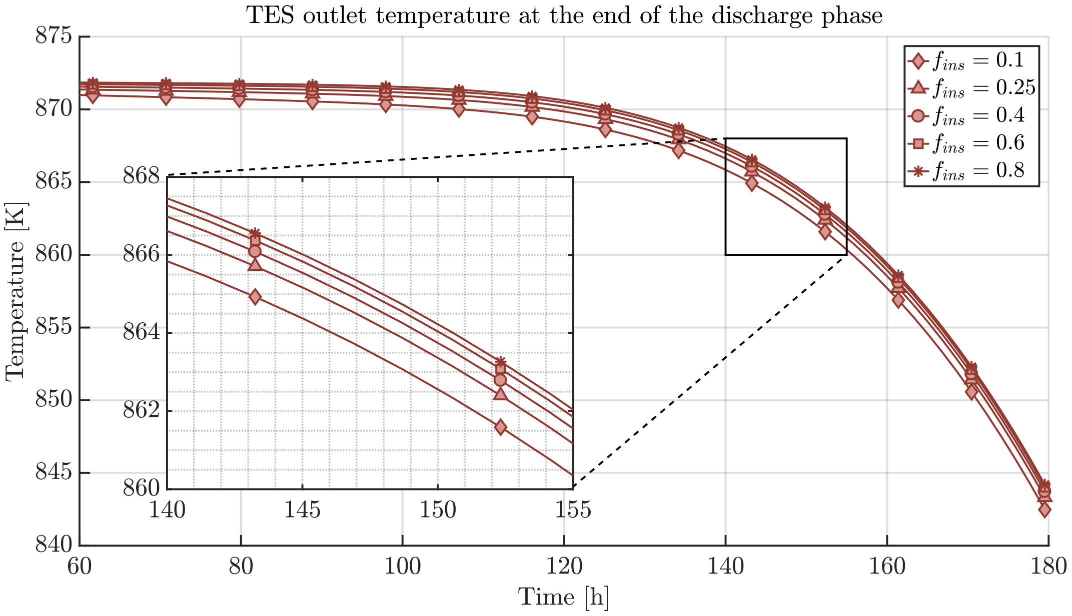

Figure 4.20: The TES outlet temperature at the end of the discharge phase illustrating the temperature drop caused by the amount of insulation.

Figures 4.21 and 4.22 shows the accumulated thermal losses during the charge-discharge cycle and the corresponding loss fractions. These include the values for the initial insulation tickness represented by $f_{ins} = 1$. Again, larger insulation thicknesses do not reduce the fraction of thermal energy lost to the surroundings by a significant amount. It should be noted that the losses through the roof account for the highest fraction of the total losses. From a practical point of view, this would also be the easiest place to additional insulation, should it be required.

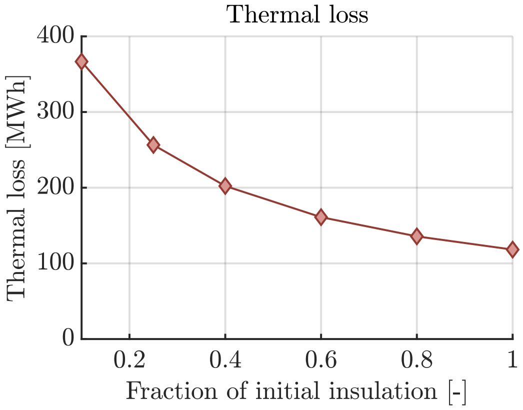

Figure 4.21: Total amount of energy lost to the surroundings over the charge-discharge cycle.

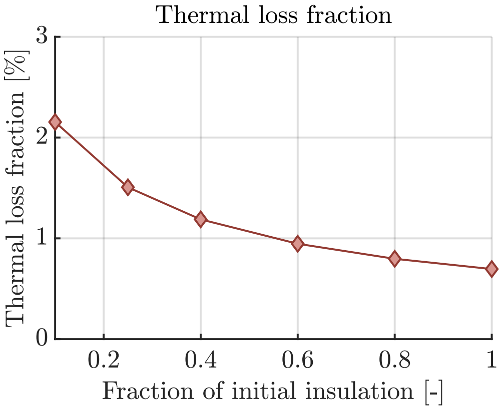

Figure 4.22: Fraction of heat lost to the surroundings in relation to the total amount of energy added to the TES.

Table 4.8 shows the efficiencies at the varying insulation thicknesses. It can be seen that the difference in efficiencies between 10% and 100% of the initial insulation thicknesses is 0.73% percent points for the energy efficiency and 0.66% for the exergy efficiency. With this in mind it and taking the thermal loss fraction into account it would be feasible to reduce the amount of insulation by 20 to 40% without significant impact on the TES performance and keeping the thermal loss fraction below 1%.

Insulation thickness factor f_{ins} [-]	0.1	0.25	0.4	0.6	0.8	1
η_{cycle} [%]	97.79	98.10	98.26	98.38	98.46	98.52
ψ_{cycle} [%]	97.61	97.89	98.03	98.84	98.22	98.27

Table 4.8: Efficiencies of the TES for varying insulation factors.

4.5 TES diameter to length ratio

Author Stiesdal (2016b) suggests that a long narrow TES geometry that would have the beneficial characteristic of a steep heat front in relation to the TES length, allowing for longer discharge periods at a constant temperatures avoiding the drop off in temperature as observed in figure 4.12 for rock diameter.

The developed model is, however, not suited for this kind of analysis since the grid independence study shown in section 2.3.1 concluded that a grid layer height of 6.25 cm was required to properly determine the length of the heat front. When using the model to study a longer TES, the model will over-estimate the length of the heat front. The important parameter for this study is, however, the pressure loss and besides the temperature in the TES affecting the air velocity differently than expected the pressure loss can still be evaluated to some degree.

Because the temperature throughout the storage is not constant, the velocity of the charge air will equally vary depending on the temperature. The increased velocity will again affect the pressure loss throughout the storage and thus, for longer storages, the effect of this will become more prominent. Despite this, the pressure loss can still be evaluated to some degree using the current model.

Stiesdal (2016b) proposes a 250 m long storage that have the input and output in the same end of the TES installation. This leads to a horseshoe design similar to that shown in figure 1.11 with a minimum TES length of 500 m. The model has been run at five intervals gradually increasing the length of the TES from 25 m to 500 m while keeping the volume constant at 175,000 m^3 and the performance will be evaluated based on the maximum observed Biot number and the fan loss fraction.

The Biot number is shown in figure 4.23 and it can be seen that the increased velocity in the TES causes the Biot number to increase beyond 0.1 at a length just above 50 m. The pressure loss is, however, greatly affected as the length and the velocity of the air increases.

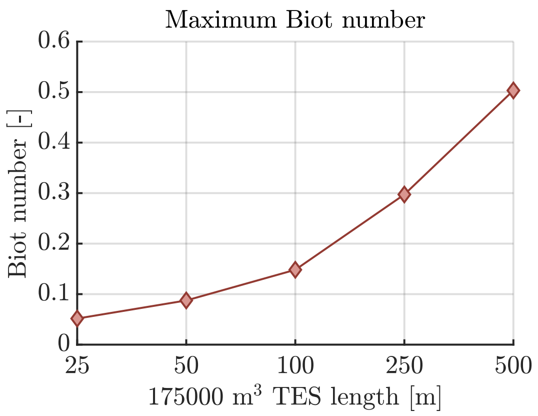

Figure 4.23: Maximum observed Biot number during the full charge-discharge cycle simulation.

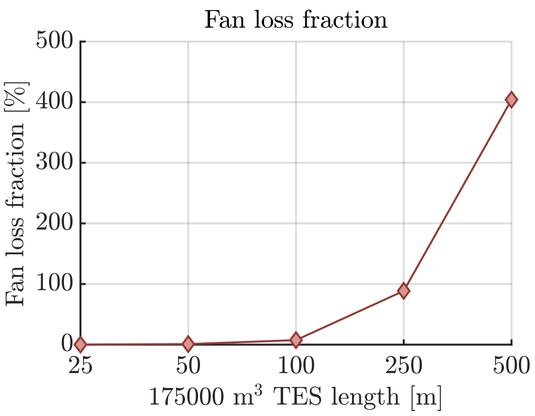

Figure 4.24: Fan loss fraction over the full charge-discharge cycle simulation.

This results in a significant increase in the fan losses as seen in figure 4.24. The fraction of equivalent thermal energy required to drive the fan exceeds the actual energy recovered from the TES by a factor of 4 at a length of 500 m. Stiesdal (2016b) proposes a segmentation of the TES in to smaller insulated sections that can be discharged individually in order to circumvent the high pressure loss. This will, however, increase the complexity of the TES installation and this set-up is not considered further in this study.

It is concluded that a TES in a vertical orientation with a height of 25 m is the optimal value for a TES of this size. From a practical point of view, problems with ground water levels in Denmark will most likely be encountered for depths of 25 m, posing challenges for the construction of the storage (Miljøstyrelsen, 2017).

5. Combined TES and power cycle

The performance of the steam Rankine cycle as well as the pressure loss through the boiler are key parameters for determining the overall efficiency of the TES. This section will cover simulations of the 175,000 m^3 conical TES including parameters from the auxiliary system *i.e.* the steam Rankine-cycle and the boiler.

Firstly, two discharge rates of the TES are defined. Using the resulting discharge air flow and temperature as inputs to the Rankine cycle model, optimisations of selected parameters are performed to determine properties of the steam Rankine cycles such as the efficiencies, the total heat exchanger area and optimum operating pressures. The heat exchanger area is then used as a basis for the design of the heat exchanger/boiler. Based on the selected heat exchanger design, the pressure loss across the heat exchanger can be determined. The efficiency of the Rankine-cycle and the pressure loss across the heat exchanger can then be implemented into the TES model and used to determine the fan power required to overcome the pressure loss of the TES and the heat exchanger keeping in mind that the power to drive the fan must originate from the steam Rankine cycle.

The parameters of the conical 175,000 m^3 TES are based on the previous parametric study. The resulting TES has a cylindrical shape and contains rocks with a diameter of 3 cm. The TES is discharged at air mass flow rates of 221.2 kg/s and 442.4 kg/s equivalent to 100 or 200 MW$_{th}$ discharge rates as discussed in the parametric study. The actual discharge rate will depends on the Rankine-cycle model, where the minimum outlet temperature is treated as a constraint.

Cycle performance comparison

For this optimisation, the models for the two investigated steam Rankine cycles are run for two cases for charge rates of 100 MW and 200 MW from the TES corresponding to mass flows of 221.2 $[kg/s]$ and 442.4 $[kg/s]$ respectively.

Two values for the minimum outlet temperature of boiler were also investigated *i.e.* a temperature of 373 and 473 K respectively. Initial optimisations conclude that, for the chosen constraints for the dual pressure SRC, an outlet temperature of 473 K was not realistic. Because the saturation temperature in of the cycle depends greatly on the cycle pressure, a minimum LP cycle pressure of approximately 33 bar was necessary for an outlet temperature of 473 K based on the corresponding saturation temperature and a temperature difference ΔT across the pre-heater of 40 K to ensure that enough heat was available for pre-heating. As a consequence of the minimum requirement for the LP pressure, the steam quality out of the LP cycle turbine would move below the constraint of a steam quality of 0.85. Due to this consideration, a boiler outlet temperature of 473

K is not considered further.

The four chosen cases for optimisation are summarised in the table below:

Cycle type	Charge rates	Boiler outlet temperature
Single Pressure	100 MW (221.2 kg/s)	373 K
	200 MW (442.4 kg/s)	
Dual Pressure	100 MW (221.2 kg/s)	373 K
	200 MW (442.4 kg/s)	

Table 5.1: Summarised cases with selected charge rates and outlet temperature.

The optimisation for both the SP and DP cycles has been carried out for three parameters: maximisation of the total turbine shaft power W_{shaft}, maximisation of the net thermal efficiency η_{th} and maximisation of the ratio of total generated turbine shaft power to the total boiler heat exchanger area W_{shaft}/A_{tot}.

The turbine shaft work to the total boiler heat exchanger area ratio W_{shaft}/A_{tot} can be seen in figure 5.1 and 5.2 for the single- and dual pressure SRC respectively. The value of this ratio is shown for the three previously mentioned optimisation parameters W_{shaft}, η_{th} and W_{shaft}/A_{tot}. This means that, naturally, the value of the W_{shaft}/A_{tot} ratio will be largest for the optimisation run for which it has been optimised.

It can be observed that, for the SP cycle, the work-to-area ratio in figure 5.1, the shaft work in figure 5.5 as well as the thermal efficiency in figure 5.3, are all constant for both discharge rates of 100 and 200 MW. This is due to the fact that the maximum shaft work for the single pressure cycle was obtained at the highest allowable pressure of 140 bar for all cases. The highest obtained work-to-area ratio for the SP cycle is 983 W/m^2.

For the DP cycle in figure 5.2, it can be observed the work-to-area ratio varies slightly between the investigated discharge rates due to a change in the LP cycle pressure between optimisations. The highest obtained work-to-area ratio for the DP cycle is 831 W/m^2, which is approximately 15% lower than the SP cycle.

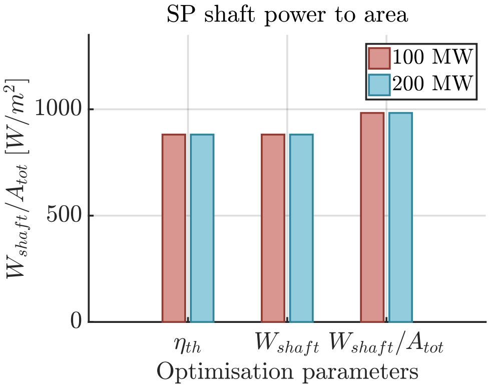

Figure 5.1: The SP Rankine cycle shaft work to area ratio.

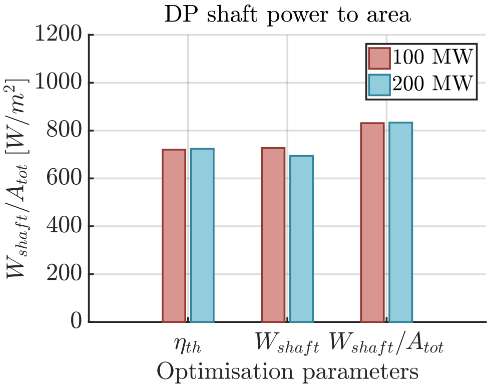

Figure 5.2: The DP Rankine cycle shaft work to area ratio.

The thermal efficiency can be seen in figure 5.3 and 5.4 for the single- and dual pressure cycles respectively. Again, the thermal efficiency for the SP cycle remains constant for both discharge rates as previously mentioned and is approximately the same when optimised for both the shaft power and thermal efficiency with a value of 0.36. This is due to the fact that the thermal efficiency is a function of the produced shaft power. The SP thermal efficiency is slightly lower when optimised for the work-to-area ratio with a value of 0.32 due to a smaller turbine shaft power.

The dual pressure thermal efficiency can be observed to vary slightly between charge rates with a value of approximately 0.35 when optimised for both the thermal efficiency and the shaft power. A slightly lower efficiency of 0.32 is obtained when optimised for the work to area ratio.

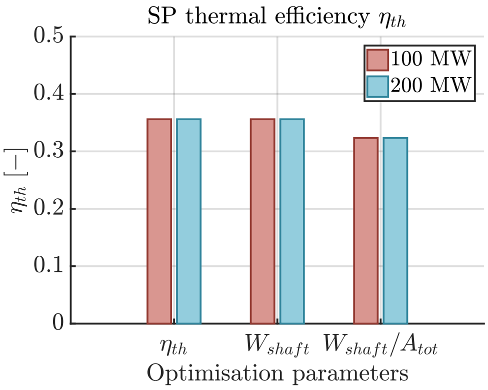

Figure 5.3: The SP Rankine cycle thermal efficiency.

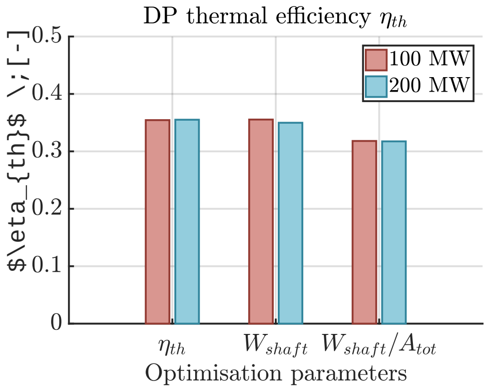

Figure 5.4: The DP Rankine cycle thermal efficiency.

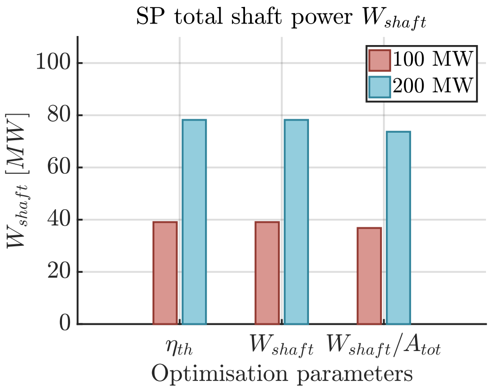

Figure 5.5: The SP Rankine cycle shaft work.

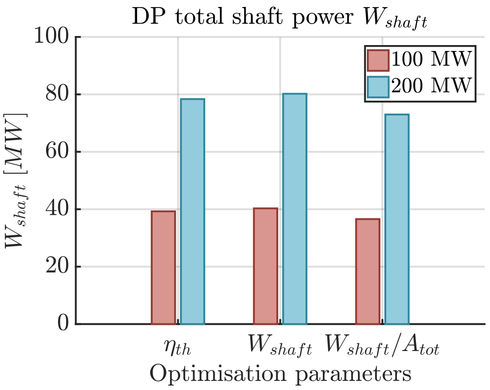

Figure 5.6: The DP Rankine cycle shaft work.

The total turbine shaft work can be seen in figure 5.5 and 5.6 for the single- and dual pressure cycles respectively. The shaft work for both cycles can be seen to approximately double between cycles of 100 and 200 MW charge rates. The highest turbine shaft work for the SP cycle was 39.07 MW for 100 MW discharge rate and 78.22 MW for 200 MW charge rate. In comparison, the DP cycle obtained a maximum shaft work of 40.3 MW for 100 MW discharge rate and 80.21 MW for 200 MW discharge rates. This yields a 3.1% lower shaft work of the SP cycle for 100 MW charge rate and a 2.5% lower shaft work for 200 MW charge rate when compared to the DP cycle. When comparing the total heat exchanger areas of the SP and DP cycles when optimised for maximum shaft work, the total DP heat exchanger area is 21.3% higher than the SP area for 100 MW discharge charge rate and 30.1% higher for 200 MW discharge rate.

When optimised for maximum turbine shaft work, the DP cycle was capable of producing 40.3 MW while the SP cycle produced 39.07 for a 100 MW TES discharge rate, slightly higher shaft work than the SP cycle but at the expense of a significant increase in the total heat exchanger areas. When optimised for maximum work-to-area ratio, the SP cycle was capable of producing 983 W/m^2 while the DP cycle produced 831 W/m^2 for a 100 MW TES discharge rate, approximately 15% less than the SP cycle. Optimisation of the thermal efficiencies revealed that both cycles displayed similar performance with a thermal efficiency of approximately 0.36 for a 100 MW TES discharge rate. The LP turbine exit quality was found to be the limiting factor in the DP SRC with the chosen superheating temperature in the LP cycle, the minimum outlet temperature of the boiler of 100°C affecting the minimum LP cycle saturation pressure and the chosen pinch temperatures.

Compared to the single pressure cycle performance, it can be concluded that, at the current outlet temperature constraints, a dual pressure cycle performs only marginally better than a simple single pressure system. For the current constraints, a different type of cycle, for example a reheat cycle, could possibly perform better for the current constraints and improve the moisture levels at the LP turbine outlet. The turbine must be dimensioned to the discharge rate of the storage because the pressures and maximum allowable steam mass flow rates must remain within the specified ranges.

Because a high shaft work and a low pressure loss through the boiler are both key factors for determining the overall TES system efficiency, the work-to-area ratio is chosen as the most reasonable optimisation parameter. The key results and differences between the SP and DP steam Rankine cycles when optimised for maximum work-to-area ratio for 100 and 200 MW discharge rates can be seen in table 5.2.

Optimised parameters (100 MW)	**SP**	**DP**
P_{HP} [bar]	37.74	31.9
P_{LP} [bar]	-	3.6
A_{tot} [m^2]	37448	44055
W_{shaft} [MW]	36.81	36.57
W_{shaft}/A_{tot} [W/m^2]	983	831
W_{el} for $\eta_{el} = 0.96$ [MW$_{el}$]	35.34	35.11
η_{th} [-]	0.3232	0.3181
η_{ex} [-]	0.4767	0.4692
Optimised parameters (200 MW)	**SP**	**DP**
P_{HP} [bar]	37.74	30.89
P_{LP} [bar]	-	3.61
A_{tot} [m^2]	74964	87579
W_{shaft} [MW]	73.68	72.99
W_{shaft}/A_{tot} [W/m^2]	982.9	833.3
W_{el} for $\eta_{el} = 0.96$ [MW$_{el}$]	70.73	70.07
η_{th} [-]	0.3232	0.3174
η_{ex} [-]	0.4767	0.4681

Table 5.2: Summarised values for the chosen optimisation parameter W_{shaft}/A_{tot}.

Additional properties and results for the SP and DP steam Rankine cycles optimised for a maximum work-to-area ratio can be found in appendix G.

Considering the increased complexity of a dual pressure SRC compared to the simple single pressure SRC as well as limited gains in shaft power for the DP system for the chosen constraints, the single pressure SRC is concluded to be superior in this investigation.

5.1 Heat exchanger design

The heat exchanger is designed based on the maximum allowable pressure loss that can be introduced to the system during a discharge. The effect of the pressure loss on the fan loss fraction can be seen for a air mass flow rate of 221.2 kg/s, corresponding 115 MW_{th} discharge rate in figure 5.7 and for 442.4 kg/s or 230 MW_{th} in figure 5.8. The charge rate is based on an average boiler outlet temperature of 413 K as found during SRC optimisation in section 5. These figures shows that the pressure loss in the heat exchanger should be kept below a certain point to prevent the fan from using excessive amounts of power.

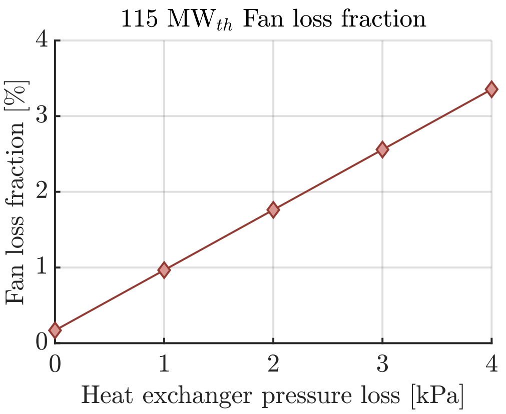

Figure 5.7: The thermal loss through the floor walls and roof during the charge-discharge cycle for the conical TES.

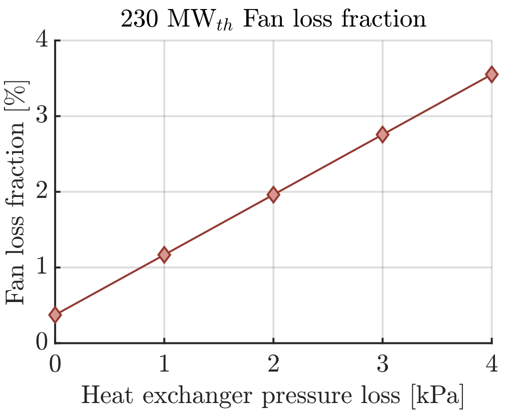

Figure 5.8: The thermal loss through the floor walls and roof during the charge-discharge cycle for the cylindrical TES.

This puts some restrictions on how the heat exchanger should be designed. If a desired maximum fan loss fraction is set to 1%, the pressure loss through the heat exchanger must be kept about 1 kPa. Any higher and the fan loss fraction will increase with about 1% per 1 kPa increase in pressure loss. The thermal losses in the TES is about 0.7% to 1% for comparison. Based on this, a maximum desired pressure loss of 1 kPa is chosen.

Based on the efficiency index for the heat exchanger described in section 3.2, the dimensions of the heat exchanger are determined. Figures 5.9 and 5.10 show how the efficiency index is affected at air flow rates of 221.2 and 442.4 kg/s with the heat exchanger surface areas determined in the table 5.2. As it can be seen, a transverse tube pitch of 10 cm yields the highest efficiency index in both cases while the channel width only has a small effect. This happens because the effective heat transfer coefficient benefits from the smaller transverse pitch and is greatly reduced at a higher transverse pitch. The increase in the efficiency index at higher channel widths is caused by the lower pressure loss caused by the channel width. A transverse pitch of 10 cm is therefore used in the heat exchanger.

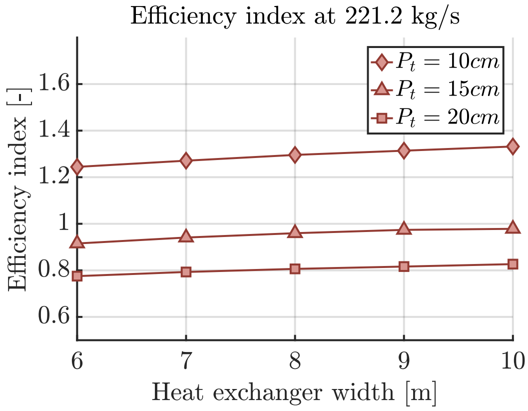

Figure 5.9: Efficiency index for an air flow rate of 221.2 kg/s at increasing channel width and transverse pitch.

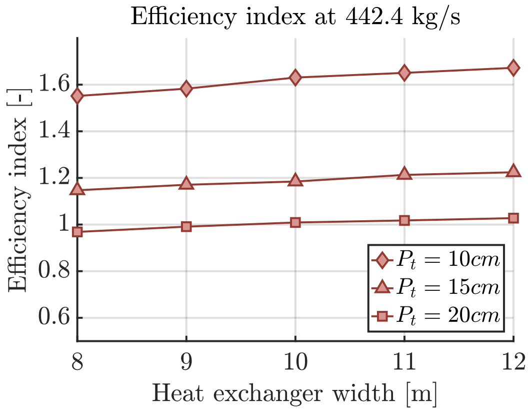

Figure 5.10: Efficiency index for a air flow rate of 442.4 kg/s at increasing channel width and transverse pitch.

At a pressure loss of 1 kPa, the heat exchanger channel would be 9 x 9 m and the heat exchanger would be 3.5 m long at a mass flow rate of 221.2 kg/s and a surface area of 37,448 m^2. Likewise, for a mass flow rate 442.4 kg/s and a surface area of 74,964 m^2, the heat exchanger would need to have a channel that is 12 x 12 m while being 3 meters long

These dimensions of the heat exchangers result in some complications. The large width of the heat exchanger is impractical when considering the support of the tube rows. Furthermore, the air needs to be properly distributed by an expanding duct across the heat exchanger. To avoid flow stall in the expanding duct, flow correction devices such as guide vanes may be required. In order to keep this as simple as possible, it is determined that a discharge mass flow rate of 221.2 kg/s should be used in the final TES system. This will mean that the smaller Rankine system is used. This TES system will be able to produce 35.34 MW_{el} during discharge.

5.2 TES system performance

With the properties for the Rankine-cycle that directly affect TES performance determined, the overall performance of the system will be evaluated. This will result in the actual capacity and efficiencies for the combined TES system. Based on the earlier results, the final system will be designed to have a charge rate of 230 MW_{th} as this does not affect the fan losses much compared to the discharge fan losses. Additionally, it may be desirable to charge the TES over a shorter period of time to take advantage of fluctuating energy sources, if these are available to do so. The discharge rate is set to 115 MW_{th} in order to keep the fan losses low and restrain the demands for the heat exchanger dimensions from having a large width to length ratio. This will result in a TES that is able to charge at 230 MW_{th} corresponding to 230 MW_{el} plus the minor fan consumption at about 20-30 kW_{el} while being able to supply 35.34 MW_{el} to the grid for a 115 MW_{th} TES discharge rate.

In the following sections, the actual available capacity of the TES will be discussed along with the charge and discharge times that can be expected for the system.

5.2.1 TES capacity

The TES capacity has up until now been defined by the volume specific heat capacity and the temperature difference between the highest TES temperature and the lowest temperature that the TES is discharged to. This would yield a TES with a maximum temperature of 873 K and a minimum discharge temperature of 413 K to have a capacity of 41.29 GWh_{th}. In a real application, the amount of available energy will be greatly reduced because of the nature of the heat front. The total amount of energy in the TES is limited by the allowable outlet temperature during charge and discharge.

During charging, an outlet temperature that is much higher than the default minimum temperature of the TES will be undesirable. The fan energy used to pump the air through the TES will be subject to the lower density caused by the increased air temperature and the fan itself might not be able to operate at higher temperatures than the design temperature. Based on the Rankine-cycle, the lower TES temperature, and thus the fan default operating temperature, is set to 413 K. If the TES was to be charged to full capacity, the fan would have to endure 873 K which would not be practical. A possible solution to this could be to install a rotary heat exchanger that could cool the air before the fan and heat it up again afterward the air has been compressed.

During discharge of the TES, the same problem occurs. In this case, the constraints for the maximum super heating temperature for Rankine-cycle poses the limit meaning that the temperature should not move below 873 K. While it would be possible to run at a partial load, the temperature of the TES would drop quickly and the process would become ineffective. A possible solution to this could be the implementation of a Brayton gas cycle operating at higher air temperatures.

An additional simulation has been run for which the maximum charge temperature at the floor outlet is allowed to increase to 10 K above 413 K. The same limit is set for the roof outlet during discharge and it is allowed to decrease 10 K below the 873 K. The difference between these two states can be seen in figure 5.11. A discharge curve can be seen up to 10 K below 873 K at the roof outlet. This curve is denounced as the initial state. From this initial condition, the TES has been charged until the floor outlet reaches 10 K above 413 K after 77.4 hours at 230 MW_{th}. The difference between these two curves illustrate how much energy it is possible to add to the TES without increasing the outlet temperature beyond 423 K.

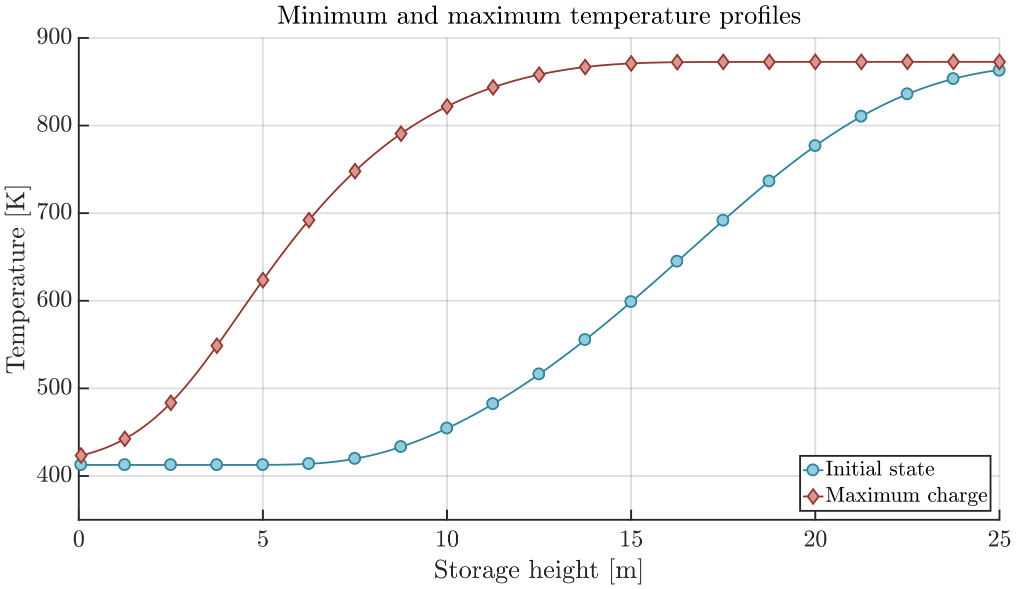

Figure 5.11: Temperature profile at maximum allowable charge and discharge.

This illustrates that a large part of the TES cannot be heated to 873 K at a maximum charge level. At a maximum discharge level, an large part of the TES cannot be cooled to 413 K. The heat fronts are expressed as energy stored per meter of storage as seen in figure 5.12. This corresponds to the amount of energy being stored at the maximum charge to be 76.0% of the 41.29 GWh_{th}. The energy stored at the initial state is 35.5% of the 41.29 GWh_{th}

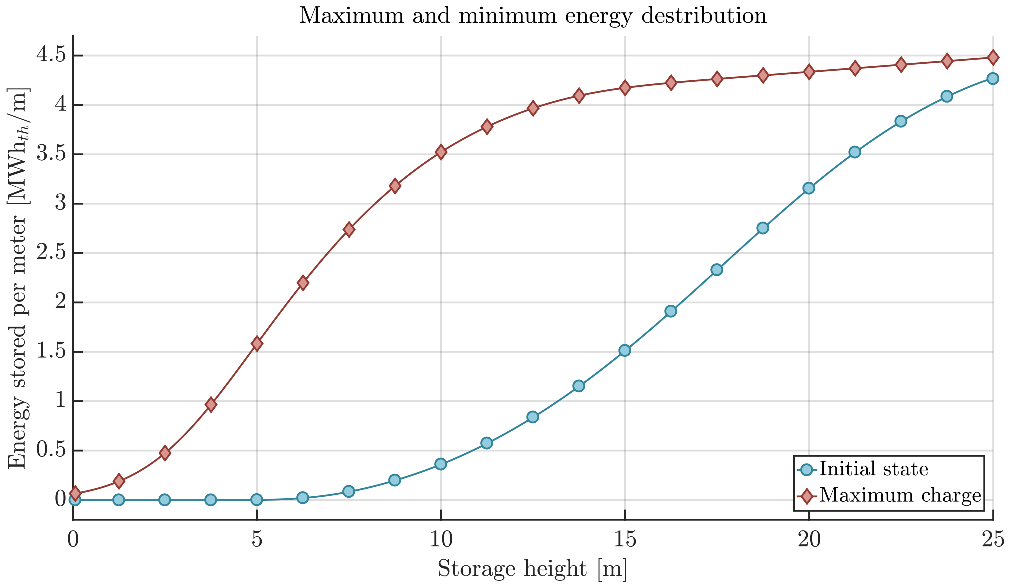

Figure 5.12: Energy distribution at maximum allowable charge and discharge levels.

If energy stored at the maximum charge level is used as the maximum amount of energy in the TES and the energy stored at the maximum discharge level is used as the minimum amount of energy stored by the TES, the total capacity of the TES becomes 16.7 GWh_{th} *i.e.* 40.5% of the before defined 41.29 GWh_{th}. This essentially means that 59.5% of the storage volume of rocks in the TES are not utilised corresponding to a volume of 104,144 m^3 out of the total 175,000 m^3.

This is, in part, caused by the relatively short length of the TES. With a height of 25 m, the pressure loss is kept low. This, in turn, also causes the heat front to cover a longer part of the TES resulting in the tendency as seen above. This effect is, furthermore, increased over time with conduction and radiation slowly causing the heat to move downwards in the TES. This means that the heat front will continually increase in length. Over many charge-discharge cycles, this will cause the gap between the charged and discharged heat front to be decrease in size effectively decreasing the useful storage volume. This is further explained in appendix H where the model has been run for many consecutive charge/discharge cycles.

5.2.2 TES charge and discharge times

Figure 5.13 shows the temperature at the floor outlet for the charge period to the maximum charge state described above. As previously stated, the charge time is 77.4 hours before the temperature reaches 10 K above 413 K. The curve shows that temperature begins to increase at the floor outlet after 50 hours of charging, but only increases beyond 414 K after 60 hours. At this point, however, the temperature begins to increase rapidly. If charging is continued after 77.4 hours, the temperature at the floor outlet would increase rapidly.

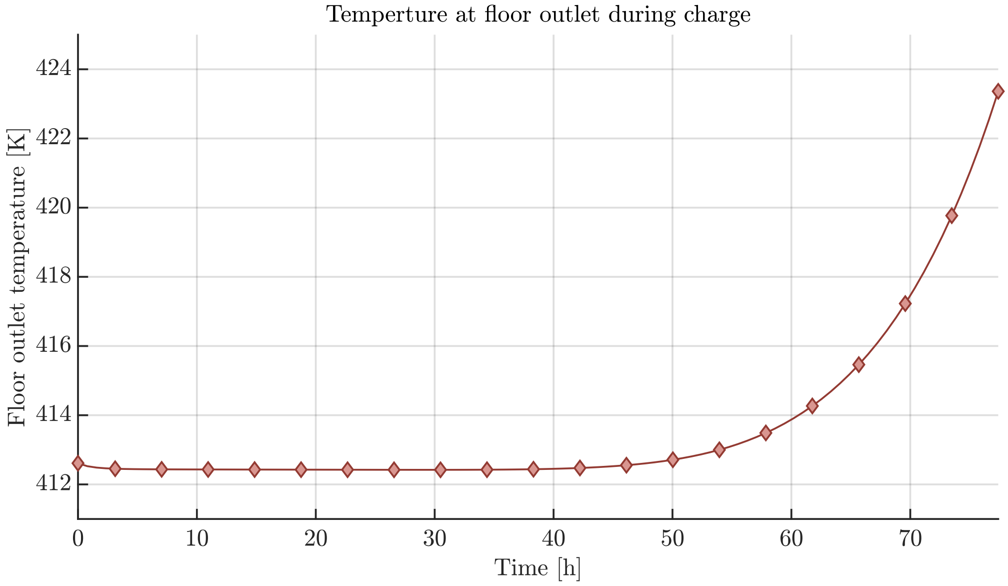

Figure 5.13: Temperature at the floor outlet during charge of the TES.

Figure 5.14 shows the temperature at the roof outlet over a discharge period following the charge period in figure 5.13. This discharge period takes place over 154.8 hours, twice the time of the charge period, at a rate of 115 MW_{th}, half the rate of the charge period. This shows that the temperature will decrease below the before mentioned 10 K limit for a discharge roof outlet temperature of 873 K. This is mainly due the axial conduction and radiation as previously mentioned. This implies that, during discharge, a lower amount of energy can be extracted than was added to the TES during charge if the discharge limit is set to 10 K below the maximum temperature of 873 K.

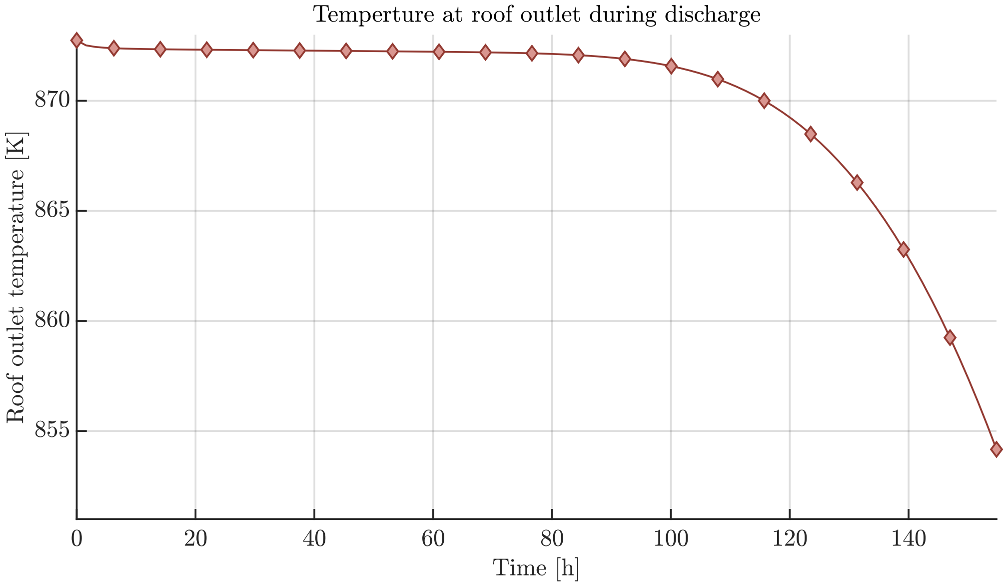

Figure 5.14: Temperature at the roof outlet during discharge of the TES.

From figure 5.14 it can be seen that the TES can be discharged for approximately 100 hours at an approximately constant temperature. Over the following 20 hours, the temperature drops to 869 K. Past this point, the temperature drops rapidly and at 140 hours, the temperature reaches 863 K. At this temperature, the discharge should be stopped to avoid further decrease in the temperature.

5.2.3 TES efficiency

During the charge-discharge cycle it is only possible to charge the TES for a period of 77.4 hours. Similarly, a following discharge period cannot exceed 140 hours if the temperature is to be kept from decreasing to much. The efficiencies and loss fractions for the TES for this particular charge/discharge cycle are shown in table 5.3 that also contains the data for the discharge of 154 hours to illustrate the effect of a decrease in the temperature.

Cycle efficiencies	η_{cycle} [%]	ψ_{cycle} [%]
154 hour discharge	98.52	98.11
140 hour discharge	88.92	88.62

Cycle loss fractions	f_{fan} [%]	f_{roof} [%]	f_{wall} [%]	f_{floor} [%]
154 hour discharge	0.91	0.17	0.11	0.12
140 hour discharge	0.92	0.18	0.11	0.13

Table 5.3: Efficiencies and loss fractions for the charge/discharge cycle performed at with a discharge period of 154 hours and 140 hours.

The efficiencies in table 5.3 show that the 154 hour discharge period is very effective as it recovers 16.6210 GWh$_{th}$ of the 16.7179 GWh$_{th}$ added during the charge cycle. The exergy efficiency is not affected much due to the discharge temperature only decreasing in the last hours. This means that, overall, the recovered exergy is still high compared to the exergy added to the system.

The 140 hour discharge period only recovers 15.0014 GWh$_{th}$, which is the main reason for the large difference between the two discharge periods. This shows that the efficiency of a full cycle is limited by the amount of energy that can be recovered before the temperature drops due to the heat front increasing in length over the time period of the cycle.

The efficiency of the 140 hour discharge period may be lower due to the lengthening of the heat front caused by the axial conduction. This causes the energy to be stored in the lower parts of the TES at a lower temperature.

5.3 Discussion

In this chapter the combined performance of the TES and the discharge cycle has been investigated. The TES can operate at very high efficiencies in terms of energy and exergy. The main issue concerns the elongation of the heat front longer over time thus limiting the amount of energy that can be withdrawn at the maximum outlet temperature during discharge. This also leads to a poor volume efficiency where most of the TES volume cannot be utilised during continuous operation and cycling.

In the study above, the TES was charged to a maximum capacity and discharged immediately after. In a real scenario the cycling will depend greatly on energy availability, energy prices and the demand. The storage will, most likely, be charged when excess electricity is available and discharged when electricity is demanded. This means that the TES will not always be charged to full capacity or discharged to minimum capacity. Furthermore, the TES will undergo storage periods where the energy with no charging or discharging taking place. This will, over time, cause the heat front to become even longer due to conduction and radiation meaning that the temperature at the roof of the TES during a storage period will decrease. Thermal losses to sorroundings during storage periods will also play a role in a practical scenario.

Charging the TES will increase the roof temperature to the maximum again but the slope of the heat front will still be affected and the possible discharge time at maximum temperature will, thus, be decreased.

The charge period also puts a limit on how much the TES can be charged. As shown earlier, the TES cannot be charged to full capacity as the outlet temperature of the TES directly affects the power required to drive the fan.

One possible way to prevent the fan efficiency from being affected by the temperature of the hot discharge air could be to cool the air from the floor outlet of the TES before it reaches the fan. A rotary heat exchanger could be implemented into the charge cycle as shown in figure 5.15.

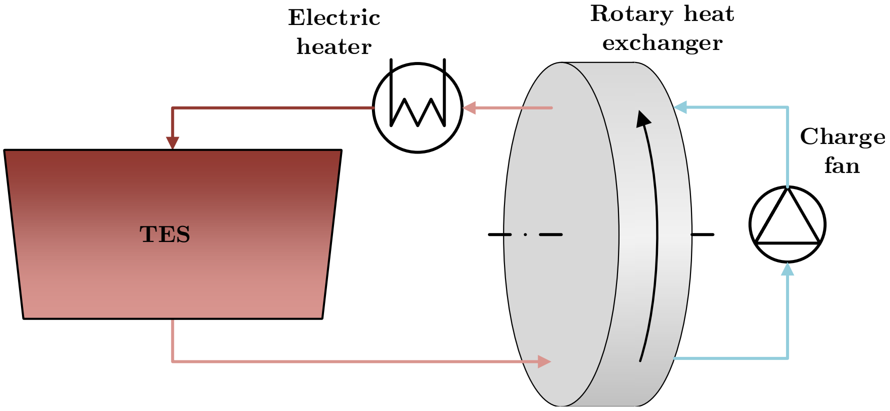

Figure 5.15: Charge cycle modified with a rotary heat exchanger.

As seen from the figure, the rotary heat exchanger would allow for the fan to operate at a lower temperature with the heat being extracted from the air before the fan and added once again downstream of the fan. By doing so, the TES could be charged to a higher capacity, which will increase the outlet temperature of the charge air. In this way, the heat is recycled back in to the TES without affecting the fan operation and overall TES efficiency to a noticeable degree. The rotary heat exchanger will, however, introduce an additional pressure loss. Despite this, the fan will be cost less to operate during the charge period since the required power does not have to be subtracted from the power generated by the Rankine-cycle. The rotary heat exchanger will, furthermore, be bypassed as long as the floor temperature of the TES is not increased during the charge period and will, thus, only be used for the last boost in capacity.

The cost of charging the TES to full capacity from the point at which the floor temperature begins to increase beyond the minimum TES temperature will be higher because of the pressure loss introduced by the rotary heat exchanger. Despite this, the implementation of a heat exchanger in the charge cycle could possibly allow for a better utilisation of the TES volume and increase storage capacity from around 40% of the theoretical maximum to about 65% in the best case.

A possible solution for increasing the actual TES capacity would be to split the TES into several smaller or compartments sections. These would be insulated from each other thus reducing the effect of axial conduction and radiation making it possible to maintain a steeper heat front for longer a longer time period. Another solution for maintaining a constant discharge temperature for extended discharge periods is to introduce a mixed storage utilising solids like rocks and an encapsuled phase change material in the top part of the storage as suggested by Zanganeh (2014).

The main limitation of the TES as presented in this study is the limitation in the amount of high temperature energy that can be provided for extended periods of time which limits the effective capacity of the TES. This can possibly be improved by increasing the TES volume for the relevant storage application or by implementing the improvements as previously discussed. It can be concluded that the energy- and exergy efficiencies of complete charge/discharge cycles are generally very high proving that the TES can effectively store energy as heat with a high return ratio and at high temperatures.

The investigated dual pressure SRC was found to be limited the constraints for the low pressure cycle due to requirements for the minimum boiler outlet temperature. Other power cycles such as the re-heat and Brayton gas cycles may have a potential to produce even more power for the given constraints provided that the temperature of the discharge air can be raised to the required levels for optimum cycle performance.

6. Conclusion

The objective of this study has been to investigate the behaviour of a packed bed, High Temperature Thermal Energy Storage (HT-TES) in conjunction with an auxiliary system consisting of a charge cycle, a discharge cycle and a power generating Steam Rankine cycle. The investigated conical storage had a volume of 175,000 m^3, a height of 25 m and a lid and bottom radius of 49.19 m and 45.19 m respectively. Rocks were utilised as a solid storage medium with air as a secondary heat transfer medium.

A dynamic model of the Thermal Energy Storage was created resembling a modified version of the original Schumann model for packed beds. The model incorporates temperature dependent properties for both the fluid- and solid phases. It treats heat transfer by forced convection and contains terms accounting for axial transport of energy by conduction and radiation. The pressure loss through the TES has been modelled using a modified version of the Ergun equation. The model was solved using the method of lines and the ode15s solver in Simulink. A grid independence study concluded that 400 grid points were required to obtain a satisfactory accuracy of the heat front length in the TES. The model was validated using results obtained by Zanganeh (2014) for a simulation of 30 charge/discharge cycles over 30 days.

A parametric study was carried out, investigating the effect of selected parameters on the performance of the TES. Two general shapes of the storage were investigated. It was concluded that the difference between a conical and a cylindrical TES were negligible in terms of internal heat distribution and thermal losses.

The diameter of the solid particle storage material was investigated. It was determined that rocks with a diameter of 1 cm caused an unacceptably high pressure loss while rocks with diameters above 5 cm yielded an unreasonably high Biot number. Therefore, a rock diameter of 3 cm was chosen for the TES.

The effect of varying the charge/discharge rate was investigated. It was concluded that the TES should not be charged or discharged at a rate higher than 553 kg/s as this would increase the Biot number beyond the acceptable limit.

The effect of varying the thickness of the insulation material on the walls, floor and roof of the storage was investigated. It was determined that the initial insulation thicknesses, up to 0.6 m, could be reduced by as much as 40% without increasing the thermal losses beyond 1% of the energy recovered during the discharge phase.

The length of the TES was investigated for a cylindrical storage with a constant radius in relation to the Biot number and the pressure loss through the storage. It can be concluded that a height of 25 m is the maximum allowable for the TES.

It was concluded that both the energy- and exergy efficiencies obtained from the parametric study for all but the extreme cases, remained above 98%.

Rankine cycle models were developed for a single- and a dual pressure steam Rankine cycle as a part of the auxiliary system utilising Engineering Equation Solver. For the Rankine cycle optimisation, the ratio of the turbine shaft work to the total heat exchanger area was chosen as the most applicable optimisation parameter due to the close coherence of this parameter with the total TES performance.

Optimisation of the modelled single- and dual pressure steam Rankine cycles conclude that, when optimised for the maximum turbine shaft work to heat exchanger area ratio for the current constraints, the two cycles had similar electrical power outputs. For a discharge air mass flow rate of 221.2 kg/s, the single pressure cycle produced 35.34 MW_{el} with a shaft work to heat exchanger area ratio of 983 W/m^2. Based on the chosen optimisation parameter and system complexity, the single pressure steam Rankine cycle is considered superior to the dual pressure cycle for the relevant constraints. Both cycles investigated operated of thermal efficiencies of approximately 0.32. The maximum pressure loss introduced to the system by the Rankine cycle boiler was limited 1 kPa. Based on this, a maximum air mass flow rate of 221.2 kg/s during discharge was chosen to comply with this.

A realistic thermal capacity for the 175,000 m^3 TES was estimated at 16.7 GWh_{th} *i.e.* 40.5% of the theoretical capacity of the rocks by volume. This was based on an inlet discharge temperature to the storage of 413 K, based on the modelled outlet temperature of the Rankine cycle boiler, and an outlet discharge temperature from the storage of 873 K. This means that 104,144 m^3 of the total volume of 175.000 m^3 could not be effectively utilised to store useful energy due to the nature of the heat front.

The charge time at a rate of 230 MW_{th} was found to be 77.4 hours or 3.2 days while the discharge time was determined to be 140 hours or 5.8 days at a discharge rate of 115 MW_{th}. It was concluded that, for this particular case, the cycle energy efficiency was 88.92 if the temperature of the TES outlet should not be decreased beyond 863 K.

7. Future work

This chapter is dedicated to the presentation of possible future studies based on this thesis. These subjects are related to model improvements, system investigations and optimisation parameters.

The increasing complexity of the model implemented in Simulink have caused the initialisation time of Simulink to become longer than the actual simulation time. If the Simulink model is to be improved upon by adding additional terms, the initialisation time will further increase. Furthermore, with all features implemented, 400 grid points is the limit of the Simulink model. Simulating the TES in a configuration that requires 600 or 800 grid points is not feasible. The model of the TES could be converted from Simulink to another program, possibly a standard Matlab script, to improve calculation time and accuracy.

In this thesis, the overall TES efficiency has been based on charge/discharge cycles that utilise a large part of the TES capacity. The TES efficiency should be determined in a more realistic scenario. The actual charge period could be based on an analysis of when excess electricity generally is available and in what quantities. Likewise, an analysis of the general demand for electricity would be needed to determine actual discharge periods. These analyses would also be required to investigate the economy of operating a TES and for which the capacity of the TES should be designed.

While the cycle efficiency of the TES is high, the volume that can be utilised for actual storage is low. This means that a large amount of the volume in the TES is essentially not utilised for useful energy storage.

Some ways to increase the capacity of the TES were discussed in section 5.3 and include:

- Splitting the TES into several smaller sections that are individually insulated to avoid the effects of axial conduction and radiation
- Implementation of an encapsulated phase change material at the top of the TES that would ensure constant outlet temperature for extended time periods
- Charging the of the entire TES storage volume to 873 K. This will, however, require that the fan is protected as the air begins to heat up in the charge cycle when the bottom of the TES heats up.

The thermal efficiency of the single pressure Rankine cycle used in this study reached 32% when optimised for shaft work over heat exchanger area. Other types of power cycles should be investigated to determine if the efficiency could be improved even further. Such power cycles could include a Rankine cycle with reheat and a Brayton gas cycle as discussed in section 5.3.

Bibliography

Christian B. Friberg. Milj ørapportering - elproduktion, April 2016. URL `http://www.energinet.dk/DA/KLIMA-OG-MILJOE/Miljoerapportering/Termisk-produktion/Sider/Termisk-produktion.aspx`.

Nord Pool AS. The market members - producers. URL `http://www.nordpoolspot.com/How-does-it-work/The-market-members/Producers/`.

Kenneth Lykkedal. Nord pool spot - det førende elmarked i europa, 2016. URL `http://www.vindenergi.dk/images/editor/pdf/nord_pool.pdf`.

Danmarks Vindmølleforening. Faktablad t7 - import og eksport af vindmøllestrøm, June 2015. Fakta om Vindenergi.

M. A. Tahat, R. F. Babus'Haq, and P. W. O'Callaghan. Thermal energy storage. *Building Serv. Eng. Res. Technol.*, 14(1):1–11, 1993.

Guruprasad Alva, Lingkun Liu, Xiang Huang, and Guiyin Fang. Thermal energy storage materials and systems for solar energy applications. *Renewable and Sustainable Energy Reviews*, 68, Part 1:693 – 706, 2017. ISSN 1364-0321. doi: http://dx.doi.org/10.1016/j.rser.2016.10.021. URL `http://www.sciencedirect.com/science/article/pii/S1364032116306700`.

Harmeet Singh, R.P. Saini, and J.S. Saini. A review on packed bed solar energy storage systems. *Renewable and Sustainable Energy Reviews*, 14(3):1059 – 1069, 2010. ISSN 1364-0321. doi: http://dx.doi.org/10.1016/j.rser.2009.10.022. URL `http://www.sciencedirect.com/science/article/pii/S1364032109002536`.

S. Kalaiselvam and R. Parameshwaran. *Thermal Energy Storage Technologies for Sustainability - System Design, Assessment and Applications.* Academic Press, 2014. ISBN: 978-0-12-417291-3.

Giw Zanganeh. *High-Temperature Thermal Energy Storage for Concentrated Solar Power with Air as Heat Transfer Fluid.* PhD thesis, ETH Zü rich, 2014.

T.E.W. Schumann. Heat transfer: A liquid flowing through a porous prism. *Journal of the Franklin Institute*, 208(3):405 – 416, 1929. ISSN 0016-0032. doi: http://dx.doi.org/10.1016/S0016-0032(29)91186-8. URL `http://www.sciencedirect.com/science/article/pii/S0016003229911868`.

Sabri Ergun and A. A. Orning. Fluid flow through randomly packed columns and fluidized beds. *Industrial & Engineering Chemistry*, 41(6):1179–1184, 1949. doi: 10.1021/ie50474a011. URL `http://dx.doi.org/10.1021/ie50474a011`.

J.Pascal Coutier and E.A. Farber. Two applications of a numerical approach of heat transfer process within rock beds. *Solar Energy*, 29(6):451 – 462, 1982. ISSN 0038-092X. doi: http://dx.doi.org/10.1016/0038-092X(82)90053-6. URL `http://www.sciencedirect.com/science/article/pii/0038092X82900536`.

L. Geissbühler, M. Kolman, G. Zanganeh, A. Haselbacher, and A. Steinfeld. Analysis of industrial-scale high-temperature combined sensible/latent thermal energy storage. *Applied Thermal Engineering*, 101:657 – 668, 2016. ISSN 1359-4311. doi: http://dx.doi.org/10.1016/j.applthermaleng.2015.12.031. URL `http://www.sciencedirect.com/science/article/pii/S135943111501412X`.

Kenneth Guy Allen. Performance characteristics of packed bed thermal energy storage for solar thermal power plants. Master's thesis, University of Stellenbosch, 2010.

Markus Hänchen, Sarah Brückner, and Aldo Steinfeld. High-temperature thermal storage using a packed bed of rocks - heat transfer analysis and experimental validation. *Applied Thermal Engineering*, 31(10):1798 – 1806, 2011. ISSN 1359-4311. doi: http://dx.doi.org/10.1016/j.applthermaleng.2010.10.034. URL `http://www.sciencedirect.com/science/article/pii/S1359431111001062`.

Nicolas Mertens, Falah Alobaid, Lorenz Frigge, and Bernd Epple. Dynamic simulation of integrated rock-bed thermocline storage for concentrated solar power. *Solar Energy*, 110:830 – 842, 2014. ISSN 0038-092X. doi: http://doi.org/10.1016/j.solener.2014.10.021. URL `http://www.sciencedirect.com/science/article/pii/S0038092X14005076`.

Marc Medrano, Antoni Gil, Ingrid Martorell, Xavi Potau, and Luisa F. Cabeza. State of the art on high-temperature thermal energy storage for power generation. part 2 - case studies. *Renewable and Sustainable Energy Reviews*, 14(1):56 – 72, 2010. ISSN 1364-0321. doi: http://dx.doi.org/10.1016/j.rser.2009.07.036. URL `http://www.sciencedirect.com/science/article/pii/S1364032109001786`.

Andreas Hauer. Iea-etsap and irena technology brief e17, 2013. URL `http://www.irena.org/Publications/ReportsPaper2014New.aspx?mnu=cat&PriMenuID=36&CatID=141&type=all`.

Henrik Stiesdal. Vindmøller som aktiver - nu og i fremtiden. PowerPoint, September 2016a.

Geology.com. Rocks: Igneous, metamorphic and sedimentary, 2017. URL `http://geology.com/rocks/`.

G. Zanganeh, A. Pedretti, S. Zavattoni, M. Barbato, and A. Steinfeld. Packed-bed thermal storage for concentrated solar power-pilot-scale demonstration and industrial-scale design. *Solar Energy*, 86(10):3084 – 3098, 2012. ISSN 0038-092X. doi: http://dx.doi.org/10.1016/j.solener.2012.07.019. URL `http://www.sciencedirect.com/science/article/pii/S0038092X12002812`.

Erich Hahne. *Ullmann's Encyclopedia of Industrial Chemistry - Heat Storage Media.* John Wiley and Sons, Inc., 1999-2014. doi: DOI:10.1002/14356007. URL `http://onlinelibrary.wiley.com/doi/10.1002/14356007.a12_b30/pdf`. ISBN: 9783527306732.

Iñigo Ortega-Fernández, Nicolas Calvet, Antoni Gil, Javier Rodríguez-Aseguinolaza, Abdessamad Faik, and Bruno D'Aguanno. Thermophysical characterization of a by-product from the steel industry to be used as a sustainable and low-cost thermal energy storage material. *Energy*, 89:601 – 609, 2015. ISSN 0360-5442. doi: https://doi.org/10.1016/j.energy.2015.05.153. URL `http://www.sciencedirect.com/science/article/pii/S0360544215007823`.

C. Martin, N. Breidenbach, and M. Eck. Screening and analysis of potential filler materials for molten salt thermocline storages. *ASME Energy Sustainability*, Volume 1, 2014. doi: doi:10.1115/ES2014-6493. URL `http://proceedings.asmedigitalcollection.asme.org/proceeding.aspx?articleid=1920612`.

Doerte Laing, Wolf-Dieter Steinmann, Rainer Tamme, and Christoph Richter. Solid media thermal storage for parabolic trough power plants. *Solar Energy*, 80(10):1283 – 1289, 2006. ISSN 0038-092X. doi: https://doi.org/10.1016/j.solener.2006.06.003. URL `http://www.sciencedirect.com/science/article/pii/S0038092X06001538`.

R. Tiskatine, A. Eddemani, L. Gourdo, B. Abnay, A. Ihlal, A. Aharoune, and L. Bouirden. Experimental evaluation of thermo-mechanical performances of candidate rocks for use in high temperature thermal storage. *Applied Energy*, 171:243 – 255, 2016. ISSN 0306-2619. doi: http://doi.org/10.1016/j.apenergy.2016.03.061. URL `http://www.sciencedirect.com/science/article/pii/S0306261916303816`.

Henrik Stiesdal. Stiesdals blog: Den sidste kroelle paa energilagringen - the hot stuff, January 2016b. URL `https://ing.dk/blog/den-sidste-kroelle-paa-energilagringen-hot-stuff-181281`.

T.M. Sanderson and G.T. Cunningham. Performance and efficient design of packed bed thermal storage systems. part 1. *Applied Energy*, 50(2):119 – 132, 1995. ISSN 0306-2619. doi: http://dx.doi.org/10.1016/0306-2619(95)92628-7. URL `http://www.sciencedirect.com/science/article/pii/0306261995926287`.

Sami Hamdi, William E. Schiesser, and Graham W. Griffiths. Method of lines. *Scholarpedia*, 2009.

W.H. Somerton. Chapter v. thermal conductivity of rock/fluid systems. In W.H. Somerton, editor, *Thermal properties and temperature-related behavior of rock/fluid systems*, volume 37 of *Developments in Petroleum Science*, pages 39 – 81. Elsevier, 1992. doi: https://doi.org/10.1016/S0376-7361(09)70025-1. URL `http://www.sciencedirect.com/science/article/pii/S0376736109700251`.

K. K. Kelly. *Contributions to the Data on Theoretical Metallurgy.* U.S. Dept. of the Interior, Bureau of Mines, 1960.

Robert Pfeffer. Heat and mass transport in multiparticle systems. *Industrial & Engineering Chemistry Fundamentals*, 3(4):380–383, 1964. doi: 10.1021/i160012a018. URL `http://dx.doi.org/10.1021/i160012a018`.

Elvio Alanis, Luis Saravis, and Leticia Rovetta. Measurement of rock pile heat transfer coefficients. *Solar Energy*, December 1977.

Edward Barbour, Dimitri Mignard, Yulong Ding, and Yongliang Li. Adiabatic compressed air energy storage with packed bed thermal energy storage. *Applied Energy*, 155:804 – 815, 2015. ISSN 0306-2619. doi: http://dx.doi.org/10.1016/j.apenergy.2015.06.019. URL `http://www.sciencedirect.com/science/article/pii/S0306261915007771`.

J. M. Smith and Daizo Kunii. Heat-transfer characteristics of porous rocks. *Americal Institue of Chemical Engineers*, Vol. 6(1):pp. 71–78, March 1960.

Sakae Yagi and Daizo Kunii. Studies on effective thermal conductivities in packed beds. *Americal Institue of Chemical Engineers*, Vol. 3(3):pp. 373–381, September 1957.

Karl Terpager Andersen. Theory for natural ventilation by thermal buoyancy in one zone with uniform temperature. *Building and Environment*, 38(11):1281 – 1289, 2003. ISSN 0360-1323. doi: https://doi.org/10.1016/S0360-1323(03)00132-X. URL `http://www.sciencedirect.com/science/article/pii/S036013230300132X`.

I. F. Macdonald, M. S. El-Sayed, K. Mow, and F. A. L. Dullien. Flow through porous media-the ergun equation revisited. *Industrial & Engineering Chemistry Fundamentals*, 18(3):199–208, 1979. doi: 10.1021/i160071a001. URL `http://dx.doi.org/10.1021/i160071a001`.

Ibrahim Dincer and Marc A. Rosen. *Thermal Energy Storage*. Wiley, 2010. URL `https://ebookcentral.proquest.com/lib/aalborguniv-ebooks/detail.action?docID=589273`.

Robert J. Krane. A second law analysis of the optimum design and operation of thermal energy storage systems. *International Journal of Heat and Mass Transfer*, 30(1):43 – 57, 1987. ISSN 0017-9310. doi: http://dx.doi.org/10.1016/0017-9310(87)90059-7. URL `http://www.sciencedirect.com/science/article/pii/0017931087900597`.

Behnaz Rezaie, Bale Reddy, and Marc A. Rosen. Seasonal stratified thermal energy storage exergy analysis. In *The Canadian Conference on Building Simulation*. Faculty of Engineering and Applied Science, University of Ontario Institute of Technology, 2012.

Burmeister & Wain. Ultra super critical boilers, 2016. URL `http://www.bwe.dk/download/brochures_pdf/bwe10-0006_8.pdf`.

Yunus A. Cengel and Michael A. Boles. *Thermodynamics - An Engineering Approach*. McGraw-Hill, 8th edition edition, 2015.

R. W. Haywood. *Analysis of Engineering Cycles*. Pergamon Press, 2nd edition edition, 1975. ISBN: 0-08-017947-9.

Siemens AG. Turbines for biomass plants, 2014. URL `https://www.energy.siemens.com/us/pool/hq/power-generation/renewables/biomass-power/Biomass_Turbines_EN.pdf`.

ESCOA. *ESCOA TURB-X SF finned tube data sheet*, 1979.

Tian Jian Lu, Feng Xu, and Ting Wen. *Thermo-Fluid Behaviour of Periodic Cellular Metals*. Springer, 2013. ISNB: 978-3-642-33523-5.

Miljøstyrelsen. Grundvandskort, 2017. URL `https://www.dingeo.dk/kort/grundvand/`.

Kamal A. R. Ismail and Rubens Stuginski Jr. Analysis of possible models for fixed bed. In *11th ABCM Mechanichal Engineering Conference*, 1991.

Yunus A. Cengel, John M. Cimbala, and Robert H. Turner. *Fundamentals of Thermal-Fluid sciences*. McGraw Hill, 2012. ISBN:978-007-132511-0.

John Beek. Design of packed catalytic reactors. *Advances in Chemical Engineering*, 3:203 – 271, 1962. ISSN 0065-2377. doi: http://dx.doi.org/10.1016/S0065-2377(08)60060-5. URL `http://www.sciencedirect.com/science/article/pii/S0065237708600605`.

Kunihiko Ofuchi and Daizo Kunii. Heat-transfer characteristics of packed beds with stagnant fluids. *Heat and Mass Transfer*, Vol. 8:pp. 749–757, December 1965.

A. Schumann's model

The basic, one dimensional Schumann model was developed in 1929 and describes the transient heat transfer by the convection of fluid and the heat transfer between he fluid and solid phases (Schumann, 1929). The Schumann model is based on the several assumptions (Ismail and Jr., 1991): The properties of the fluid and solid phase are constant and independent of temperature, the flow is steady and incompressible, no axial or radial heat conduction or radiation and lastly, the Biot number is assumed to be below 0.1 meaning that no internal temperature gradient in the solid particles.

The equation for the fluid phase can be written as:

$$\underbrace{\varepsilon V \rho_f c_{p,f}}_{\text{Fluid phase capacity}} \left(\frac{dT_f}{dt} + v_f \frac{dT_f}{dx} \right) = \underbrace{h_{vol} V \left(T_s - T_f \right)}_{\text{fluid-solid phase convection}} - \underbrace{U_{wall} A_{wall} \left(T_f - T_\infty \right)}_{\text{loss to surroundings}} \tag{A.1}$$

The equation for the solid phase is written as:

$$\underbrace{\left(1 - \varepsilon\right) V \rho_s c_{p,s}}_{\text{Solid phase capacity}} \frac{dT_s}{dt} = - \underbrace{h_{vol} V \left(T_s - T_f \right)}_{\text{fluid-solid phase convection}} \tag{A.2}$$

Equation A.1 shows how the capacity of the fluid is taken into account in relation to time and also axial distance in terms of fluid velocity. The equations also incorporate a fluid-solid phase convection term that accounts for the transfer of energy in either direction. This is the only heat transfer between the two phases that the Schumann model takes into account based on the volumetric heat transfer coefficient in this instance. Finally, a term describing the losses to the surroundings is implemented, based on the overall heat transfer through the walls and the wall area.

Equation A.2 is more simple than equation A.1 and accounts for the transient temperature change of the solid phase in relation to the solid phase energy capacity and the energy transferred from- or to the solid phase from the fluid phase through convection.

The model developed in this study is based on the Schumann model but incorporates terms and modifications that improves the accuracy of the model.

B. Model solver

The model described in chapter 2.1 is implemented in Matlab Simulink and solved using the build in ode15s solver. The model has thus been discretised in the axial direction and solved using the method of lines. This appendix describes how the individual grid point model block determines the radius at the inlet and at the outlet of the grid point along with a detailed description of how the individual model blocks are constructed.

B.1 Geometrical calculations

As the TES can be simulated as a conical tank and in two directions depending on the flow direction, some geometrical calculations must be defined. The height of the individual grid layer is defined by the total TES height divided by the number of grid points $\Delta x = H_{TES}/N$. A grid layer in a conical TES will have different inlet and outlet radii and they are calculated for the charge phase as:

$$R_{out,charge} = R_{roof} - (R_{roof} - R_{floor})\,\frac{n}{N} \tag{B.1}$$

$$R_{in,charge} = R_{roof} - (R_{roof} - R_{floor})\,\frac{n-1}{N} \tag{B.2}$$

and for the discharge phase in reverse order the radii are calculated as:

$$R_{out,discharge} = R_{floor} + (R_{roof} - R_{floor})\,\frac{n}{N} \tag{B.3}$$

$$R_{in,discharge} = R_{floor} + (R_{roof} - R_{floor})\,\frac{n-1}{N} \tag{B.4}$$

With the height and radii defined, the cross-sectional in- and outlet areas along with the Grid layer volume can be obtained.

B.2 Grid point model structure

Each grid point or layer calculates the temperature of the fluid and solid phases contained in the volume associated with the grid point or layer. Figure B.1 gives a detailed overview of the model structure in Simulink. Generally, the model calculates 3 parameters: the energy of the 2 phases and the pressure loss across the grid layer. All geometrical calculation are based on the grid point number as this determines the location in the TES and the subsequent radius. All the model blocks require the geometrical data for the grid point.

The thermal properties of the fluid is determined through property lookup tables and require the temperature of the fluid at both the inlet and the outlet of the grid point and in some cases also the pressure at the grid point.

The fluid enthalpy change is calculated based, primarily, on the convection by flow, which requires the enthalpy for the inlet and the outlet of the grid layer, and the fluid-solid phase convection that relies on the temperature of the fluid and solid phases.

The loss to the surroundings is based on the internal temperature of the fluid phase at the grid point and is determined based on the amount of insulation in the wall and the ambient temperature. Furthermore, the first and last grid points also have to take the floor or the roof into account depending on the model orientation.

The solid phase internal energy required is mainly based on the fluid-solid phase convection and the axial conduction and radiation. The axial conduction and radiation calculation requires the solid-phase temperatures of both the adjacent cells to determine the gradient. Furthermore, the temperature of the fluid-phase is used along with the solid-phase temperatures to determine the effective conduction coefficient.

The pressure loss is calculated based on the thermal properties and the geometrical values for the cell. The pressure of the individual cells is based on the outlet pressure of the TES where each grid point adds the change in the pressure to the grid point pressure. The outlet pressure will be either atmospheric pressure or atmospheric pressure plus the pressure loss of the heat exchanger.

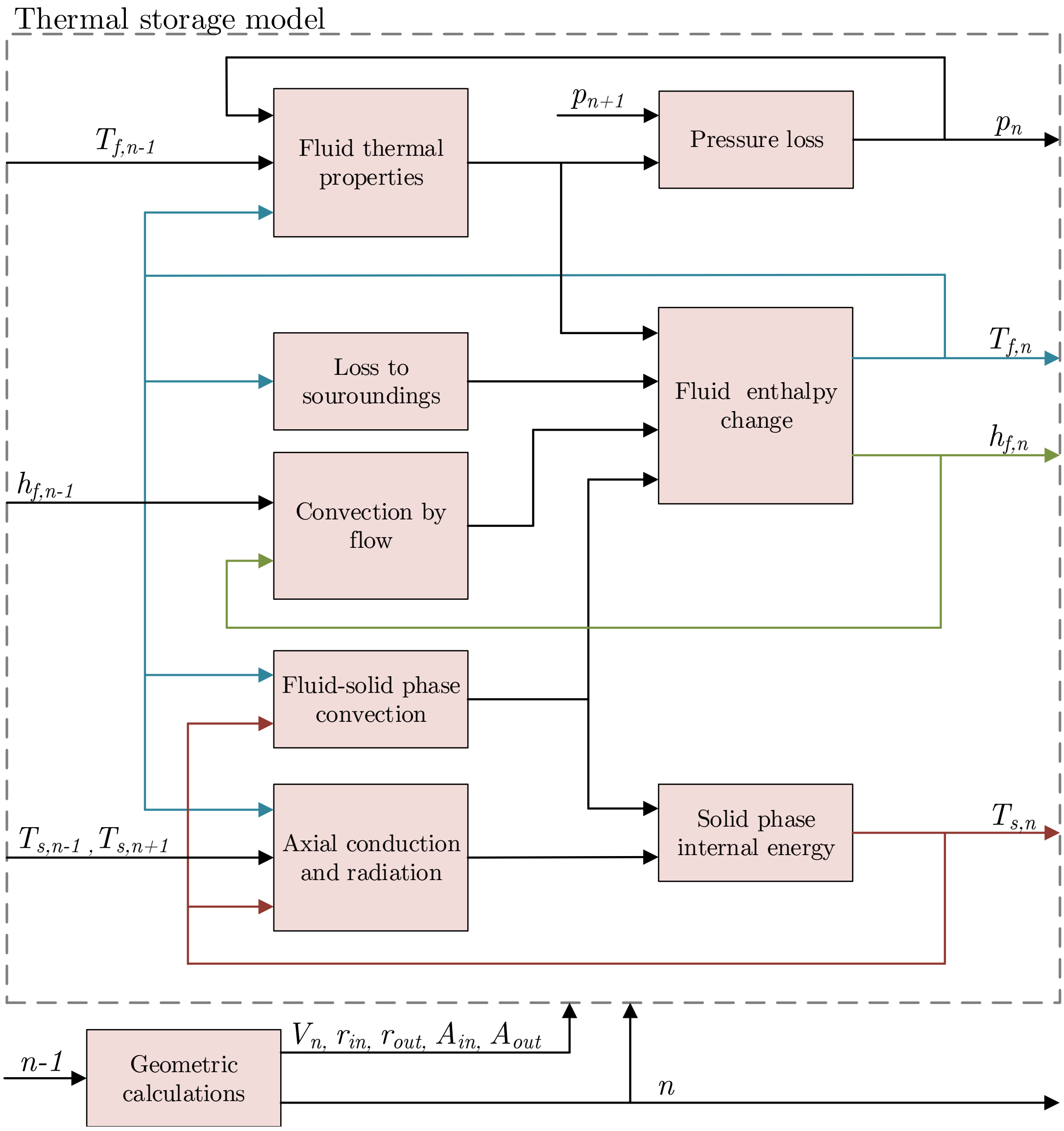

Figure B.1: Detailed block diagram of the over all structure of the individual grid point.

C. Temperature dependent heat capacity

The Simulink model determines the internal energy of the rocks based on the specific heat capacity of the rocks. Initially, the internal energy needs to be determined based on an initial temperature that often consists of a heat front at a specific shape and location in the TES depending on how it has been generated. $u_{s,n,ini}$ is determined by:

$$u_{s,n,ini} = (1-\varepsilon)\, V_{s,n} \rho_s c_{s,n} \left(T_{s,n}\right) \left(T_{max} - T_{min}\right) \tag{C.1}$$

where $c_{s,n}\left(T_{s,n}\right)$ is the rock specific heat capacity at the initial temperature but normalised to a scale between 0 and the maximum value of $c_{s,n}$ at T_{max} in the TES. This causes the initial amount of energy to be zero if $T_{s,n}$ is equal to the minimum TES temperature T_{min}. Likewise, if $T_{s,n} = T_{max}$, then $u_{s,n,ini}$ will be the maximum amount of energy that can be stored at the current grid point as the temperature cannot increase beyond T_{max}. The scaling compared to the original Kelly correlation is shown in figure C.1.

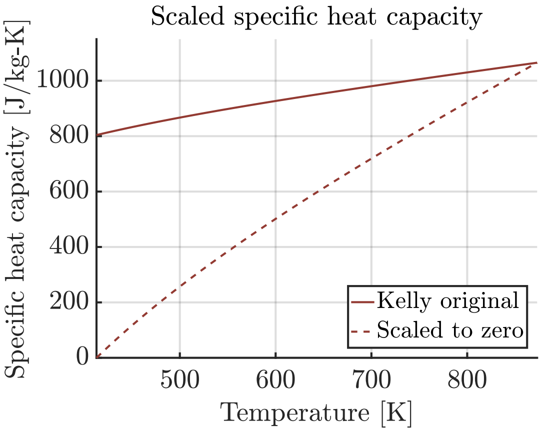

Figure C.1: Scaling of the specific rock heat capacity for the Simulink model.

The internal energy of the rocks is determined in the Simulink model by using $u_{s,ini}$ as the initial condition.

$$u_{s,n} = \int_{t=0}^{t_{final}} \left(\dot{q}_{cond} - \dot{q}_{conv}\right) dt \tag{C.2}$$

The temperature for the grid point is then calculated as $T_{s,n}\left(c_{s,n}\right)$ which is the inverse of $c_{s,n}\left(T_{s,n}\right)$ where $c_{s,n}$ is still normalised to a scale between 0 and the maximum value of $c_{s,n}$. $c_{s,n}$ is determined by:

$$c_{s,n} = \frac{u_s}{\left(1-\varepsilon\right) V_{s,n} \rho_{s,n} \left(T_{max} - T_{min}\right)} \tag{C.3}$$

The implementation of the specific heat capacity of the rocks in Simulink in this manner is assumed to be the main cause of an error in the model. The sum of energies added to the TES, based on the inlet and outlet flows along with the thermal losses, do not match the amount of energy stored in the TES when calculating the energy in the TES based on the final temperature after the simulation is complete. The difference between the stored energy and the energy added or removed from the system is in the order of 1.8% to 4% for the majority of the simulations in this study. This means that up to 4% extra energy is present in the TES when calculation the energy content based on the TES temperature compared to the energy that is added or removed from the TES during simulation.

D. Thermal transport phenomena in the TES

This appendix describes the additional equations and methods used to determine the effective conduction coefficient λ_{eff} and the losses associated with the TES surfaces and the insulation.

D.1 Axial conduction and Radiation

Equation 2.13 in section 2.1.4 describes the effective axial conduction and radiation coefficient. This equation is based on the void-to-void radiative heat transfer coefficient h_{rv} and the solid surface to solid surface radiative heat transfer coefficient h_{rs} along with ϕ, the ratio of the effective thickness of the fluid film adjacent to the surface of two particles to the particle diameter.

The void-to-void radiative heat transfer coefficient h_{rv} is given by:

$$h_{rv} = \frac{0.1952}{1 + \dfrac{\varepsilon}{2\left(1-\varepsilon\right)} \dfrac{1-\epsilon_s}{\epsilon_s}} \left(\frac{T_f}{100}\right)^3 \tag{D.1}$$

h_{rs}, the solid surface to solid surface radiative heat transfer coefficient, is given by (Yagi and Kunii, 1957):

$$h_{rs} = 0.1952 \left(\frac{\epsilon_s}{2-\epsilon_s}\right) \left(\frac{T_s}{100}\right)^3 \tag{D.2}$$

The ratio of the effective thickness of the fluid film adjacent to the surface of two particles to the particle diameter ϕ is defined as:

$$\phi = \phi_2 + \left(\phi_1 - \phi_2\right) \frac{\varepsilon - \varepsilon_2}{\varepsilon_1 - \varepsilon_2} \tag{D.3}$$

where ε_1 and ε_2 represent minimum and maximum possible void fractions respectively with $\varepsilon_1 = 0.26$ for a tightly packed bed and $\varepsilon_2 = 0.476$ for a loosely packed bed. These are illustrated in figure D.1.

It is important to note that the unit of h_{rv} and h_{rs} in the reference is given in kcal/m^2-hr-K which results in a multiplication factor of 1.162 in order to convert to W/m^2-K.

$$\phi_i = \frac{1}{2} \frac{\frac{\kappa - 1}{\kappa} \sin^2\theta_i}{\ln\left(\kappa - (\kappa - 1)\cos\theta_i\right) - \frac{\kappa - 1}{\kappa}\left(1 - \cos\theta_i\right)} \frac{2}{3}\frac{1}{\kappa} \tag{D.4}$$

where $\kappa = \lambda_s/\lambda_f$ and $\sin^2\theta_i = 1/n_i$. Here, n_i is the number of contact points of a semi-spherical surface of a particle. For a loosely packed bed, $n_1 = 1.5$ and for a tightly packed bed, $n_1 = 4\sqrt{3}$.

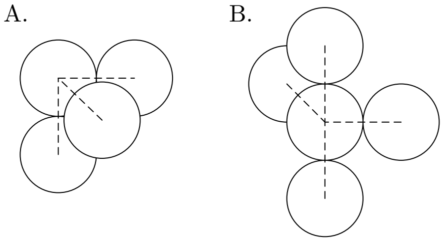

Figure D.1: A. Tightly backed particles with $\varepsilon_1 = 0.26$. B. Loosely packed particles with $\varepsilon_2 = 0.476$. Adapted from (Yagi and Kunii, 1957)

D.2 Thermal losses

The calculations of the thermal losses through the roof, wall and floor described in section 2.1.5 are presented in the following sections.

D.2.1 Thermal losses through walls

The thermal loss through the lateral walls of the storage will be calculated based on inside convection, conduction and radiation to the roof internal surface along with the roof insulation. The overall heat transfer coefficient for the lateral wall is thus expressed as (Cengel et al., 2012):

$$R_{wall} = \frac{1}{h_{int} A_{c,int}} + \sum_{j=0}^{n} \frac{\ln\left(r_{j+1}/r_j\right)}{\lambda_j A_{c,j}} \tag{D.5}$$

The internal heat transfer coefficient consists of the heat transfer coefficient for the internal convection as well as the internal radiation and conduction:

$$h_{int} = h_{conv} + h_{rad-cond} \tag{D.6}$$

where h_{conv} covers the convective heat transfer to the wall inside the TES and is calculated by the following equation (Beek, 1962):

$$Nu = \frac{h_{conv} d_p}{\lambda_f} \tag{D.7}$$

with:

$$Nu = \left(3.22\mathrm{Re}_p^{1/3}\mathrm{Pr}^{1/3} + 0.117\mathrm{Re}_p^{0.8}\mathrm{Pr}^{0.4}\right) \tag{D.8}$$

Here, $\mathrm{Re}_p = Gd_p/\mu$ for a packed bed. $h_{rad-cond}$ accounts for both the conductive heat transfer along with the radiative heat transfer and is similar to the expressions in equations 2.13 to D.3 and is based on (Ofuchi and Kunii, 1965):

$$\frac{1}{h_{rad-cond} d_p/\lambda_f} = \frac{1}{\lambda_w^0/\lambda_f} - \frac{0.5}{\lambda_{eff}/\lambda_f} \tag{D.9}$$

where λ_{eff}/λ_f is similar to equation 2.13 and λ_w^0/λ_f is determined by (Ofuchi and Kunii, 1965):

$$\frac{\lambda_w^0}{\lambda_f} = \varepsilon\left(2 + \frac{h_{rv} d_p}{\lambda_f}\right)\frac{1-\varepsilon}{\frac{1}{\phi} + \frac{h_{rs} d_p}{\lambda_f} + \frac{1}{3}\frac{\lambda_f}{\lambda_s}} \tag{D.10}$$

D.2.2 Roof thermal loss

The losses through the roof of the TES $\dot{q}_{roof}$ are determined by the energy balance described in the following equation:

$$\dot{q}_{roof} = \dot{q}_{cond} = \dot{q}_{conv} \tag{D.11}$$

where $\dot{q}_{cond}$ is the conduction through the roof isolation material and $\dot{q}_{conv}$ the convection of the ambient air. The conduction and convection to the roof is given by the following equations:

$$\dot{q}_{cond} = \frac{T_f - T_{surface}}{R_{roof}} \tag{D.12}$$

$$R_{roof} = \frac{1}{A_{roof}}\sum_{j=1}^{n}\frac{t_j}{\lambda_j} \tag{D.13}$$

$$\dot{q}_{conv} = h_{ext} A_{roof}\left(T_{surface} - T_\infty\right) \tag{D.14}$$

The external heat transfer coefficient h_{ext} is given by (Cengel et al., 2012):

$$h_{ext} = \frac{\mathrm{Nu}\lambda_{amb}}{L_{storage}} \tag{D.15}$$

where Nu is the Nusselt number for a flow over a flat plate defined as (Cengel et al., 2012):

$$\mathrm{Nu}_{Laminar} = 0.664\mathrm{Re}_{amb}^{0.5}\mathrm{Pr}^{1/3} \quad for \;\; \mathrm{Re} < 5 \cdot 10^{5} \tag{D.16}$$

$$\mathrm{Nu}_{Turbulent} = 0.037\mathrm{Re}_{amb}^{0.8}\mathrm{Pr}^{1/3} \quad for \;\; \mathrm{Re} > 5 \cdot 10^{5} \tag{D.17}$$

where $\mathrm{Re}_{amb} = \rho_{amb} L_{storage} v_{wind}/\mu$ for the ambient air at an averaged wind speed.

Equation D.11 contains only one unknown, $T_{surface}$, in the expressions for $\dot{q}_{cond}$ and $\dot{q}_{conv}$. These are solved in Simulink using an algebraic constraint that determines $T_{surface}$ based on the condition $\dot{q}_{cond} - \dot{q}_{conv} = 0$.

D.2.3 Floor thermal loss

The losses through the bottom floor of the TES is modelled in a similar way to the walls with:

$$R_{floor} = \sum_{j=0}^{n} \frac{t_j}{\lambda_j A_{floor}} \tag{D.18}$$

The only difference is that the convection term is not included for the floor loss.

E. Energy and exergy calculations

This appendix covers the various calculations of energy accumulated in the TES, the energy input and recovered energy related to efficiencies and loss fractions discussed in section 2.2.

E.1 Energy

The amount of energy transferred to the TES during a charge period is given by:

$$E_{input} = \sum_{t=0}^{t_{charge}} \dot{m} \left(h^t_{f,out} - h^t_{f,in} \right) \Delta t \tag{E.1}$$

Likewise, the amount of energy recovered from the TES during a discharge period is given by:

$$E_{recovered} = \sum_{t=0}^{t_{discharge}} \dot{m} \left(h^t_{f,in} - h^t_{f,out} \right) \Delta t \tag{E.2}$$

The energy accumulated in the TES during a simulation is calculated by:

$$E_{\text{accumulated}} = \sum_{n=1}^{N} (1 - \varepsilon) \rho_s V_n c_s \left(T_n^{t_{final}} - T_{initial} \right) \tag{E.3}$$

The amount of energy used to power the fan during a charge period is calculated with:

$$E_{fan,charge} = \sum_{t=0}^{t_{charging}} \frac{\Delta p^t \dot{m}^t \Delta t}{\rho_f \eta_{fan}} \tag{E.4}$$

The amount of energy used to power the fan during a discharge period also has to take the Rankine-cycle efficiency into consideration as thermal energy from the TES used to run the Rankine-cycle is used to power the fan during discharge given by:

$$E_{fan,discharge} = \sum_{t=0}^{t_{discharge}} \frac{\Delta p^t \dot{m}^t \Delta t}{\rho_f \eta_{fan} \eta_{Rankine}} \tag{E.5}$$

E.2 Exergy

The exergy input to the system is over the charge period is calculated by:

$$Ex_{input} = \sum_{t=0}^{t_{charging}} \dot{m}\left[\left(h_{h,in} - h_{f,out}\right) - T_0\left(s_{f,in} - s_{f,out}\right)\right]\Delta t \tag{E.6}$$

where T_0 is the reference temperature of the entropy, in this case 298 K, and $s_{f,in}$ and $s_{f,out}$ is the entropy at the roof and floor during charge respectively. The exergy recovered from the TES over the charge period is given by:

$$Ex_{recovered} = \sum_{t=0}^{t_{discharging}} \dot{m}\left[\left(h_{h,out} - h_{f,in}\right) - T_0\left(s_{f,out} - s_{f,in}\right)\right]\Delta t \tag{E.7}$$

The exergy used to run the fan during discharge $Ex_{fan,discharge}$ is calculated by:

$$Ex_{fan,discharge} = f_{fan,discharge}Ex_{recovered} \tag{E.8}$$

where $f_{fan,discharge}$ is the fraction of the total amount of energy recovered during the discharge period used to run the fan. The total exergy accumulated in the TES is calculatrd by:

$$Ex_{accumulated} = \sum_{n=1}^{N}\left[\left(1-\varepsilon\right)V_n\rho_s c_{s,n}\left(T_n^{t_{final}} - T_0\right) - T_0\cdot\ln\left(\frac{T_n^{t_{final}}}{T_0}\right)\right] \tag{E.9}$$

F. Heat exchanger design parameters

The finned tube used for the design of the heat exchanger in this study is shown in figure 3.10 in section 3.2.

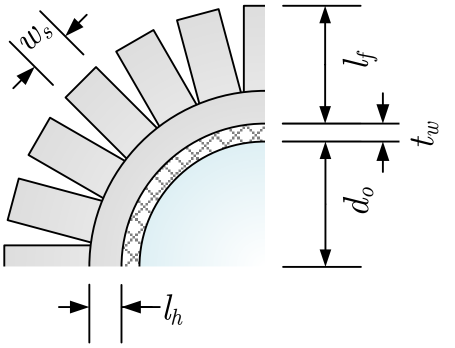

Figure F.1: Cross-section of the finned tube (Adapted from ESCOA (1979)).

The geometrical parameters of the finned tube can be seen in figureF.1.

The values of the tube parameters can be seen in table F.1 and have been measured on the sample shown in figure 3.10 or calculated based on the measured values.

Finned Tube parameters		
Parameter	Variable	Value
Tube outer diameter	d_o	0.038 m
Tube wall thickness	t_w	0.004 m
Fin height	l_f	0.016 m
Fin base height	l_h	0.005 m
Fin width	w_s	0.005 m
fin Thickness	t_f	0.001 m
Spacing between fins	s_f	0.005 m
Longitudinal pitch	P_l	0.080 m

Table F.1: Geometrical values of the finned tubes measured as shown in figure F.1.

F.1 Heat exchanger design equations

This section covers the additional equations used to calculate the heat transfer coefficient and the pressure loss for the heat exchanger. The Reynolds number used in the calculations for the heat exchanger is defined as:

$$\mathrm{Re}_{he} = \frac{Gd_o}{\mu_{air}} \tag{F.1}$$

where G is the mass flux given by: $G = \dot{m}/A_n$

F.1.1 Heat transfer coefficient calculations

The heat transfer coefficients are determined mainly by the flow properties and the area of the finned tube available for heat transfer. The effective heat transfer coefficient on the air side can be determined by:

$$h_e = h_o \frac{EA_{fo} + A_{po}}{A_o} \tag{F.2}$$

where A_{fo} is the fin surface area per unit length of the finned tube. A_{po} is the prime surface area of the finned tube. A_o is the total surface area of the finned tube. E is the fin efficiency defined as $E = 0.61$. h_o is the average air side heat transfer coefficient and is given by:

$$h_o = \frac{1}{\dfrac{1}{h_c + h_r} + R_{fo}} \tag{F.3}$$

where h_r is the average air side radiation heat transfer coefficient and R_{fo} is the thermal resistance caused by fouling. Fouling, although, is omitted in the model as the secondary heat transfer medium is assumed to be clean air. h_c is the average air side convection heat transfer coefficient that can be determined by:

$$h_c = jGc_p \left(\frac{\lambda_p}{c_{p,air}\mu_{air}} \right)^{0.67} \tag{F.4}$$

where j is the Colburn j-factor given by the following equation:

$$j = C_1 \cdot C_3 \cdot C_5 \left(\frac{d_f}{d_o} \right)^{0.5} \left(\frac{T_{f,he,avg}}{T_{fin,avg}} \right)^{0.25} \tag{F.5}$$

where C_1, C_3 and C_5 are dimensionless corrections to the j-factor in respect to the Reynolds number, the fin geometry, and the tube row layout respectively given by equations F.10 ,F.11 and F.12. d_f and d_o is the outer tube fin diameter and the outer tube diameter respectively while $T_{fin,avg}$ and $T_{f,he,avg}$ is the average fin temperature and the average outside temperature respectively. The average outside temperature is based on the air inlet and outlet temperature of the heat exchanger given by:

$$T_{f,he,avg} = \frac{T_{f,he,in} + T_{f,he,out}}{2} \tag{F.6}$$

Likewise the internal tube flow average temperature $T_{w/s,avg}$ is given by:

$$T_{w/s,avg} = \frac{T_{w/s,in} + T_{w/s,out}}{2} \tag{F.7}$$

The average fin temperature $T_{fin,avg}$ and average tube wall temperature $T_{w,avg}$ are given in the following equations:

$$T_{fin,avg} = T_{w/s,avg} + 0.3\left(T_{f,he,avg} - T_{w/s,avg}\right) \tag{F.8}$$

$$T_{wall,avg} = T_{w/s,avg} + 0.1\left(T_{f,he,avg} - T_{w/s,avg}\right) \tag{F.9}$$

The Reynolds number correction to the j-factor is given by:

$$C_1 = 0.25\mathrm{Re}^{-0.25} \tag{F.10}$$

The geometry correction to the j-factor is given by:

$$C_3 = 0.35 + 0.5e^{-0.35\,(l_f/s_f)} \tag{F.11}$$

The non-equilateral and row correction to the j-factor is given by:

$$C_5 = 1.1 - \left(0.75 - 1.5 * e^{-0.70 * N_r}\right) e^{-2\,(P_l/P_t)} \tag{F.12}$$

F.1.2 Heat exchanger pressure loss calculations

The pressure loss of the air stream is based on the number of tube rows in the flow direction and the mass flow rate per unit area in the narrowest cross section through the heat exchanger. The pressure loss can be determined by:

$$\Delta p = (f_f + a)\,\frac{G^2 * N_r}{0.5\rho_{avg}} \tag{F.13}$$

where f is the Fanning friction factor [-] and a is the pressure drop acceleration loss term [-]. N_r is the number of tube rows in the direction of flow and ρ_{avg} is the average air density in the air stream.

The Fanning friction factor used to calculate the pressure loss is given by:

$$f_f = C_2 \cdot C_4 \cdot C_6 \left(\frac{d_f}{d_o} \right) \tag{F.14}$$

The pressure drop acceleration loss term is given by

$$a = \frac{1+\beta^2}{4N_r} \rho_{avg} \left(\frac{1}{\rho_{out}} - \frac{1}{\rho_{in}} \right) \tag{F.15}$$

The contraction factor is given by:

$$\beta^2 = (A_n/A_d)^2 \tag{F.16}$$

The Reynolds number correction to the f-factor is given by:

$$C_2 = 0.07 + 8.0\mathrm{Re}^{-0.45} \tag{F.17}$$

The geometry correction to the f-factor is given by:

$$C_4 = 0.08\,(0.15P_t/d_o)^{-1.1}\,(l_f/s_f)^{0.20} \tag{F.18}$$

The non-equilateral and row correction to f-factor is given by:

$$C_6 = 1.6 - \left(0.75 - 1.5 * e^{-0.7 * N_r} \right) e^{-0.2\,(P_l/P_t)} \tag{F.19}$$

G. Additional SRC model results

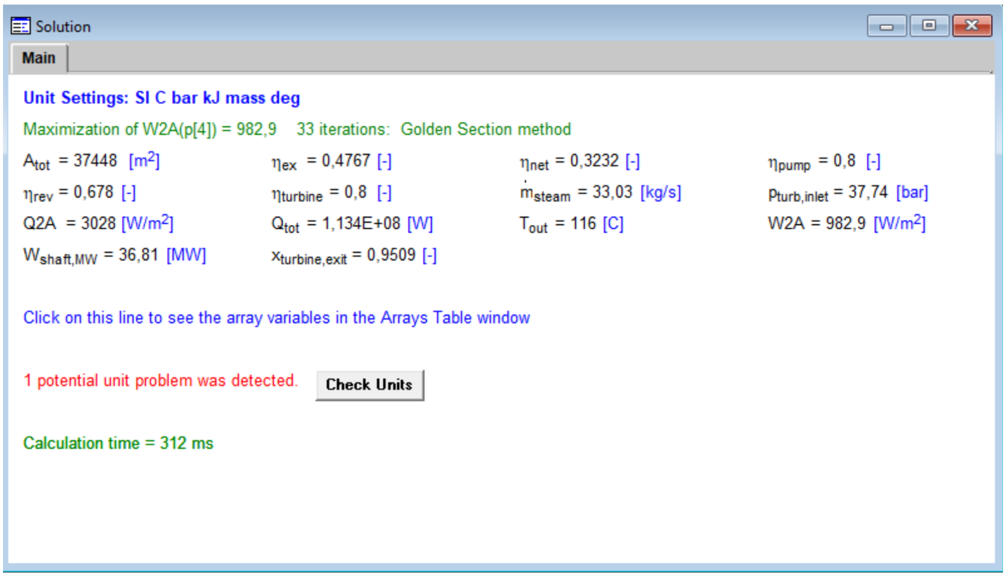

Unit Settings: SI C bar kJ mass deg

Maximization of W2A(p[4]) = 982,9   33 iterations: Golden Section method

A_{tot} = 37448 [m^2] η_{ex} = 0,4767 [-] η_{net} = 0,3232 [-] η_{pump} = 0,8 [-]

η_{rev} = 0,678 [-] $\eta_{turbine}$ = 0,8 [-] $\dot{m}_{steam}$ = 33,03 [kg/s] $P_{turb,inlet}$ = 37,74 [bar]

Q2A = 3028 [W/m^2] Q_{tot} = 1,134E+08 [W] T_{out} = 116 [C]   W2A = 982,9 [W/m^2]

$W_{shaft,MW}$ = 36,81 [MW] $x_{turbine,exit}$ = 0,9509 [-]

Click on this line to see the array variables in the Arrays Table window

1 potential unit problem was detected.

Calculation time = 312 ms

Figure G.1: Additional model results for the SP SRC optimised for W_{shaft}/A_{tot} and 100 MW discharge rate.

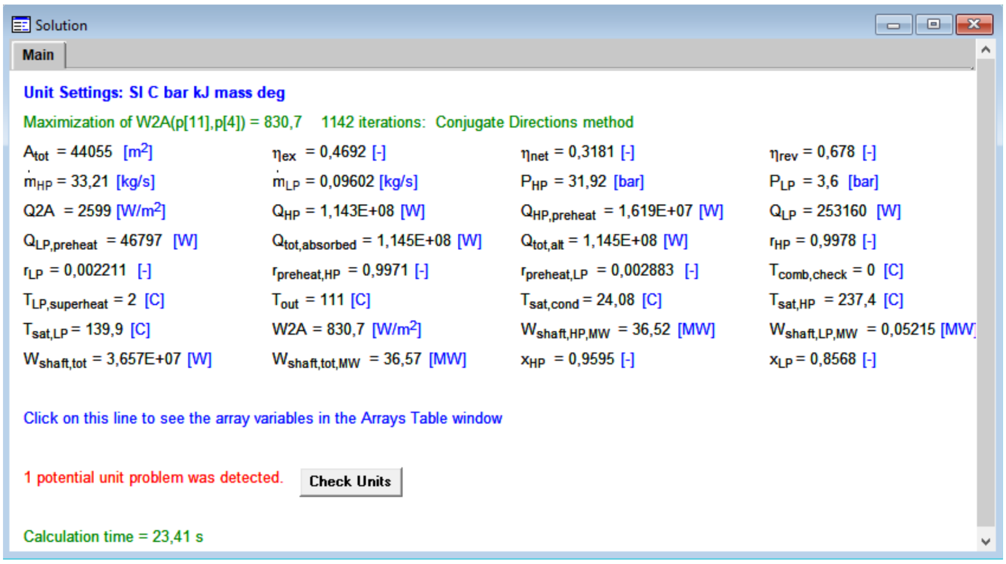

Unit Settings: SI C bar kJ mass deg

Maximization of W2A(p[11],p[4]) = 830,7   1142 iterations: Conjugate Directions method

A_{tot} = 44055 [m^2] η_{ex} = 0,4692 [-] η_{net} = 0,3181 [-] η_{rev} = 0,678 [-]

$\dot{m}_{HP}$ = 33,21 [kg/s] $\dot{m}_{LP}$ = 0,09602 [kg/s] P_{HP} = 31,92 [bar] P_{LP} = 3,6 [bar]

Q2A = 2599 [W/m^2] Q_{HP} = 1,143E+08 [W] $Q_{HP,preheat}$ = 1,619E+07 [W] Q_{LP} = 253160 [W]

$Q_{LP,preheat}$ = 46797 [W] $Q_{tot,absorbed}$ = 1,145E+08 [W] $Q_{tot,alt}$ = 1,145E+08 [W] r_{HP} = 0,9978 [-]

r_{LP} = 0,002211 [-] $r_{preheat,HP}$ = 0,9971 [-] $r_{preheat,LP}$ = 0,002883 [-] $T_{comb,check}$ = 0 [C]

$T_{LP,superheat}$ = 2 [C] T_{out} = 111 [C] $T_{sat,cond}$ = 24,08 [C] $T_{sat,HP}$ = 237,4 [C]

$T_{sat,LP}$ = 139,9 [C]   W2A = 830,7 [W/m^2] $W_{shaft,HP,MW}$ = 36,52 [MW] $W_{shaft,LP,MW}$ = 0,05215 [MW]

$W_{shaft,tot}$ = 3,657E+07 [W] $W_{shaft,tot,MW}$ = 36,57 [MW] x_{HP} = 0,9595 [-] x_{LP} = 0,8568 [-]

Click on this line to see the array variables in the Arrays Table window

1 potential unit problem was detected.

Calculation time = 23,41 s

Figure G.2: Additional model results for the DP SRC optimised for W_{shaft}/A_{tot} and 100 MW discharge rate.

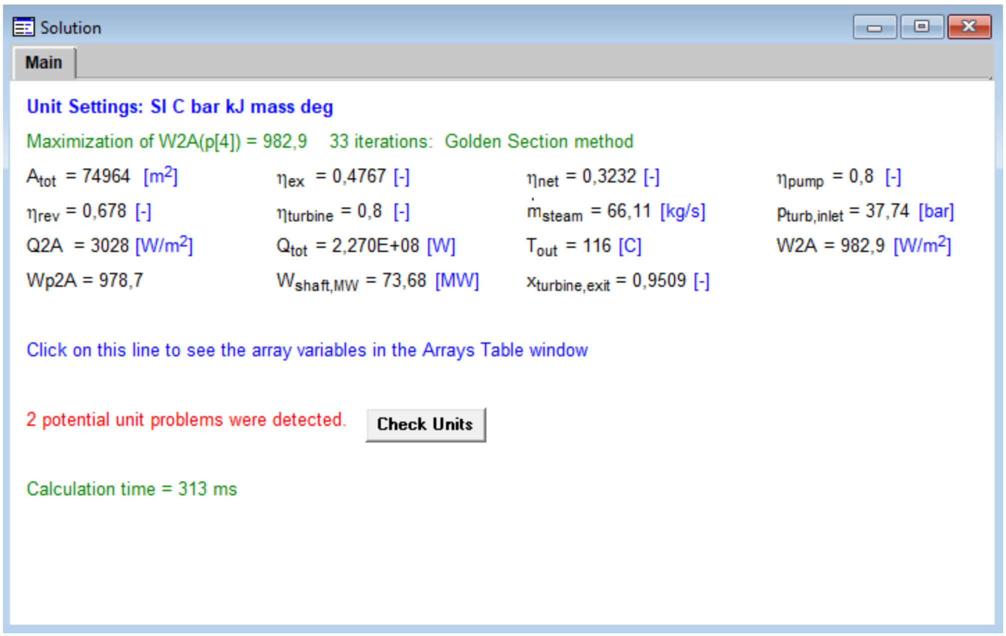

Unit Settings: SI C bar kJ mass deg

Maximization of W2A(p[4]) = 982,9   33 iterations: Golden Section method

A_{tot} = 74964 [m^2] η_{ex} = 0,4767 [-] η_{net} = 0,3232 [-] η_{pump} = 0,8 [-]

η_{rev} = 0,678 [-] $\eta_{turbine}$ = 0,8 [-] $\dot{m}_{steam}$ = 66,11 [kg/s] $p_{turb,inlet}$ = 37,74 [bar]

Q2A = 3028 [W/m^2] Q_{tot} = 2,270E+08 [W] T_{out} = 116 [C]   W2A = 982,9 [W/m^2]

Wp2A = 978,7 $W_{shaft,MW}$ = 73,68 [MW] $x_{turbine,exit}$ = 0,9509 [-]

Click on this line to see the array variables in the Arrays Table window

2 potential unit problems were detected.

Calculation time = 313 ms

Figure G.3: Additional model results for the SP SRC optimised for W_{shaft}/A_{tot} and 100 MW discharge rate.

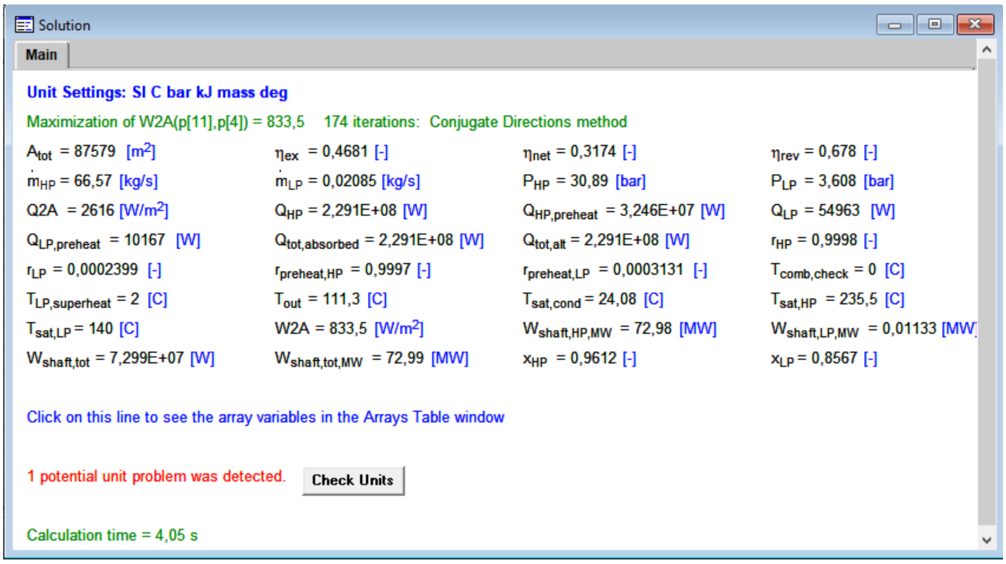

Unit Settings: SI C bar kJ mass deg

Maximization of W2A(p[11],p[4]) = 833,5   174 iterations: Conjugate Directions method

A_{tot} = 87579 [m^2] η_{ex} = 0,4681 [-] η_{net} = 0,3174 [-] η_{rev} = 0,678 [-]

$\dot{m}_{HP}$ = 66,57 [kg/s] $\dot{m}_{LP}$ = 0,02085 [kg/s] P_{HP} = 30,89 [bar] P_{LP} = 3,608 [bar]

Q2A = 2616 [W/m^2] Q_{HP} = 2,291E+08 [W] $Q_{HP,preheat}$ = 3,246E+07 [W] Q_{LP} = 54963 [W]

$Q_{LP,preheat}$ = 10167 [W] $Q_{tot,absorbed}$ = 2,291E+08 [W] $Q_{tot,alt}$ = 2,291E+08 [W] r_{HP} = 0,9998 [-]

r_{LP} = 0,0002399 [-] $r_{preheat,HP}$ = 0,9997 [-] $r_{preheat,LP}$ = 0,0003131 [-] $T_{comb,check}$ = 0 [C]

$T_{LP,superheat}$ = 2 [C] T_{out} = 111,3 [C] $T_{sat,cond}$ = 24,08 [C] $T_{sat,HP}$ = 235,5 [C]

$T_{sat,LP}$ = 140 [C]   W2A = 833,5 [W/m^2] $W_{shaft,HP,MW}$ = 72,98 [MW] $W_{shaft,LP,MW}$ = 0,01133 [MW]

$W_{shaft,tot}$ = 7,299E+07 [W] $W_{shaft,tot,MW}$ = 72,99 [MW] x_{HP} = 0,9612 [-] x_{LP} = 0,8567 [-]

Click on this line to see the array variables in the Arrays Table window

1 potential unit problem was detected.

Calculation time = 4,05 s

Figure G.4: Additional model results for the DP SRC optimised for W_{shaft}/A_{tot} and 200 MW discharge rate.

H. Cyclic TES behaviour

In this appendix, the sloping of the heat front in the TES is examined over continuous charge/discharge cycles. The model has been run in a continuous charge/discharge cycle from an initial state of completely discharged at a TES temperature of 413 K. This is followed by 60 charge/discharge cycles consisting of a 77.4 hour period at 230 MW_{th} charge followed by a 154.8 hour discharge period at 115 MW_{th}. The result can be seen in figure H.1. This shows how the heat fronts develops over time. As it can be seen, the heat front begins to stabilise after 30 cycles and only negligible change can be observed from 40 cycles and beyond. Due to this, cycles above cycle 40 are not shown.

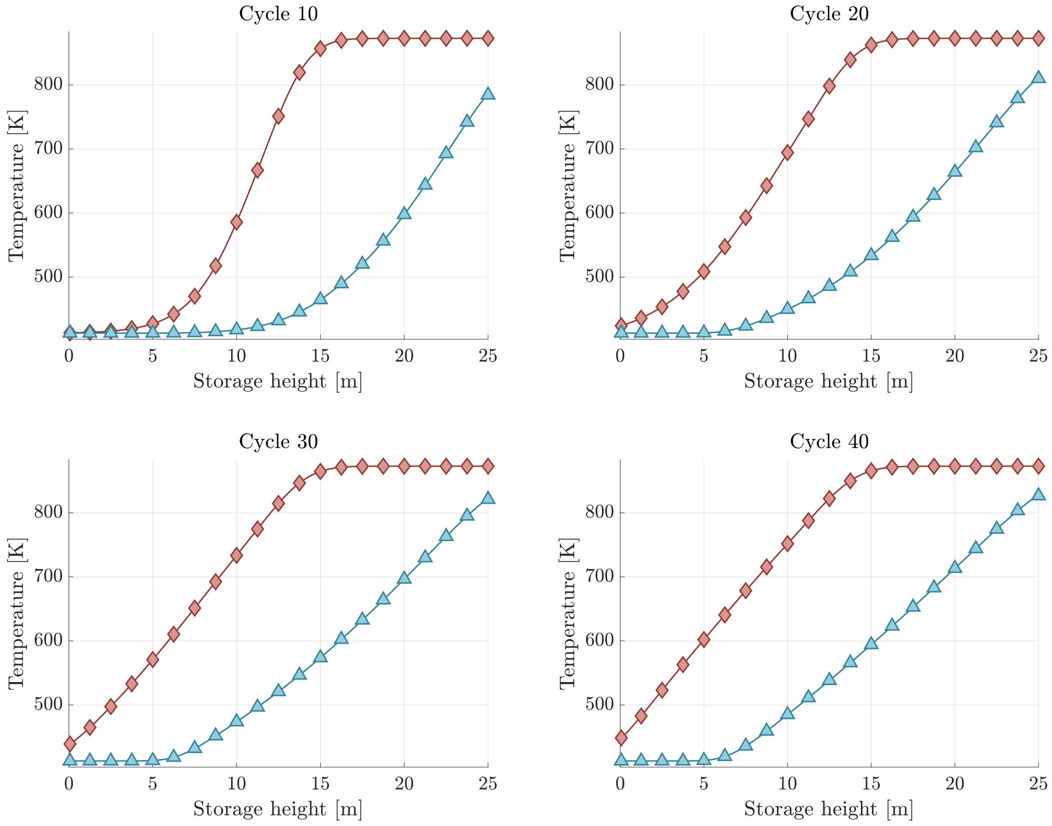

Figure H.1: Energy distribution at maximum allowable charge and discharge.

This illustrates that, if charged and discharged continuously at equivalent rates, the TES behaviour will stop changing between cycles. The capacity of the TES after 40 cycles, following the same method as described above, where the capacity is determined by the difference between charge and discharge, is 17.3 GWh$_{th}$ which is the same as found for the case in section 5.2.1. The charge and discharge times at cycle 40 are described in the following section.

H.1 Charging and discharging times

At the 230 MW charge rate it will take 77.4 hours or 3.2 days to charge the TES to the capacity described above. The temperature at the floor outlet during charge is shown during this time in figure H.2. From this, it can be seen that, after 40 hours of charge at 230 MW$_{th}$, the temperature begins to increase. After after 60 hours the temperature surpasses 415 K. From there, it increases rapidly to 479 K after 77.4 hours.

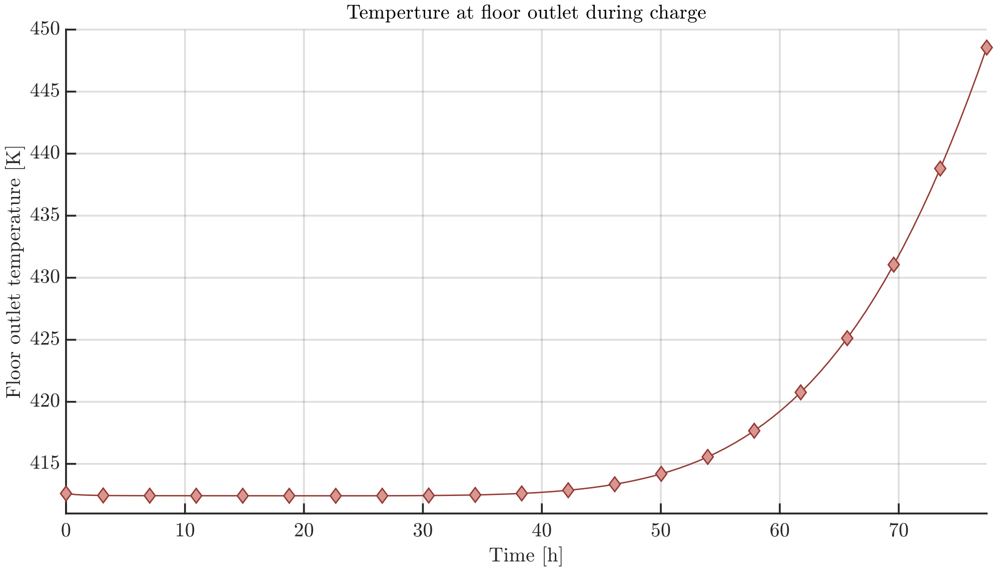

Figure H.2: Temperature at the floor outlet during charge of the TES.

Likewise, for the 115 MW discharge period, the temperature at the roof outlet is shown. The discharge period takes 6.4 days to complete or 154.8 hours. As it can be seen, the temperature begins to drop after only 80 hours and drops below the before mentioned 10 K difference after approximately 120 hours. After 120 hours, the temperature drops rapidly as the TES is depleted.

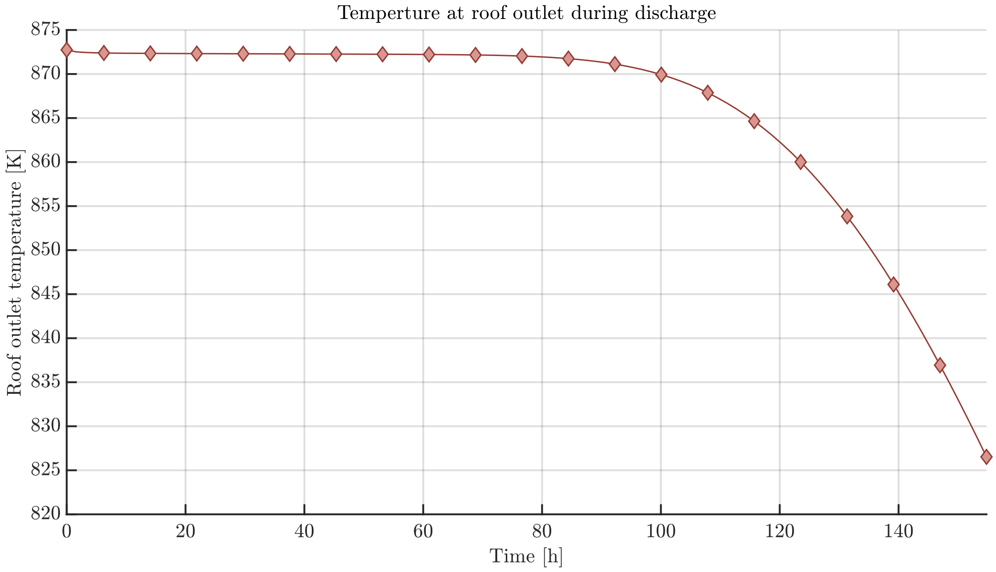

Figure H.3: Temperature at the roof outlet during discharge of the TES.

The increase in floor outlet temperature during charge and the decrease in roof outlet temperature during discharge, makes it necessary to stop the charge and discharge earlier. This means that the capacity of the TES will be reduced if the TES is continuously charged/discharged over long periods. This is, however, not a realistic operation of this type of TES as the storage will be charged when excess electricity is available and discharged when electricity is in demand.